THEORETICAL STUDIES OF NONVALENCE CORRELATION-BOUND ANION STATES

by

Vamsee K. Voora

Bachelor of Science (Hons.), Sri Satya Sai University, 2007

Master of Science, University of Hyderabad, 2009

Submitted to the Graduate Faculty of

the Kenneth P. Deitrich School of Arts and Sciences in partial

fulfillment

of the requirements for the degree of

Doctor of Philosophy

University of Pittsburgh

2014

UNIVERSITY OF PITTSBURGH

DIETRICH SCHOOL OF ARTS AND SCIENCES

This dissertation was presented

by

Vamsee K. Voora

It was defended on

June 20th 2014

and approved by

Kenneth D. Jordan, Department of Chemistry

David Waldeck, Department of Chemistry

Sean Garrett-Roe, Department of Chemistry

John Keith, Department of Chemical Engineering

Dissertation Director: Kenneth D. Jordan, Department of Chemistry

THEORETICAL STUDIES OF NONVALENCE CORRELATION-BOUND ANION STATES

Vamsee K. Voora, PhD

University of Pittsburgh, 2014

Nonvalence correlation-bound anion states have been investigated using state-of-the-art ab initio methodologies as well as by model potential approaches. In nonvalence correlation-bound anion states the excess electron occupies a very extended orbital with the binding to the molecule or cluster being dominated by long-range correlation effects. Failure of conventional Hartree-Fock reference based approaches for treating these anionic states is discussed. Ab initio approaches that go beyond Hartree-Fock orbitals, such as Green's functions, and equation-of-motion methods are used to characterize nonvalence correlation-bound anion states of a variety of systems. The existence of nonvalence correlation-bounds is established for C_{60} and C_6F_6. Edge-bound nonvalence correlation-bound anionic states are also established for polycyclic aromatics. Accurate one-electron model potential approaches, parametrized using the results of ab initio calculations, are developed. The model potentials are used to study nonvalence correlation-bound anion states of large water clusters as well as "superatomic" states of fullerene systems.

TABLE OF CONTENTS

LIST OF TABLES

LIST OF FIGURES

ix

PREFACE

I would like to thank Prof. Ken Jordan for his excellent guidance and patience with me. I hope to continue with my affinity for excess electrons that I inherited from him. I would also like to thank Prof. Thomas Sommerfeld, another excess electron aficionado, for fruitful discussions during his summer visits to Pitt. I thank the current and former Jordan group members for their help and encouragement, and wish them great success in their future. Finally I thank my parents and brother for their tireless support.

1.0   INTRODUCTION

Anions can lie energetically below or above the ground state of the neutral atom, molecule, or cluster of interest. Anions that lie energetically below the ground state of the neutral species are stable with respect to electron detachment, while those that lie energetically above the ground state are temporary as they are unstable with respect to electron detachment.

The excess electron binding energy (EBE) to a molecule has several contributions as shown in equation 1.1:

$$EBE = E(ke) + E(es) + E(exch) + E(corr) \tag{1.1}$$

The first term, $E(ke)$, is the kinetic energy of the electron binding and is necessarily repulsive due to the localization of the excess electron. $E(es)$ accounts for the electrostatic interactions and is especially important for electrostatic-bound anions such as dipole-bound anions. Exchange interactions between the excess electron and the electrons of the molecule are accounted for by the $E(exch)$. The first three terms, together, are computed from Koopmans' theorem (KT).[1] These three terms alone may not be sufficient to bind an excess electron, but when correlation effects, i.e. $E(corr)$ (the fourth term in equation 1.1) are included at an appropriate level (including relaxation in response to correlation, E(relax-corr)) the excess electron may then become bound.

Electron binding can be computed using Hartree-Fock (HF) orbital based methods such as second-order Möller-Plesset (MP2),[2] coupled-cluster singles-doubles (CCSD) and CCSD with perturbative triples (CCSD(T))[3] if the anion is bound in the Koopmans' theory approximation. MP2 does not account for the relaxation in response to correlation term at all, whereas, CCSD, and CCSD(T) may or may not recover the this effect depending upon the nature of the initial orbitals. An example where MP2, CCSD and CCSD(T) would fail are the correlation-bound anions for which the Hartree-Fock reference orbitals are a poor

starting guess for the excess electron. On the other hand, the algebraic-diagrammatic construction (ADC),[4] electron attachment equation-of-motion coupled cluster (EA-EOM-CC),[5] orbital optimized MP2 (OMP2),[6,7] and Brueckner coupled-cluster doubles with perturbative triples (BCCD(T))[8] methods account for E(relax-corr). For the methods listed above, except for EOM-MP2, EOM-CCSD and ADC(2), the energies of the neutral and anionic systems were calculated, and EBE was obtained from $E_{neutral}$-E_{anion}. Below I give a brief description of the ADC, EA-EOM and OMP2 methods. A diagrammatic approach will be used to illustrate various contributions to the electron binding by different methods.

1.1   ALGEBRAIC DIAGRAMMATIC CONSTRUCTION

Electron affinities can be obtained from the poles of a one-particle propagator. ADC methods are based on diagrammatic perturbation of the propagator (or the Greens function) for one-particle. The simplest approximation of the ADC is the second-order approximation, ADC(2).[4] The following diagrams contribute to the ADC(2).
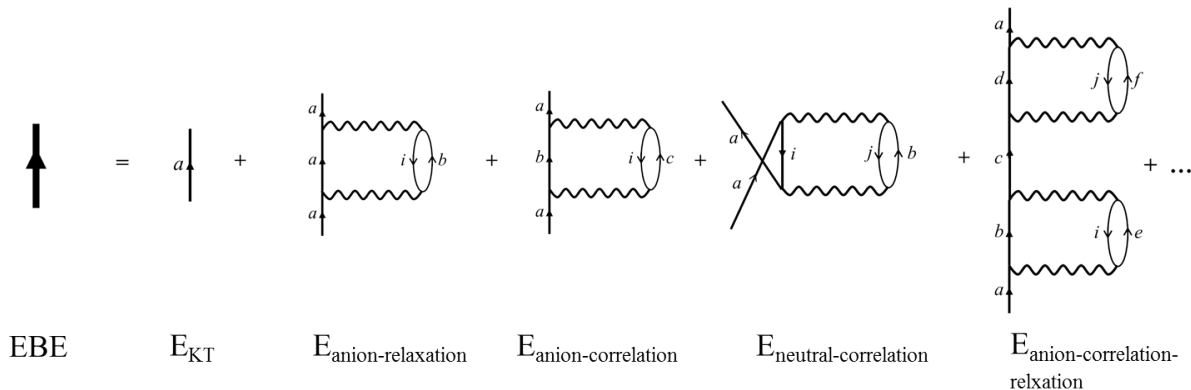
Figure 1.1: Diagrams that contribute to the EBE computed using ADC(2)

In the diagrams above, the lines directing upwards represent particle levels, while the lines pointing downwards represent holes. The indices a, b, c, etc. are used to denote the particle lines while i, j, k, etc are used to denote the hole lines. The wiggly lines represent the antisymmetrized coulomb interactions between electrons. The first diagram on the right hand side represents the Hartree-Fock orbital Coulomb and exchange interaction between

the excess electron in orbital and all the other electrons of the molecule. The second diagram represents the electronic relaxation of the molecule due to addition of the excess electron. The third diagram represents the correlation gained upon addition of an excess electron, while the fourth diagrams shows the correlation lost in the neutral due to the addition of an electron to orbital a. The final diagram represents the relaxation of the excess electron in response to correlation effects. The final diagram and the other higher order diagrams that are not shown, are the cross terms arising from first four diagrams. ADC(2) is missing all odd order correlation and relaxation effects. Many of the missing diagrams are accounted for by the ADC(3) and EOM methods.

1.2 EQUATION-OF-MOTION COUPLED-CLUSTER THEORY

Another approach to directly computing the electron affinity of a molecule is the electron affinity equation of motion (EA-EOM) approach. This approach is generally used with a coupled cluster singles doubles wavefunction. The (EA-EOM-CCSD) method involves three steps. The first step involves computation of the reference (in this study it is the neutral systems) coupled cluster wavefunction

$$\Psi = e^{\hat{T}} \left| \Phi_0 \right\rangle \tag{1.2}$$

where, $\left| \Phi_0 \right\rangle$ is the reference Hartree-Fock Slater determinant and $\hat{T}$ is the coupled cluster excitation operator containing the amplitudes. The second step involves the computation of the similarity transformation of the Hamiltonian using the coupled cluster amplitudes to give

$$\bar{H} = e^{-\hat{T}} \hat{H} e^{\hat{T}}. \tag{1.3}$$

The final step involves the computation of eigenvalues of the $\bar{H} - E_{CCSD}$,

$$(\bar{H} - E_{CCSD})C = C\Delta E \tag{1.4}$$

in the basis of $1p$ and $2p1h$ configurations:

$$\left| C \right\rangle = \left(\sum_a C^a \hat{a}^+ + \sum_{abi} C_i^{ab} \hat{a}^+ \hat{b}^+ \hat{i} \right) \left| \Phi_0 \right\rangle \tag{1.5}$$

3

$\hat{a}^+$ indicates a creation operator while $\hat{i}$ indicates a destruction operator. The eigenvalues, ΔE, correspond to the electron affinities. For more details, the reader is referred to ref 5. The equations for EA-EOM-MP2 are similar to those of EOM-CCSD except that the $\hat{T}$ amplitudes are obtained from MP2.[9,10] Both EA-EOM-MP2 and EOM-CCSD contain many diagrams, representing higher order correlation and relaxation effects, missing in ADC(2) including the following:
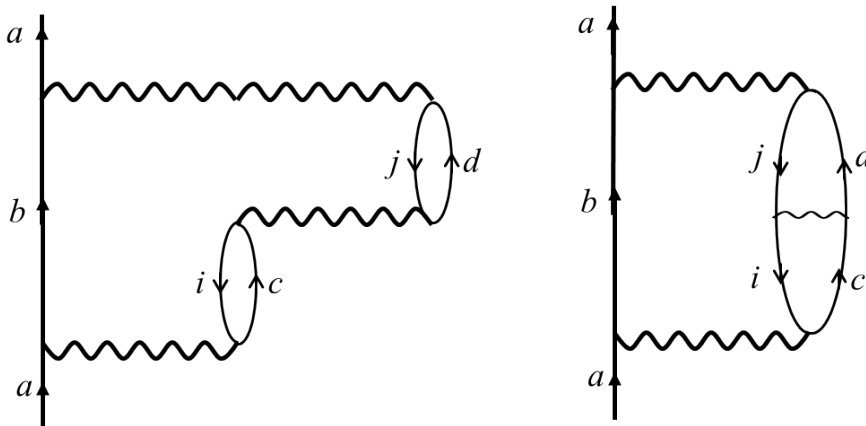
Figure 1.2: Some third-order diagrams that contribute to the EBE computed using EOM-CCSD, EOM-MP2 and ADC(3)

1.3 ORBITAL OPTIMIZED MP2

The MP2 energy is the sum of HF energy and the second-order correlation energy. The orbitals in HF or MP2 are not optimized with respect to correlation affects. In orbital optimized MP2 (OMP2), the orbitals are determined through minimization of the net MP2 energy thereby incorporating orbital relaxation with response to correlation.

In this work, we focus on nonvalence correlation-bound anions, which, although stable at an appropriate correlated level of theory, are unbound in the HF approximation. Such species cannot, in general, be adequately described using electronic structure methods that assume the validity of the Hartree-Fock wavefunction as the reference configuration for the

anion. Examples of such systems are the nonvalence correlation-bound anions of NaCl clusters,[11] Xe clusters,[12] C_{60},[13] C_6F_6[14] and the anions of certain water clusters.[15] Two methods used in the past to characterize such anions are the second-order algebraic diagrammatic construction (ADC(2)) Green's function[4] and the equation-of-motion (EOM) methods.[5,9,10] However, to date we lack a comprehensive understanding of the type of interactions that must be included in a theoretical method to accurately characterize nonvalence correlation-bound anions. In this work, we examine in detail the applicability of various theoretical methods to nonvalence correlation-bound anions, and in the process gain insights about the nature of the correlation effects that are important in their description.

Chapter 2 further discusses the nature of nonvalence correlation-bound anions and theoretical methodologies necessary to describe correlation bound anions. Two model systems, a $(H_2O)_4$ cluster and a CO_2 molecule are used to illustrate the nuances of nonvalence correlation-bound anions and to test the applicability of various theoretical methods. A nonvalence correlation-bound anion state of TCNE is also established.

In chapter 3, state-of-the-art ADC(2), EOM-EA-CCSD, and EOM-EA-CCSD(2) many-body methods are used to calculate the energies for binding an excess electron to selected water clusters up to $(H_2O)_{24}$ in size. The systems chosen for study include several clusters for which the Hartree-Fock method either fails to bind the excess electron or binds it only very weakly. The three approaches are found to give similar values of the electron binding energies. The reported electron binding energies are the most accurate to date for such systems and these results will be used as benchmarks for testing model potential approaches for describing the interactions of excess electrons with water clusters and bulk water.

A new polarization model potential for describing the interaction of an excess electron with water clusters is presented in chapter 4. This model, which allows for self-consistent electron-water and water-water polarization, including dispersion interactions between the excess electron and the water monomers, gives electron binding energies in excellent agreement with high-level ab initio calculations for both surface-bound and cavity-bound states of $(H_2O)_n^-$ clusters. By contrast, model potentials that do not allow for a self-consistent treatment of electron-water and water-water polarization are less successful at predicting the relative stability of surface-bound and cavity-bound excess electron states.

In chapter 5, it is established using high-level electronic structure calculations that C_{60}

has an s-type correlation-bound anion state with an electron binding energy of about 118 meV. Examination of the "singly occupied" natural orbital of the anion reveals that about 9% of the charge density of the excess electron is localized inside and about 91% is localized outside the C_{60} cage. Calculations were also carried out for the He@C_{60}, Ne@C_{60}, and H_2O@C_{60} endohedral complexes. For each of these species the s-type anion is predicted to be less weakly bound than for C_{60} itself.

A one-electron model Hamiltonian for characterizing nonvalence correlation-bound anion states of fullerene molecules is presented in chapter 6. These states are the finite system analogs of image potential states of metallic surfaces. The model potential accounts for both atomic and charge-flow polarization and is used to characterize the correlation-bound anion states of the C_{60}, $(C_{60})_2$, C_{240} and C_{60}@C_{240} fullerene systems. Although C_{60} is found to have a single (s-type) nonvalence correlation-bound anion state, the larger fullerenes are demonstrated to have multiple correlation-bound anion states.

Chapter 7 investigates the ground state anion of perfluorobenzene using equation-of-motion (EOM) methods. It is found that at the geometry of the neutral the excess electron is bound by 0.135 eV. This anion state is nonvalence in nature with the excess electron bound in a very diffuse orbital with dispersion type interactions between the excess electron and the valence electrons being pivotal to the binding. The diffuse correlation-bound state is shown to evolve into a more stable compact valence-bound anion state with C_{2v} geometry with a buckled geometry having an adiabatic electron affinity of 0.5 eV. Results are also presented for the bound anion states of the C_6F_6 dimer.

In chapter 8 the nonvalence correlation-bound anion states of several large polycyclic aromatic systems are characterized. In these systems, much of the charge distribution of the excess electron is localized around the periphery of the molecule as a consequence of the electrostatic interaction with polar CH groups. Replacing the H atoms by F atoms or the CH groups by N atoms, shifts the charge density of the excess electron from the periphery to above and below the plane of the acene.

2.0 THEORETICAL APPROACHES FOR TREATING CORRELATION-BOUND ANIONS

2.1 INTRODUCTION

The binding of an excess electron in a nonvalence orbital has electrostatic, correlation, exchange-repulsion and kinetic energy(confinement) contributions, where the exchange-repulsion term includes the effect of orthogonalization to the valence orbitals. The most widely studied nonvalence anions are the dipole-bound species, in which the dipole moment is sufficiently large that the excess electron is bound in the Hartree-Fock approximation. Less understood are the nonvalence correlation-bound anions for which electrostatic interactions alone are not large enough to bind the excess electron. In this work we consider two model systems, a $(H_2O)_4$ cluster as a function of inter-dimer distance R with D_{2h} symmetry and thus no net dipole and the CO_2 molecule as a function of OCO angle to illustrate the nuances of nonvalence correlation-bound anions and to test various electronic structure methods for describing these anions. We will also establish that tetracyanoethylene (TCNE) possesses a correlation-bound anionic state.

2.2 THEORETICAL METHODOLOGY

For both the $(H_2O)_4$ cluster model and for CO_2 the theoretical methods considered include Hartree-Fock (HF), second-order Möller-Plesset (MP2),[2] second-order algebraic diagrammatic construction (ADC(2)),[4] coupled-cluster singles-doubles (CCSD), CCSD with perturbative triples CCSD(T),[3] equation-of-motion MP2 (EOM-MP2),[9,10] equation-of-motion CCSD (EOM-CCSD),[5] orbital-optimized MP2 (OMP2),[6,7] and Brueckner coupled-cluster
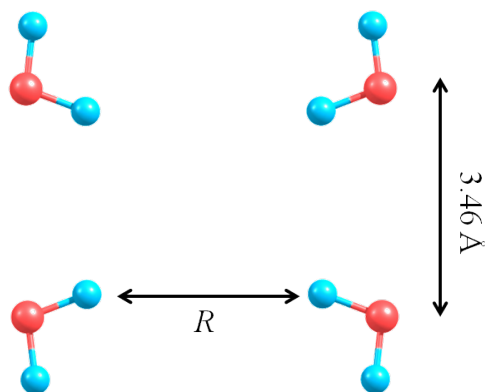
Figure 2.1: $(H_2O)_4$ cluster model studied in this work.

doubles with perturbative triples (BCCD(T)).[8] For each of these methods, except EOM-MP2, EOM-CCSD and ADC(2), the energies of the neutral and anionic systems were calculated, and the electron binding energy (EBE) was obtained from $E_{neutral}$-E_{anion}.

In the EOM-MP2 and EOM-CCSD methods, the energy of the neutral system is calculated using the MP2 and CCSD methods, respectively. The resulting doubles amplitudes are then used to perform a similarity transform of the Hamiltonian, and a CI calculation involving all symmetry-allowed one-particle ($1p$) and two-particle-one-hole ($2p1h$) configurations is carried out using the transformed Hamiltonian to describe the anion. The eigenvalues of such a CI matrix directly gives the EBE. ADC(2) also gives the EBE directly. In the OMP2 method the orbitals are optimized in the presence of the second-order correlation effects, whereas the Bruckner-coupled-cluster doubles with perturbative triples (BCCD(T)) method calculates the coupled-cluster energies using orbitals that eliminate single excitations to all orders in the inter-electron interaction. In the case of $(H_2O)_4$ calculations were also carried out using a restricted SDCI procedure described below.

For $(H_2O)_4$ model two different Gaussian basis sets were employed: aug-cc-pVTZ[16,17] and aug-cc-pVDZ+$7s7p$, where the $7s7p$ denotes a supplemental set of diffuse primitive Gaussian functions located at the center of mass of the cluster. The s and p exponents of the $7s7p$ set of Gaussians range geometrically from 0.025 to 0.000025 and 0.022 to 0.000022, respectively. For CO_2 an ANOTZ[18]+$3s3p$ basis set was employed. In this case the three diffuse s and three diffuse p functions, taken from ref [19], were included on each atom.

The EOM, BCCD(T), MP2, and CCSD(T) calculations were carried out using the CFOUR code,[20] and the OMP2 and r-CISD calculations were carried out using the PSI4 code.[21]

2.3 ELECTROSTATIC-BOUND TO CORRELATION-BOUND: THE CASE OF $(H_2O)_4$

The $(H_2O)_4$ cluster model employed in this work is depicted in Figure 2.1. The geometrical parameter, R, which gives the separation between two water dimers, is varied from 2.5 to 8.0 Å. For $R \geq 4.2$ Å, the anion is bound in large-basis-set HF calculations, while for shorter distances, it is not, and the lowest energy HF solution for the excess electron system corresponds to the neutral plus an electron in the continuum. Before considering further results obtained with the aug-cc-pVDZ+$7s7p$ basis set, it is instructive to first consider the results obtained using the aug-cc-pVTZ basis set, for which the anion does not bind at any R value in the Hartree-Fock approximation (Figure 2.2). In spite of the failure of HF approximation to bind the excess electron, all of the considered wave-function based theoretical methods including correlation effects bind the anion for R values ranging from roughly 2.0 to 5.5 Å. This is a consequence of the fact that with the aug-cc-pVTZ basis set the lowest unoccupied molecular orbital (LUMO) is artificially constrained to have considerable weight in the vicinity of the water monomers, leading to a sizable correlation contribution. The absence of highly diffuse functions in the basis set eliminates the problem of collapse of the LUMO onto a continuum solution, but the resulting electron binding energies are significantly underestimated compared to the results obtained with the aug-cc-pVDZ +$7s7p$ basis set. Moreover, for $R \geq 5.5$ Å the anion is predicted to be unbound when using the aug-cc-pVDZ basis set.

Figure 2.3 summarizes the results of the calculations with the aug-cc-pVDZ+$7s7p$ basis set. While the two EOM methods bind the excess electron for all R values considered, giving similar EBE values, the Koopmans' theorem (KT)[1], HF, MP2, CCSD, and CCSD(T) methods bind the excess electron only for R values greater than about 4.2 Å. Strikingly, the maximum value of the EBE obtained with the two EOM methods occurs near $R = 4.2$ Å,
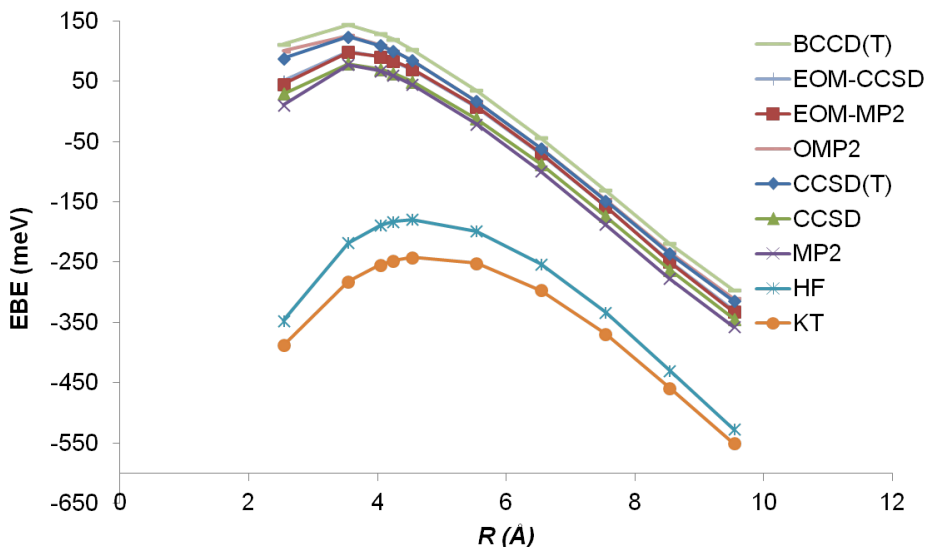
Figure 2.2: EBE of $(H_2O)_4$ calculated using various theoretical methods methods employing the aug-cc-pVTZ basis set.

the distance at which the excess electron ceases to bind in the Hartree-Fock approximation. For R values for which the HF method binds the excess electron, the CCSD(T) method gives EBEs close to the EOM results, while the CCSD method typically under-binds the excess electron over this range of R values. The success of the coupled cluster methods for R values greater than 4.2 Å is due to the ability of the single excitations to relax the "singly-occupied" orbital of the anion. The MP2 method also binds the excess electron for $R \geq 4.2$ Å, but the resulting EBE is underestimated by about 20% at $R = 9.5$ Å, with the error growing as R decreases. This growing error in the MP2 values of the EBE with decreasing R value is due to the inability of the MP2 approach to relax the singly-occupied orbital of the anion. Additional insight is provided by examination of the LUMO from the HF calculations on the neutral cluster and the singly-occupied natural orbital (SONO) from the EOM-MP2 calculations on the anion as described by the aug-cc-pVDZ+7s7p basis set. Figure 2.4 depicts these orbitals for $R = 2.5$, 3.5, 4.5, and 8.5 Å over the entire range of R values, the charge associated with the SONO from the EOM-MP2 calculations is almost entirely contained in a region within 20 Bohrs of the center of the cluster. For R = 2.5 and 3.5 Å, the LUMO from the Hartree-Fock calculations is much more extended
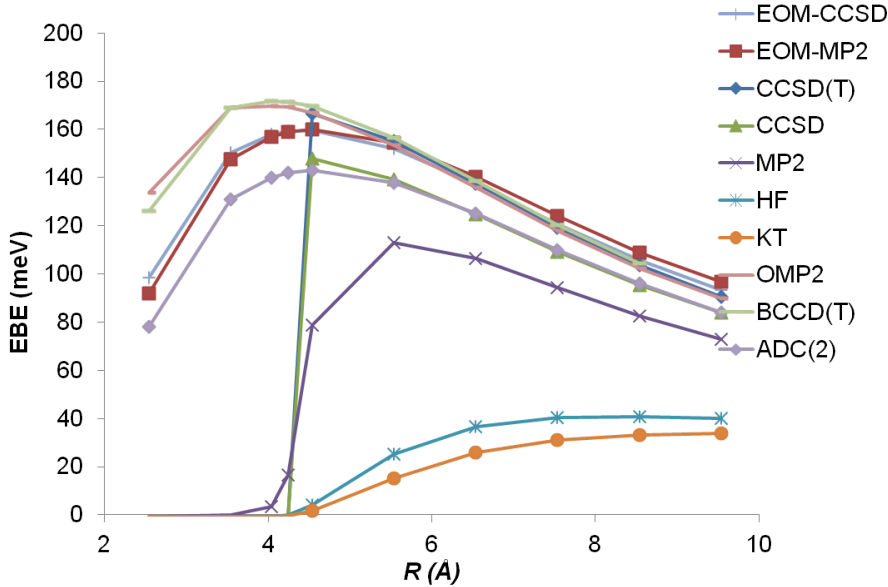
Figure 2.3: EBE of $(H_2O)_4$ calculated using various theoretical methods methods employing the aug-cc-pVDZ+7s7p basis set.

than the SONO from the EOM-CCSD calculations as a result of its corresponding to an approximate continuum function. In fact, at $R = 3.5$ Å it is the sixth empty orbital from the HF calculations of neutral $(H_2O)_4$ which most closely resembles the SONO from the EOM-CCSD calculations.

Both the OMP2 and B-CCD(T) methods give stable anion even when the singly occupied orbital from the Hartree-Fock calculation of the anion corresponds to an approximate continuum function. For $R \geq 5.5$ Å, the OMP2 method and B-CCD(T) methods give EBEs close to the EOM-CCSD values. However, for $R \leq 5.5$ Å the OMP2 and B-CCD(T) methods give EBEs significantly larger than the EOM-CCSD values. It is not clear which set of binding energies is more reflective of the true value of the EBE at these short R values. These results indicate that the key to describing the $(H_2O)_4^-$ anion at R values where the Hartree-Fock method does not bind the excess electron is allowing the nominally singly occupied orbital to relax in response to the second-order dispersion-like correlation effects. In the case of ADC(2) method this relaxation is accomplished through the off-diagonal terms in the self energy. Indeed, in the absence of the off-diagonal terms the ADC(2) method

11
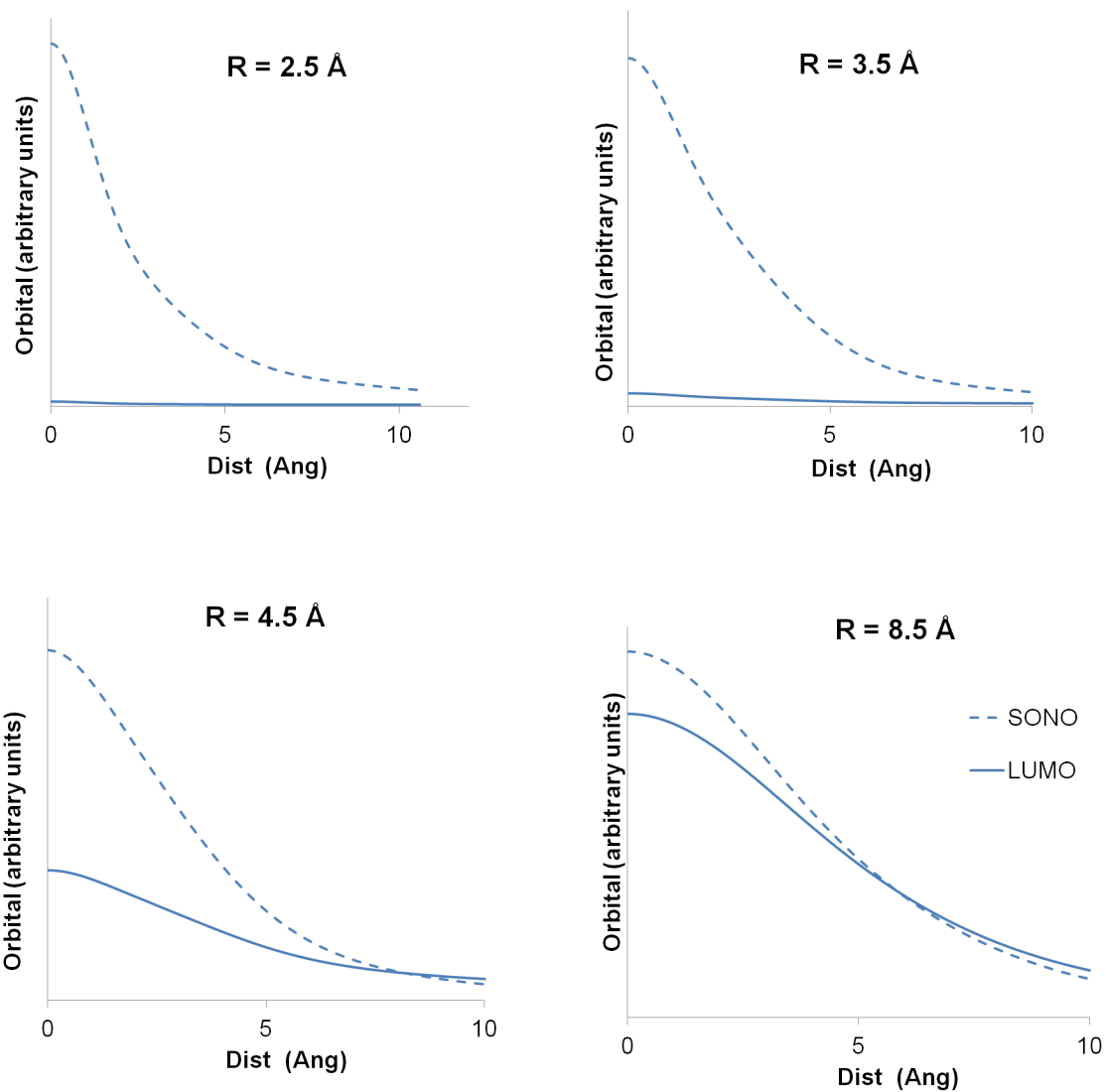
Figure 2.4: Orbital plots of the LUMO (from the Hartree-Fock calculations of the neutral $(H_2O)_4$ cluster) and the SONO (from the EOM-CCSD calculations on the $(H_2O)_4^-$ cluster) as a function of the distance from the center of the cluster toward a direction perpendicular to the plane of the cluster. The aug-cc-pVDZ+$7s7p$ basis set was used in both sets of calculations.

using the aug-cc-pVDZ+7s7p basis set fails to bind an excess electron to the $(H_2O)_4$ model for R values less than 4.2 Å. The non-self-consistent G_0W_0 method[22] also fails in this case, again due to the neglect of orbital relaxation in response to correlation effects.

In light of the results discussed above it is instructive to consider the application of the configuration interaction method to the $(H_2O)_4^-$ model system. The standard single-reference SDCI method using Hartree-Fock orbitals fails at geometries for which the excess electron is not bound in the Hartree-Fock approximation, as the anion wavefunction collapses onto the neutral plus a continuum electron. This problem can be avoided by doing for the anion a one-particle $(1p)$ plus two-particle-one-hole $(2p1h)$ CI (r-SDCI), where only single excitations are allowed from the valence orbitals and at most one electron is excited into the virtual orbitals of other than a_g symmetry. This approach accounts for the dispersion interactions between the excess electron and the electrons of the neutral cluster and also is able to convert the singly-occupied orbital from a continuum-like function to an orbital that closely resembles the SONO from an EOM calculation. Application of this approach to the anion of the $(H_2O)_4$ model system at $R = 3.5$ Å using aug-cc-pVDZ+7s7p and Hartree-Fock energy of the neutral cluster gives an EBE of 316 meV. Although this value is about 160 meV larger than the EOM-CCSD result, the SONO from the r-SDCI calculation closely resembles that from EOM calculations. The over-binding of the excess electron in the r-SDCI method primarily reflects an inadequacy of using the Hartree-Fock energy for the neutral cluster when calculating the EBE. This can be seen from an analysis of the delta-MP2 method of treating anions (using HF orbitals for both the neutral and anion), which reveals that some contributions to the correlation energy of both the neutral and anion and thus cancel in the energy difference. What remains are correlation contributions that involve various $1p$ and $2p1h$ configurations for the anion and a term that describes correlation effects in the neutral involving the LUMO. It is the neglect of the latter correlation effect involving the neutral the neutral that is primarily responsible for the r-SDCI method overestimating the EBE. This type of correlation effect also exists in the case of anions that are not bound in the Hartree-Fock approximation but one cannot limit the configuration to just those involving the LUMO. The contribution of this term can be readily evaluated by doing a restricted CI on the neutral employing the natural orbitals of the anion. With this correction the r-SDCI method gives EBEs in good agreement with

the EOM-CCSD values.

2.4 VALENCE-BOUND TO CORRELATION-BOUND: THE CASE OF CO_2

To test the broader applicability of these methods we also consider the potential energy surface of the anion CO_2 varying the OCO bond angle and C-O distance as considered in an earlier work by Sommerfeld.[19] It is well known that an electronically bound valence anion with a minimum energy structure with an OCO angle of about 135°. The anion while about 1.5 eV below the neutral molecule at the same geometry has about 0.5 eV above the neutral molecule in its minimum energy linear structure. When using a flexible basis set (here we use ANOTZ+3s3p) all theoretical methods including HF bind the excess electron for angles less than 147° (see Figure 2.5). However, the HF potential crosses the neutral potential for $\theta \sim 149°$, and, for angles greater than that, the MP2, and CCSD(T) also fail to bind the excess electron. In contrast the EOM-CCSD, OMP2 and B-CCD all bind the excess electron for OCO angles upto about 155°. The ADC(2) method binds the excess electron for OCO angles as large as 158° and at smaller angles gives much stronger binding than do the EOM, BCCD, and OMP2 methods.

2.5 NONVALENCE CORRELATION-BOUND ANION OF TCNE

TCNE is a well known electron acceptor and has an electron affinity of 3.2 eV.[23] Our EOM calculations show that TCNE also has a nonvalence correlation-bound anion with an EBE of about 0.10 eV. The SONO from the EOM-MP2 calculations on this anion state is shown in Fig. 2.6.
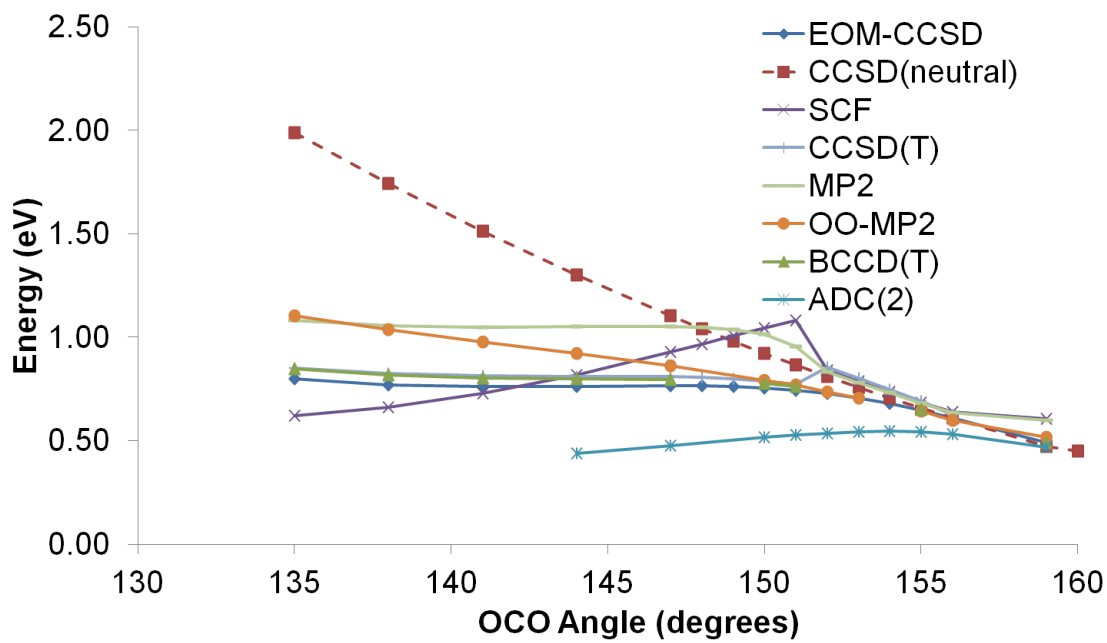
Figure 2.5: Electron binding energies of the CO_2 anion calculated using various theoretical methods as a function of a predominantly bending coordinate. The ANOTZ+3s3p basis set is used.
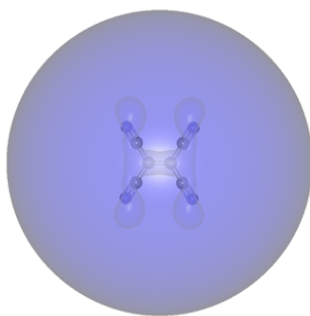
Figure 2.6: The SONO of the nonvalence correlation-bound anion of TCNE. The isosurface encloses 90% of the excess electron charge.

2.6 CONCLUSIONS

In summary, we have demonstrated that the key to binding an excess electron to a model $(H_2O)_4$ cluster to which the Hartree-Fock method does not give binding is the inclusion of orbital relaxation effects in response to the dispersion-like correlation effects. This conclusion concerning the role of orbital relaxation for binding excess electron should hold true for other systems with correlation bound anions clusters for which the Hartree-Fock method does not bind the excess electron. For the model system, the EOM-MP2 and ADC(2) methods give EBEs close to the EOM-CCSD values. The OMP2 method also gives EBEs in reasonable agreement with the EOM-CCSD values, establishing that orbital relaxation in response to low-order correlation effects are more important than higher order correlation effects describing the water cluster anions. However, for describing the polarization-bound anions of more polarizable systems such as C_{60}, both orbital relaxation in response to correlation effects and higher-order correlation effects are expected to be important for obtaining quantitative predictions of the EBEs.

2.7 ACKNOWLEDGMENTS

3.0 BENCHMARK CALCULATIONS OF THE ENERGIES FOR BINDING EXCESS ELECTRONS TO WATER CLUSTERS

This work was published as: Victor P. Vysotskiy, Lorenz S. Cederbaum, Thomas Sommerfeld, Vamsee K. Voora, and Kenneth D. Jordan, *J. Chem. Theory Comput.*, **2012**, *8*, 893-900.[1]

3.1 INTRODUCTION

There has been a long-running debate concerning the nature of excess electrons attached to intermediate sized water clusters.[24–30] At the forefront of this debate is whether experimental studies have indeed observed species with the excess electron localized in the interior of the cluster. Given the size of the clusters needed to be viable for supporting an interior bound electron and the need to account for finite temperature effects, most of the theoretical work in this area has been carried out with model Hamiltonian approaches.[31–42] This obviously leads to the question of the sensitivity of the results of the theoretical studies to the details of the model potential employed.[43] This issue has recently received considerable attention in the context of the hydrated electron in bulk water (e_{aq}^-), where a recent model potential study of this species questioned the validity of the long-accepted cavity model.[44] However, the conclusions of this study have been challenged by two other theoretical groups.[45,46] The recent debate about the nature of (e_{aq}^-) has underscored the need for high-quality ab initio data for parameterizing and testing model Hamiltonian approaches. The identities of the isomers responsible for the major peaks in the measured photodetachment spectra

---

[1]V.P.V. carried out the ADC calculations while V.K.V. carried out the EOM calculations. L.S.D, T.S. and K.D.J. contributed to the discussion.

of $(H_2O)_n^-$ clusters are known only for n ≤ 6, making accurate calculations of the electron binding energies (EBEs) of the larger clusters especially valuable. However, at the present time, accurate ab initio calculations of the EBEs e.g., using the CCSD(T) method[3] together with large basis sets have been reported only for clusters as large as $(H_2O)_6^-$.[37,47] Comparable quality theoretical data are lacking for larger clusters that are candidates for interior-bound excess electron states. The most comprehensive set of ab initio results on the EBEs of larger water clusters is that of Herbert and Head-Gordon,[48,49] who have reported MP2-level EBEs for a series of $(H_2O)_{20}^-$ and $(H_2O)_{24}^-$ clusters. These results, obtained using a 6-31(1+,3+)G basis set, formed by augmenting the 6-31+G(d) basis set[50] with diffuse s and p functions,[48,49] have proven valuable in testing model potential approaches. However, they are limited by the truncation of correlation effects at second order and by the use of a relatively small basis set. We note, in particular, that the success of the EBE calculations with the 6-31(1+,3+)G* basis set is due in part to a cancellation of errors as this basis set is not sufficiently flexible to fully describe the electron correlation effects on the EBEs but also gives a dipole moment of the monomer too large by about 0.25 D (MP2 result), which, for most geometrical structures of interest, would act so as to artificially enhance the resulting EBEs. The most ambitious calculation of an EBE of a large water cluster appears to be that of Jungwirth who recently reported an EBE of a $(H_2O)_{32}^-$ cluster obtained at the RI-MP2 level using the aug-cc-pVDZ basis set[16,17] augmented with s and p diffuse functions.[51] For a subset of $(H_2O)_n^-$ clusters for which the excess electron binds in the interior, there is an additional challenging problem in that the Hartree-Fock approximation does not bind the excess electron or binds it only weakly.[36,49] In such cases, neither the MP2 nor even the CCSD(T) method can be trusted to give reliable electron binding energies (and, in general, they will fail to bind the excess electron). This problem was recognized by Herbert and Head-Gordon who introduced a procedure that they designated MP2(BHLYP) for calculating the EBEs. This approach employs the DFT orbitals and orbital energies in the MP2 energy expressions of the neutral and anionic clusters and exploits the fact that the BHLYP density functional method[52,53] generally binds the excess electron in those cases that the Hartree-Fock method does not. The final EBEs were obtained by scaling the MP2(BHLYP) values. The accuracy of the scaled MP2(BHLYP) approach for calculating the EBEs of $(H_2O)_n^-$ clusters for which the Hartree-Fock method does not provide a suitable starting point remains to be

demonstrated. Clearly, there is a compelling need for accurate ab initio electron binding energies of $(H_2O)_n^-$, $n \geq 20$, clusters for use in testing and parameterizing model potential approaches for the accommodation of excess electrons by water. In this work we address this need by employing the second-order algebraic diagrammatic construction (ADC(2))[4] many-body Green's function method to calculate the EBEs of several water clusters, including three $(H_2O)_{24}^-$ isomers (W24a, W24c, W24e) for which the Hartree-Fock method either fails to bind the excess electron or binds it only very weakly. (In this manuscript Wn refers to the $(H_2O)_n^-$ cluster.) In addition, for a symmetrized W24a cluster, denoted W24a*, for several smaller clusters derived from the W24a*, and for two $(H_2O)_6^-$ clusters, the EBEs were calculated using the equations-of-motion electron-affinity coupled-cluster-singles-doubles (EOM-EA-CCSD)[5] and EOM-EA-CCSD(2)[10] methods, as well as with the ADC(2) method. Both the ADC(2) and EOM-EA methods are able to describe anion states for which the Hartree-Fock approximation is not a suitable starting point. However, they differ in terms of the electron correlation effects recovered. Specifically, the ADC(2) method retains only second-order terms in the expression of the self-energy of the Green's function, while the EOM-EA-CCSD includes many higher-order contributions missing in the ADC(2) procedure. The ADC(2) method is inherently size-consistent[54] and has been found to predict accurate electron binding energies for many classes of anions.[11,12,55] In addition, it has proven useful for calculating the energies and lifetimes of metastable anion states.[56,57] However, given the fact that the ADC(2) uses a second-order approximation to the self-energy, when applying to a new class of anions, it is important to compare with theoretical methods that include correlation effects missing in the ADC(2) approach. In the EOM-EA-CCSD method, one first does a CCSD calculation on the ground state of the neutral molecule, and then uses the resulting amplitudes to construct an effective Hamiltonian $e^{-T}He^T$, which is then used to carry out a configuration interaction calculation on the anion state, including all symmetry-allowed one-particle ($1p$) and two-particle-one-hole ($2p1h$) configurations. The EOM-EA-CCSD(2) method is similar except that the ground state is treated at the MP2 level, and the MP2 doubles amplitudes are used in carrying out the similarity transform of the Hamiltonian. An alternative direct equations-of-motion method for calculating electron affinities was pioneered by the Simons group.[58] Additional information on the EOM-EA-CCSD(2) calculations is provided in the supplementary information.

3.2 COMPUTATIONAL DETAILS

The ADC(2), EOM-EA-CCSD(2), and EOM-EA-CCSD methods scale as N5, N5, and N6, respectively, where N is the number of water monomers in the cluster. As a result of its relatively low scaling with cluster size, use of Cholesky decomposition,[59] and high degree of parallelization,[60] the ADC(2) method is applicable to much larger clusters than is the EOM-EA-CCSD method. Thus, it is of interest to determine if the ADC(2) method gives EBE values close to those obtained using the more computationally demanding EOM methods. For the smaller clusters for which the excess electron does bind in the Hartree-Fock approximation EBEs were also calculated using the more computationally demanding CCSD(T) method (i.e, by taking the difference of the CCSD(T) energies of the anion and neutral). The EOM-EA-CCSD and EOM-EA-CCSD(2) calculations were carried out with the CFOUR code,[20,61] and the ADC(2) calculations were performed with the P-RICDΣ code[60] which has been interfaced with MOLCAS v7.[62] The ADC(2) Dyson orbitals of the excess electron were generated with aug-cc-pVDZ+A basis set (see below for more details about basis sets used). The MP2, CCSD, and CCSD(T) calculations on the smaller clusters were performed with the MOLPRO code.[62] The clusters considered are shown in Figures 3.1-3.3. These include two isomers of $(H_2O)_6^-$, designated W6a and W6f, for which the Hartree-Fock method does bind the excess electron, two isomers of $(H_2O)_{24}^-$1 for which the Hartree-Fock method does not bind the excess electron (W24a, W24c), and one isomer of $(H_2O)_{24}^-$ for which it binds the excess electron but only weakly (W24e). In labeling these W24 clusters we have adopted the nomenclature of ref 36. In addition, we consider a series of $(H_2O)_n^-$, n = 4, 8, 12, 16 and 20 clusters, derived from W24a, which are shown in Figure 3.2 and are described below. W6a is of interest as it is the dominant isomer of $(H_2O)_6^-$ observed experimentally.[63] It has a double acceptor (AA) monomer that points two free OH groups towards the charge distribution of the excess electron. W6f$^-$ is not a local minimum on the potential energy surface of the hexamer anion, but is of interest as it has the so-called Kevan structure which has been proposed for the first hydration shell of e_{aq}^-.[64] Large basis set CCSD(T) EBEs are available for these two species.[36] The three $(H_2O)_{24}^-$ species selected for study, were considered previously by Herbert and Head-Gordon[48] and by Sommerfeld et al.,[36] are of interest as examples of clusters in which the

excess electron has considerable charge density located in the cluster interior. It is not expected that any of these three isomers corresponds to the observed $(H_2O)_{24}^-$ ion. The calculations presented in this work, with the exception of calculations of those on W24a, W24b and W24c, were carried out under the constraint of rigid monomers, i.e., with the monomer OH bond lengths and HOH angles constrained to the experimental values for the gas-phase monomer. This constraint was imposed to facilitate testing model Hamiltonian approaches employing rigid monomers. The geometry of W6a was optimized at the MP2 level under the constraint of rigid monomers, while the rigid-monomer geometries of the $(H_2O)_{24}^-$ clusters were generated by adjusting the fully optimized geometries of ref 49. The structure of W6f was constructed by hand so as to have a cavity roughly comparable in size to that of eaq- . Without the exploitation of symmetry, large basis set EOM-EA-CCSD, and even, EOM-EA-CCSD(2), calculations of the EBEs for clusters the size of $(H_2O)_{24}^-$ would be computationally prohibitive with the CFOUR code and other codes in which this approach is implemented. We note however that with the use of Cholesky decomposition and more extensive parallelization of the algorithm, such calculations would indeed be feasible even in the absence of symmetry. The optimized structure of the W24a anion is close to having D_{2h} symmetry, and to facilitate EOM-EA-CCSD calculations on this species, we adjusted the geometry to give D_{2h} symmetry. Hereafter this structure is designated as W24a*. The W4, W8, W12, W16, W20 subclusters were extracted from W24a*, and all have a common W4 core with D_{2h} symmetry. For each cluster depicted in Figures 3.1-3.3, the EBEs were calculated using the ADC(2) method. In addition, with the exception of W24a, W24b, and W24c, EOM-EA-CCSD and EOM-EA-CCSD(2) calculations of the EBEs were carried out. For the $(H_2O)_4^-$ and $(H_2O)_6^-$ clusters, EBEs are also calculated at the Koopmans' Theorem (KT), Hartree-Fock, MP2, and CCSD(T) levels of theory. The basis sets employed include aug-cc-pVDZ,[16,17] aug-cc-pVTZ, aug-cc-pVDZ+A, aug-cc-pVDZ+B, aug-cc-pVTZ+A, and aug-cc-pVTZ+B, where the A and B denote, respectively, sets of supplemental set of $7s7p$ and $6s6p6d$ diffuse functions.[65] The supplemental basis functions are located at the center-of-mass of the cluster with the exception of W6a, where they are centered on the O atom of the AA water. For the W4 and W8 clusters, EOM-EA-CCSD(2) calculations were also carried out using the aug-cc-pVQZ+A[16,17] basis set, and for the W4 cluster it was also possible to carry out EOM-EA-CCSD calculations using the aug-cc-pVQZ+B basis set,

allowing us to establish the convergence of the EBEs with basis set.

3.3 RESULTS

Table 3.1 summarizes the KT, EOM-EA-CCSD, EOM-EA-CCSD(2), and ADC(2) EBEs obtained for various water clusters. From the results reported in Tables 3.1, it is also clear that different clusters and different electron binding motifs (e.g., surface vs. interior) have very different requirements on the basis set in order to achieve convergence of the EBE. For example, for W6f, calculations with the aug-cc-pVDZ basis set give an EBE within 10% of the value obtained with the largest basis set considered (aug-cc-pVTZ+B), whereas for W6a, the EBE obtained with the aug-cc-pVDZ basis set is nearly a factor of two smaller than that obtained with the aug-cc-pVDZ+B basis set. (EOM-EA-CCSD(2) and EOM-EA-CCSD results are not reported for W6a with the larger basis sets as these calculations were not feasible with CFOUR due to the lack of symmetry.) It also appears that, with the exception of W4, near convergence in the EBEs is reached with the aug-cc-pVTZ+A basis set. In the case of W4, the inclusion of diffuse d functions at the center-of-mass (aug-cc-pVTZ+B basis set) also proves to be important, contributing 18 meV to the EBE. The adoption of the aug-cc-pVQZ rather than aug-cc-pVTZ as core basis set contributes 10 meV or less to the EBEs of W4 and W8. Such an expansion of the basis set is likely to be even less important for the larger clusters. Before discussing the results for the individual clusters, we observe that for all clusters considered, the ADC(2), EOM-EA-CCSD, and EOM-EA-CCSD(2) methods give similar values of the EBE when the same basis set is used in each case.

3.3.1 $(H_2O)_6^-$

With the aug-cc-pVDZ+A basis set, the KT, HF, MP2, and CCSD(T) EBEs of W6a are 233, 259, 361, and 422 meV, respectively. The corresponding results for W6f are 45, 254, 750, and 777 meV. These results were obtained with the supplemental functions centered on the O atom of the AA water of W6a and at the center of mass of W6f. For W6a, these values of the EBEs differ somewhat from those published in ref 36 primarily due to

the use of a structure with rigid monomers in the present study. Interestingly, although electron correlation effects are much more important for the EBE for W6f than for W6a, the change in the EBE going from the MP2 to the CCSD(T) method is more important for W6a. This is a consequence of the fact that the corrections due to triple excitations and to higher than second order double excitations enter with opposite signs for W6f but are of the same sign for W6a. Comparison of the results in Tables 3.1 and 3.2 reveals that for W6a and W6f, essentially the same EBEs are obtained with the EOM-EA and ADC(2) methods as found in the CCSD(T) calculations. This is most encouraging, given the much lower computational cost of EOM-EA-CCSD(2) and ADC(2) calculations compared to CCSD(T) or EOM-EA-CCSD calculations.

3.3.2   W24a* and its Subclusters

As noted above, EOM-EA-CCSD calculations are very computationally demanding for clusters the size of $(H_2O)_{24}^-$. Indeed, for the W24 isomers, EOM-EA-CCSD calculations were carried out only in the case of W24a* where we were able to exploit D_{2h} symmetry, and, even then, we were restricted to the aug-cc-pVDZ basis set without supplemental diffuse basis functions. The resulting EBE is close to that obtained from the ADC(2) calculations employing the same basis set (393 vs. 366 meV), providing further evidence that the computationally less demanding ADC(2) method is adequate for calculating EBEs of water clusters, even in cases where the Hartree-Fock method fails to bind the excess electron. With the ADC(2) method and the aug-cc-pVTZ+A basis set the EBE of W24a* is calculated to be 474 meV. Based on the results for the smaller clusters where larger basis sets could be employed, we expect this result to be converged to within 3% We now consider the $(H_2O)_n^-$, $n = 4, 8, 12, 16$ and 20, clusters derived from W24a*. In each case, the sub-cluster contains the same $(H_2O)_4$ core (Figure 3.2) which retains D_{2h} symmetry. In the case of W4$^-$, the Hartree-Fock approximation either fails to bind or binds very weakly (by a few meV) the excess electron depending on the basis set employed, making questionable the application of methods such as MP2 and CCSD(T) for calculation of the EBE of this cluster. Of the clusters considered, W4 binds the excess electron most weakly, with our best estimate of the EBE (described below) being 198 meV. Given the relatively small EBE value, use of a basis set with supplemental diffuse functions is especially important in this case.
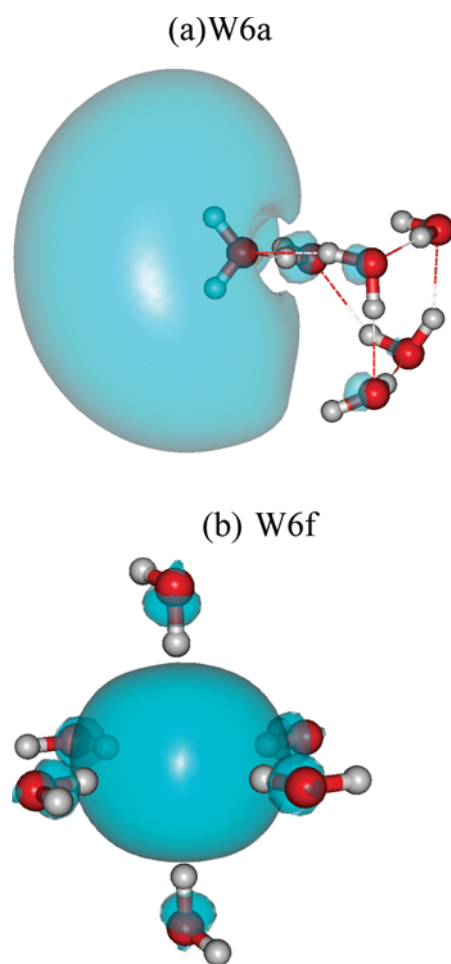
Figure 3.1: Structures of the W6 clusters studied in this work. (a) W6a, (b) W6f. The figures also display the electron density of the Dyson orbitals of the excess electron using surfaces enclosing 90% of the density.

Table 3.1: Electron binding energies (meV) of selected water clusters.

basis[a]	method	W24a* and its subclusters						W6 clusters	
		W4	W8	W12	W16	W20	W24	W6a	W6f
TZ+A	KT	<0	403	54	<0	<0	<0	231	39
DZ	ADC(2)	19	905	535	398	291	393	239	725
	EOM-EA-CCSD	37	907	551	420	298	366	250	728
DZ+A	ADC(2)	132	922	558	416	318	409	400	748
	EOM-EA-CCSD	150	920	568	432			415	744
	EOM-EA-CCSD(2)	147	922	554	403	301	366	418	744
DZ+B	EOM-EA-CCSD	181	934						
	EOM-EA-CCSD(2)	179	937	565	412	311		422	757
TZ+A	ADC(2)	163	971	611	478	376	474	424	823
	EOM-EA-CCSD	175	948						788
	EOM-EA-CCSD(2)	174	955	590					792
TZ+B	EOM-EA-CCSD(2)	192	956	593					794
QZ+A	EOM-EA-CCSD(2)	183	965						
QZ+B	EOM-EA-CCSD(2)	197							

[a]XZ = aug-cc-pVXZ, where X = D,T or Q.

Table 3.2: Comparison of electron binding energies (meV) of W4, W6a, and W6f, obtained using various theoretical methods.

Method	W4[a]	W6a[b]	W6f[b]
KT	2	233	45
HF	3	259	254
MP2	51	361	750
CCSD	166	399	717
CCSD(T)	191	422	777
EOM-CCSD	192	418	744
EOM-CCSD(2)	192	415	744
ADC(2)	192	400	748

[a]Results obtained using the aug-cc-pVTZ+B basis set
[b]Results obtained using the aug-cc-pVTZ+A basis set

Moreover, this cluster experiences the greatest increase in the EBE (25%) in going from the aug-cc-pVDZ+A to the aug-cc-pVTZ+B basis set. With the aug-cc-pVTZ+B basis set the ADC(2) and EOM-EA-CCSD(2) methods give an EBE of 192 meV for W4, whereas calculations at the KT, SCF, MP2, CCSD, and CCSD(T) levels of theory give EBEs of 2, 3, 51, 166, and 191 meV, respectively. It is remarkable that, given the very weak binding of the excess electron in the Hartree-Fock approximation, the CCSD(T) method gives an EBE essentially identical to that obtained using the EOM-EA-CCSD and ADC(2) methods. For the W4 cluster, the EBE was also calculated using the EOM-EA-CCSD method and the aug-cc-pVQZ+B basis set, giving a value of 198 meV, within 1 meV of the value obtained with the EOM-EA-CCSD(2) method. Although the W8 cluster strongly binds the excess electron at the KT level, the W12 cluster binds the excess electron only weakly and the W16, W20, and W24a* clusters fail to bind it at the KT level. Yet, all of these clusters have sizable EBEs when correlation effects are included. For example, the ADC(2) method with the aug-cc-pVTZ+A basis set gives EBEs of 971, 611, 478, 376, and 474 meV for W8, W12, W16, W20, and W24a*, respectively. Interestingly, the EBE undergoes a sizable increase in going from W4 to W8, decreases along the sequence W8, W12, W16, W20, and then

increases at W24. This behavior is the consequence of the interplay of competing factors contributing to the binding of the excess electron. Specifically, the net EBE arises from a combination of electrostatics, exchange-repulsion (including the kinetic energy contribution), induction, and dispersion interactions between the excess electron and the electrons of the water molecules. The polarization terms included in many model potentials effectively account for both the induction and dispersion contributions to the EBE.[36] For all clusters considered in this study, the electrostatic potential for the excess electron is highly attractive near the center of the cluster. In the case of the model tetramer the electrostatics contribution is comparable to the exchange-repulsion contribution, with the result that the excess electron does not bind or binds only weakly in the KT approximation, depending on the basis set used. As water molecules are added to the tetramer, the electrostatic potential near the center of the cluster can either increase or decrease, depending on the orientations of the additional water molecules. The additional water molecules also act so as to further confine the excess electron, which destabilizes it due to enhanced exchange-repulsion contributions. For the W16, W20, and W24a* clusters the confinement effect wins out, and the excess electron does not bind in the KT approximation. Thus far, the discussion has focused on the interactions present in the KT (or static exchange) approximation. Each additional water molecule also introduces attractive polarization interactions (which are dominated by dispersion-like correlation contributions). These correlation contributions are sufficiently large so as to result in stable anions even in those cases where the anion is unbound in the Hartree-Fock approximation. It is this subtle interplay of the different contributions to the EBE that makes the development of quantitatively accurate model potential approaches for describing these species especially challenging. For clusters for which the excess electron does not bind in the Hartree-Fock approximation but does bind in the ADC(2), EOM-EA-CSSD, and EOM-EA-CCSD(2) approaches, it is tempting to conclude that the anions are purely correlation bound. However, this is not the case since, if the attractive electrostatics contribution were eliminated, the excess electron would not bind or would bind only weakly. This was confirmed by model potential calculations with the electrostatic terms zeroed out. Of the W4,W8, W12, W16, W20, W24a* sequence of clusters, the excess electron is predicted to bind only to W24a* in the absence of electrostatic interactions, and then only by about 37 meV.
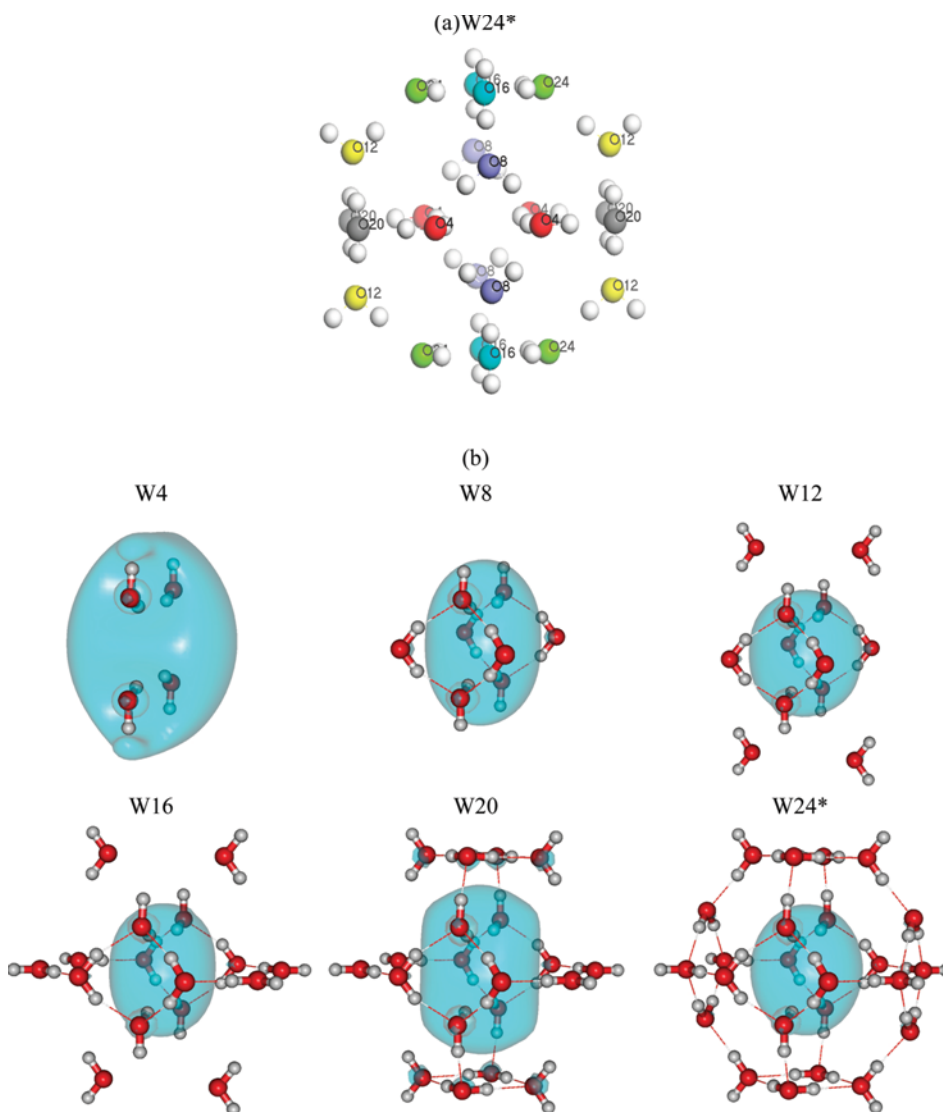
Figure 3.2: (a) W24a* and (b) the sub-clusters examined in the present work. The numbers in (a) identify the monomers retained in the W4, W8, W12, W16, and W20 subclusters, where, for example, the W8 cluster includes all molecules labeled with either 4 or 8. (b) also displays the electron densities of the Dyson orbitals of the excess electron using surfaces that enclose 90% of the density.

3.3.3 W24a, W24c, and W24e.

Table 3.3 reports for W24a, W24c, and W24e the EBEs calculated using the ADC(2) method. These results were obtained using the geometries of ref 49 (Figure 3.3), i.e. without the constraint of rigid monomers. With the aug-cc-pVDZ+A basis set, the ADC(2) calculations give EBEs of 626, 147, and 132 meV for W24a, W24c, W24e, respectively. For the three W24 isomers considered enlarging the basis set from aug-cc-pVDZ+A to aug-cc-pVDZ+B has a sizeable impact only on W24e. Here, the basis set expansion causes an increase of the EBE from 132 to 194 meV. Further enlargement of the valence basis set from aug-cc-pVDZ to aug-cc-pVTZ' (where the prime indicates that the diffuse f functions on the O atoms and the diffuse d functions on the H atoms have been omitted) leads to a further increase in the EBE of W24c, with the EBE obtained with the aug-cc-pVTZ'+B basis set being 212 meV. The ADC(2) calculations with the aug-cc-pVTZ'+A (24a and 24c) and aug-cc-pVTZ'+B (24e) basis sets (1828 and 1854 contracted Gaussian basis functions) give the most accurate EBEs to date for these clusters. Table 3.3 also reports EBEs obtained using the scaled MP2 and MP2(BHLYP) methods of Herbert and Head-Gordon.[49] Most significantly it is found that the scaled MP2 (s-MP2) approach drastically underestimates the EBE of W24c, whereas the s-MP2(BHLYP) method significantly overestimates the EBEs of W24c and W24e as compared with the results of the ADC(2) calculations. The failure of scaled MP2 approach for W24c is not surprising as that anion is not bound in the Hartree-Fock approximation.

3.4 CONCLUSIONS

The EBEs of a series of water clusters ranging from $(H_2O)_4^-$ to $(H_2O)_{24}^-$ in size were calculated using the EOM-EA-CCSD, EOM-EA-CCSD(2), and ADC(2) methods. The three theoretical were found to give similar values of the EBEs even in those cases where the Hartree-Fock approximation does not bind the excess electron. For clusters for which the Hartree-Fock method does bind the excess electron and for which CCSD(T) calculations are computationally feasible, it is found that the EBEs from CCSD(T) calculations are very close to the ADC(2) and EOM values. These results are most encouraging since the

Table 3.3: Electron binding energies (meV) of three $(H_2O)_{24}^-$ clusters calculated using the ADC(2), s-MP2 and s-MP2(BHLYP) methods.

Cluster	ADC(2)		s-MP2[a]	s-MP2(BHLYP)[a]
	DZ+A(DZ+B)	TZ'+A(TZ'+B))		
24a	626(636)	687	601	632
24b	147(162)	199	4	302
24e	132(194)	170(212)	192	316

[a]From ref 49

ADC(2) and EOM-EA-CCSD(2) methods are much less computationally demanding than EOM-EA-CCSD calculations. The major advantage of the ADC(2) method over EOM-EA-CCSD(2) is that there is a highly efficient, highly parallel implementation. This has made possible accurate calculations of the EBEs of water clusters up to $(H_2O)_{24}^-$ in size. This study also demonstrates the need to adopt large, flexible basis sets to obtain well converged EBEs of $(H_2O)_n^-$ clusters. The most challenging systems are non dipole-bound anions with a small EBE, e.g. W4, W24e. In the former case a basis set as large as aug-cc-pVQZ+B is needed to achieve a well converged value of the EBE. For W24e it is anticipated that the converged BE could be as much as 5% larger than that with the largest basis set employed for this species. For other clusters, that bind the excess electron more strongly the EBEs should be converged to within a few percent of their complete-basis-set limit values when using the aug-cc-pVTZ+A basis set. The EBEs reported in this study should prove to be especially valuable for testing model potential approaches designed for describing excess electrons interacting with water. The major problem facing traditional wavefunction-type approaches such as MP2 or CCSD(T) in describing $(H_2O)_n^-$ clusters for which Hartree-Fock method fails to give a binding or gives only a weak binding of the excess electron is that none of the virtual orbitals including the LUMO has a charge distribution that even qualitatively resembles that of the bound excess electron. This problem is especially acute when large basis sets are employed as then the low-lying virtual orbitals acquire considerable "continuum character". The key to treating such problems within an ab initio framework

(a) W24a

(b) W24c

(c) W24e
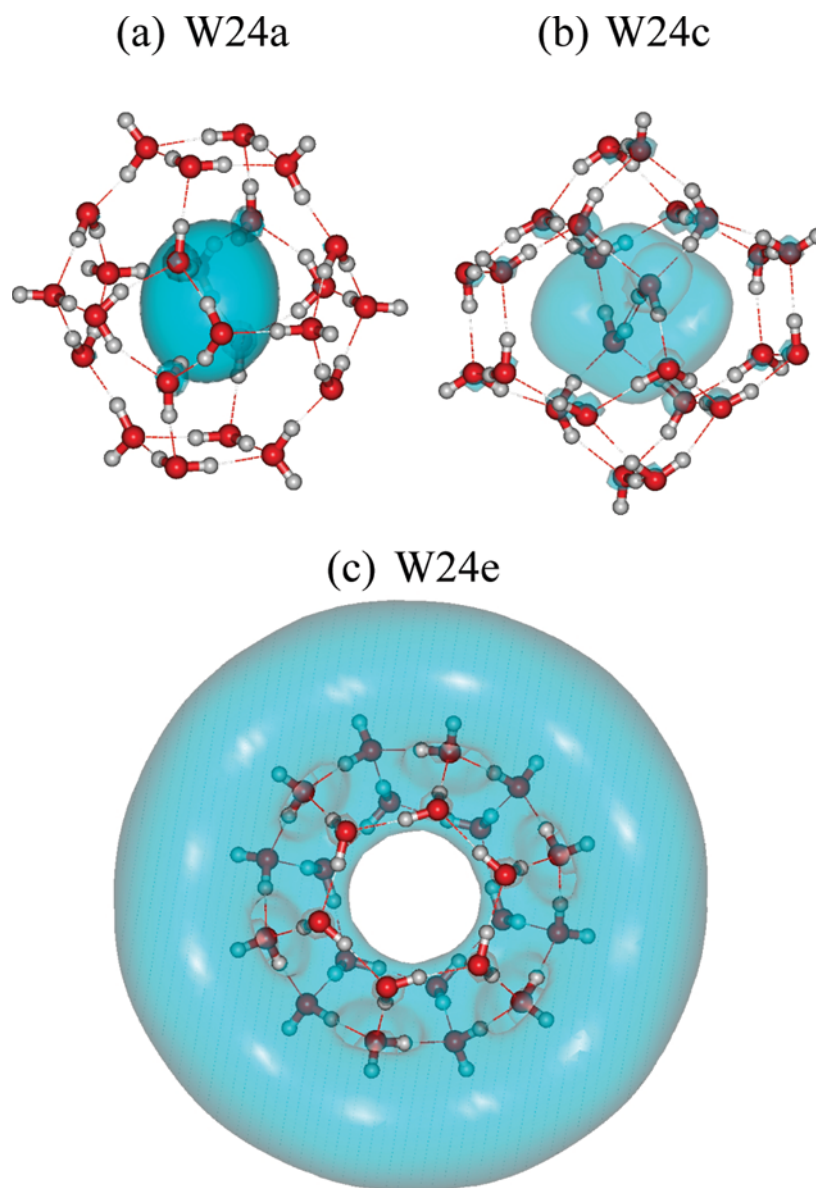
Figure 3.3: The structures of the three W24 clusters studied in this work. The surfaces indicate the electron densities of the Dyson orbitals of the excess electron using surfaces enclosing 90% of the density.

is to optimize the singly occupied orbital, allowing for the correlation interactions with the electrons of the water monomers. The resulting correlation orbital, the so-called Dyson orbital in the ADC(2) procedure, is a linear combination of the Hartree-Fock virtual orbitals of the appropriate symmetry. The success of the ADC(2), EOM-EA-CCSD(2), and EOM-EA-CCSD methods for treating this class of anions is that they account for both the long- and short-range correlation effects involving the excess electron and also allow for its relaxation in response to those correlation effects. As has been shown by Sommerfeld et al.[36] and by Simons,[66] the dominant correlation effects between the excess electron and the valence electrons of the molecules, can be viewed as generating an attractive polarization potential which when combined with the electrostatic and exchange-repulsion contributions results in a bound excess electron. Indeed, the success of the one-electron Drude[36,37,67] and polarization models[32–36,44] for treating excess electron-water systems stems from their determining the excess electron orbital in the presence of a potential, that may be viewed as a simple representation of the self-energy in the ADC(2) approach, that incorporates such correlation effects.

3.5   ACKNOWLEDGMENTS

4.0   A SELF-CONSISTENT POLARIZATION POTENTIAL MODEL FOR DESCRIBING EXCESS ELECTRONS INTERACTING WITH WATER CLUSTERS

This work was published as: Vamsee K. Voora, Jing Ding, Thomas Sommerfeld and Kenneth D. Jordan, *Journal of Physical Chemistry B*, **2013**, *117*, 4365-4370.[1]

4.1   INTRODUCTION

The nature of excess electrons in bulk water, at water interfaces, and attached to water clusters continues to be a topic of considerable debate.[24,29,43–45,68,69] Computer simulations using one-electron model potentials have played an important role in elucidating the structure and dynamics of an excess electron in water systems.[24,26,30,32,33,35,36,39,45,70,71] However, the usefulness of such simulations is directly related to the quality of the electron-water and water-water models employed. One of the most intriguing aspects of these systems is the importance of long-range dispersion-type interactions between the excess electron and the electrons of the water molecules.[72] As a result, excess electron-water systems are also valuable for exploring the use of model potential approaches for describing long-range electron correlation effects.

Over the past several years, our group has introduced two one-electron model Hamiltonian approaches for treating negatively charged water clusters.[36,37] The first approach describes the dynamical response of the electrons of the water monomers to the excess electron by means of quantum Drude oscillators.[37] The simultaneous excitation of the excess

---

electron and of a Drude oscillator describes the dispersion interaction between the excess electron and a water monomer. The second approach models the dynamical response of water molecules to the excess electron by means of a polarization potential. As shown in ref [36], a polarization potential model can be derived from the Drude model by adiabatic separation of the excess electron and the Drude oscillator degrees of freedom.

In general, our Drude and polarization model approaches give similar electron-binding energies, but for some water clusters, in particular, larger clusters with interior bound excess electrons, there are sizable differences in the electron binding energies (EBEs) calculated using the two approaches.[36] It is not known whether this is due to an inherent limitation of the polarization model or due to differences in the parametrization of the two approaches. Moreover for these problem cases, both model potential approaches give EBEs that differ appreciably from the results of high level electronic structure calculations.[15]

A major approximation of both our Drude model and polarization model approaches is the neglect of self-consistency in the electron-water and water-water interactions. The importance of such self-consistency has been noted by Jacobsen and Herbert[45] and by Stampfli.[71] In the present paper, we introduce a polarization model in which these interactions are treated self-consistently. The performance of the new model, referred to as Pol3-SC, is assessed by comparing the resulting EBEs with the results of accurate ab initio calculations for clusters as large as $(H_2O)_{24}^-$.[15] It is found that treating electron-water and water-water polarization self-consistently is especially important for the cavity-bound anions of the larger clusters.

The Pol3-SC model introduced in the present study shares several features with the recently introduced electron-water model of Jacobson et al.[35] In particular, both approaches are based on a water model with distributed mutually interacting dipole polarizable sites, although there are differences in the water-water force-fields used (the AMOEBA force-field[73] by Jacobson *et al.* and the DPP force-field[74] in our work). Both models use a spatial grid for solving the energy of the one-electron Hamiltonian. However, while Jacobson *et al.* solve for the electron-water polarization using the entire spatial distribution of the excess electron, we use an adiabatic approach in which the induced dipoles on the waters adjust to the position of the electron instantaneously. As a result our model accounts for long-range correlation interactions between the excess electron and the electrons of the water molecules,

while such correlation effects are not recovered in the SCF-type treatment of Jacobsen and Herbert. In this regard our model is actually closer in spirit to that of Stampfli.[71] Two major differences between our approach and Stampfli's are the use of three polarizable sites on the monomer in our model *vs.* one in Stampfli's model and the parameterization of our model to accurate ab initio EBEs.

4.2   THEORETICAL DETAILS

4.2.1   Description of the Present Drude and Polarization Model Approaches

Both model potential approaches developed in our group have been designed to work with the polarizable DPP water model,[74] which employs three point charges, positive charges on the H atoms, and a balancing negative charge at the so - called M site, located on the rotational axis displaced 0.25 Å, from the O atom towards the H atoms. In addition, the DPP model employs three mutually interacting atom-centered point polarizable sites with Thole-damping[75] of the charge - induced dipole and induced dipole - induced dipole interactions. Exchange-repulsion is represented by exponentials between all atoms of different molecules, and dispersion interactions are represented as damped $\frac{C_6}{R^6}$ contributions between the O atoms. The resulting one-electron Hamiltonian, in atomic units, is of the form:

$$\hat{H}^{el} = -\frac{1}{2}\nabla^2 + V^{es} + V^{rep} + V^{e-ind} + V^{dr} \tag{4.1}$$

where V^{es} accounts for the electrostatic interaction between the excess electron and the charges of the monomers, V^{rep} represents the short-range repulsion between the monomers and the excess electron, $V^{e,ind}$ couples the excess electron to the induced dipoles from water-water polarization, and V^{dr} represents the dynamic response of water monomers to the excess electron. V^{dr} is described by either Drude oscillators or polarization potentials. Because there is no coupling between the last two terms in Eq. 4.1, these models neglect changes in the water-water interactions resulting from the dynamical response of the water monomers to the excess electron.

In our applications of the Drude oscillator approach, we employed a single Drude oscil-

lator per water monomer located at the M-site, giving a coupling term of the form

$$V^{dr} = \sum_o \frac{Q\mathbf{R}_{oe} \cdot \mathbf{R}_{\mathbf{o}}^D}{(R_{oe})^3} f(R_{oe}) \tag{4.2}$$

where, $\mathbf{R}_{oe}$ determines the position of the electron relative to the oscillator, $\mathbf{R}_o^D$ determines the location of the displaceable fictitious charge, $-Q$, with respect to a countering fictitious charge $+Q$ fixed at the o site, and $f(R_{oe})$ is a damping function that attenuates the unphysical behavior as R_{oe} goes to zero.

The parameters in the Drude model consist of b which controls the damping of V^{dr} by f and a parameter γ which scales the repulsive potential, as well as the force constant k, mass m_D, and the fictitious charge Q associated with the Drude oscillator. The polarizability of the Drude oscillator α_D is given by Q^2/k and is taken to be equal to the experimental value of the isotropic polarizability of water. In our applications of the method, Q has been taken to be $+1$, which fixes the value of k. With these assumptions, the excitation energy of the Drude oscillator, ε_D is 8.7 eV, a reasonable value for the mean excitation energy of a water monomer. A perturbative analysis shows that the classical polarization contribution of the excess electron-water interaction depends on Q^2/k but not on ε_D.[37] However, the dispersion energy in the Drude model depends on both Q^2/k and ε_D, which means that it acquires a dependence on m_D. The EBEs calculated with the Drude model, at least for the small $(H_2O)_n^-$ clusters, tend to be relatively insensitive to the choice of m_D, and in our applications of this approach we have used $m_D = m_e$.

In most polarization model approaches, the interaction potential between the excess electron and a polarizable site i is described by a term of the form

$$V^{dr}(R_{ie}) = -\frac{\alpha_i}{2R_{ie}^4} g(R_{ie}) \tag{4.3}$$

where, α_i is the dipole-polarizability of the ith site, and $g(R_{ie})$ is a damping function to remove the divergence as R_{ie} tend to zero. An alternative to the use of a damping function is the inclusion of a shift parameter in the denominator.

In ref 36 it was shown that, the interaction of an electron with a single Drude oscillator gives rise to an adiabatic potential of the form,

$$V_{ad}(r) = \varepsilon_D - \sqrt{\varepsilon_D^2 + \frac{\varepsilon_D \alpha_D}{r^4} f^2(r)}, \tag{4.4}$$

where f(r) is the damping function used in the Drude model. Thus it is seen that the adiabatic potential depends on both Q^2/k and ε_D, which for a fixed k value means that it depends on m_D. A Taylor series expansion of this potential, retaining only up to the leading term in α_D, gives the traditional polarization potential of Eq. 4.3.

4.2.2 Pol3-SC Model

As noted above, the quantum Drude and polarization models introduced by our group in the past do not treat the water-water and electron-water interactions self-consistently. This limitation is removed in the Pol3-SC model in which the potential for electron-water interaction, $\hat{V}^{e-w}$, consists of electrostatic, repulsion, and self-consistent polarization terms:

$$\hat{V}^{e-w} = -\sum_i \frac{q_i}{R_{ie}} f_{pc}(R_{ie}) + \sum_i V_i^{rep}(R_{ie}) - \frac{1}{2}\sum_{ij}(V_{ij}^{e-w,pol}(\mathbf{R}_{ie},\mathbf{R}_{ij}) - V_{ij}^{w-w,pol}(\mathbf{R}_{ij})), \quad (4.5)$$

where the first term on the right-hand side represents the electrostatic interactions between the electron and the charge sites on the monomers, the second term represents the short-range repulsive interactions between the electron and atomic sites, and the third term is the electron-water self-consistent polarization potential, which is described in detail below. f_{pc} damps the electrostatic interaction at short-range and is necessitated by the use of a discrete variable representation (DVR) basis set.[76] The repulsive potential associated with each monomer was determined using the procedure described in ref 37 and is represented in terms of four s-type Slater functions on each atom:

$$V_i^{rep} = \sum_{k=1}^4 a_k e^{-\xi_k R_{ie}}. \quad (4.6)$$

In our earlier work a Gaussian-type basis set was employed to describe the wave-function of the excess electron and the repulsive potential was represented in terms of Gaussian functions to facilitate evaluation of the resulting integrals. In the present work a DVR grid basis set is employed, with the consequence that it is advantageous to use a Slater function representation of the repulsive potential.

Because the DPP water model employs three polarizable sites per monomer, the implementation of a fully self-consistent treatment of the electron-water and water-water polarization necessitates the use of three polarizable sites per water for describing electron-water

polarization. This is in contrast to our earlier polarization model which employed a single polarizable site per monomer for describing electron-water polarization. The short-range divergence of the electron-water polarization interaction is avoided by replacing R_{ie} with $R_{eff}(R_{ie})$ where, the effective distance, R_{eff} is defined as

$$R_{eff}(R) = \begin{cases} R, & if\ R \geq d; \\ d\left(\frac{1}{2} + \left(\frac{R}{d}\right)^3 \left(1 - \frac{R}{2d}\right)\right), & if\ R < d. \end{cases} \tag{4.7}$$

The net polarization potential is:

$$\frac{1}{2}\sum_{ij} V_{ij}^{e-w,pol}(\mathbf{R}_{ie}, \mathbf{R}_{ij}) = \frac{1}{2}\sum_{ij}(\mathbf{E}_i^e(\mathbf{R}_{ie}) + \mathbf{E}_i^w(\mathbf{R}_i))\cdot(\boldsymbol{\alpha}_{ii}^{-1} - \mathbf{T}_{ij}^{(2)}(\mathbf{R}_{ij}))^{-1}\cdot(\mathbf{E}_j^e(\mathbf{R}_{ie}) + \mathbf{E}_j^w(\mathbf{R}_j)), \tag{4.8}$$

where, $\mathbf{E}_i^w$ is the static electric field at site i due to the charge sites of the other water molecules, and $\mathbf{E}_i^e$ is the electric field on the atomic site i due to the excess electron. $\mathbf{R}_{ij} = \mathbf{R}_i - \mathbf{R}_j$ is the distance vector between sites i and j, $\boldsymbol{\alpha}_{ii}$ is a matrix of the site polarizabilities, and $\mathbf{T}_{ij}^{(2)}$ is the interaction matrix between induced dipoles on sites i and j. In the absence of the electron, Eq. 4.8 reduces to the polarization potential for water-water interactions, $V^{w-w,pol}$, which, of course, does not contribute to the electron binding energy and is already included in the water force-field. The polarization potential for the excess electron is given by the difference between $V^{e-w,pol}$ and $V^{w-w,pol}$. In the absence of the interaction between induced dipoles on different water molecules (i.e., $T_{ij} = 0$), the inverse matrix in Eq. 4.8 becomes diagonal and the polarization potential reduces to

$$\frac{1}{2}\sum_i V_{e-w}^{pol}(\mathbf{R}_{ie}) = \frac{1}{2}\sum_i \mathbf{E}_i^e \cdot \boldsymbol{\alpha}_i \cdot \mathbf{E}_i^e = \frac{1}{2}\sum_i \frac{\alpha_i}{(R_{eff}(R_{ie}))^4}. \tag{4.9}$$

Therefore, one can view the electron-water polarization term as having three contributions: interaction of the electron with the induced dipoles from water-water interactions, polarization of the water monomers by the excess electron, and the cross terms that allows the water-water interaction to adjust to the electron-water interactions.

In addition to the Pol3-SC model, we report results for three other models, designated Pol1, Pol3, and Pol1-SC. Pol1 uses a single polarizable site per monomer and Pol3 three polarizable sites per monomer for treating the electron-water interactions. Neither of these

models allows for a self-consistent treatment of electron-water and water-water polarization. The Pol1-SC model, like Pol3-SC, treats electron-water and water-water polarization self-consistently but uses only a single polarizable site per monomer for describing electron-water monomer polarization. Pol1, Pol3 and Pol1-SC use the same parameterization procedure as Pol3-SC to facilitate comparison of results obtained using the various methods.

4.2.3   Parametrization of the Model Potentials

The model potentials contain three parameters: the scaling parameter γ for the repulsive potential, the parameter d in the electron-water polarization potential, and a damping parameter in the electrostatic interaction between the excess electron and water molecules. The calculated EBEs are relatively insensitive to the choice of the electrostatic damping parameter, which is arbitrarily chosen to be equal to $\sqrt{\pi}$. The scaling parameter for the repulsive potential was chosen so that for the W6a hexamer anion (see Figure 4.1), the model potential using point charges chosen to reproduce the Hartree-Fock value of the dipole of the monomer and without the electron-water polarization gives the same electron binding energy as obtained from a large basis set Hartree-Fock calculation on the neutral cluster using the Koopmans' theorem[1] approximation. The d parameter in the electron-water polarization potential was chosen such that the EBE of W6a from the model potential approach using point charges that reproduce the CCSD dipole moment of water monomer is the same as that obtained from large basis set $CCSD(T)$[77] calculations.

In the implementation of the new polarization models in our PISCES code,[78] we employ sine-type particle-in-the-box functions within a DVR approach.[76,79] The results reported in this study were obtained using an evenly spaced 80x80x80 cubic DVR grid with 80 Å sides, which is adequate to achieve well converged energies.

4.2.4   Testing of the Polarization Models for Electron Binding Energy

A series of water clusters ranging from the hexamer to selected $(H_2O)_{24}^-$ isomers was used to test the Pol3-SC and the simpler models. The geometries of the clusters were taken from our earlier studies,[15,36] and, in each case, employed rigid monomers. The ab initio methods used to benchmark the electron binding energies include the second-order alge-

braic diagrammatic correction [ADC(2)] method,[4] and second-order and coupled-cluster singles-doubles equation-of-motion methods, designated EOM-MP2[9,10] and EOM-CCSD,[5] respectively. We have recently shown that these three approaches generally give similar values of the electron binding energies of $(H_2O)_n^-$ clusters,[15] and for several of the clusters we use the ab initio results from this earlier study. The test systems include six isomers of $(H_2O)_6^-$, labeled W6a-W6f, a $(H_2O)_8^-$ cluster designated W8a, three $(H_2O)_{20}^-$ clusters, designated W20a, W20c, W20e, two $(H_2O)_{24}^-$ clusters denoted W24a and W24c, and W4, W8, W12, W16 and W20 sub-clusters extracted from W24a. For the $(H_2O)_6^-$, $(H_2O)_{20}^-$, and $(H_2O)_{24}^-$ clusters the nomenclature scheme of ref 36 is adopted. The cluster structures are shown in Figures 4.1 and 4.2. W6a-W6d, W20a, W20c, and W45s all have sizable dipole moments and surface bound anions. W20f is an example of a cluster with no net dipole, but with a surface bound anion. The remaining clusters are models for interior (i.e., cavity bound) excess electron states. W6f has the classic Kevan type structure,[64] and W8a has a closely related structure. W24a has been generated by adjusting the structure of the W24a considered previously so that the overall symmetry is D_{2h} and the monomers have the gas-phase structure.

4.3 RESULTS AND DISCUSSION

Tables 4.1 and 4.2 report the EBEs obtained with the four models and from ab initio calculations when available. From the results reported in Table 4.1, it is seen that for the clusters with surface-bound excess electrons the different model potential approaches give nearly the same value of the EBE. Moreover, for the subset of these clusters for which high level ab initio results are available the model potential and ab initio EBEs are in excellent agreement. In contrast, with the exception of W4 and W6e, for the larger clusters with cavity-bound anions, the self-consistent Pol3-SC model gives EBEs appreciably smaller than those obtained from the Pol-1 model, with the differences being 227, 270 and 451 meV for W24a, W24c, and W45i, respectively. Most importantly, the Pol3-SC EBEs are in very good agreement with the ab initio results when available. For W6a, the cluster used for the parameterization, the model potential EBEs are slightly (4-7 meV) smaller than the ab
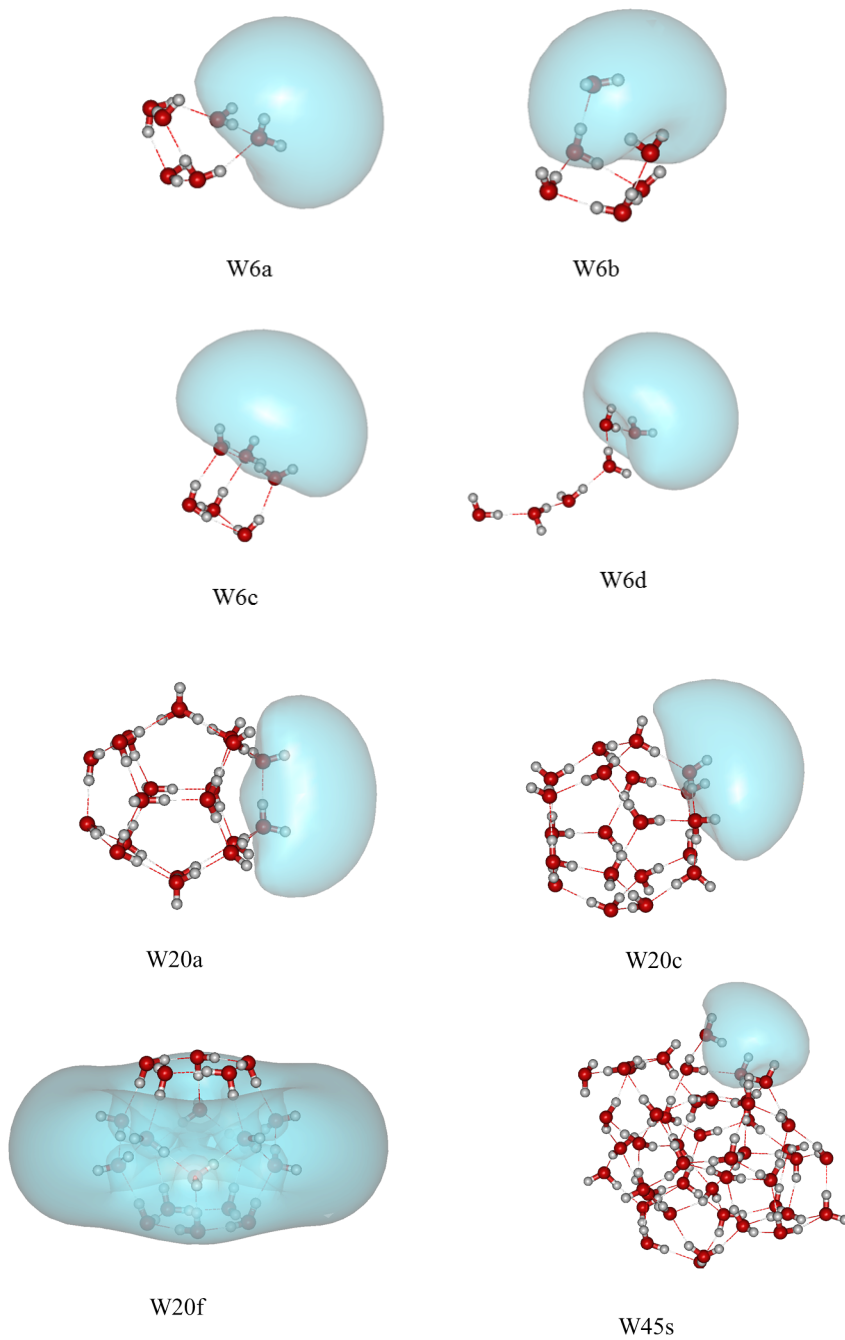
Figure 4.1: Water clusters with a surface bound excess electron. The charge densities of the excess electrons are depicted using a surface that encloses 90% of the charge.

Table 4.1: EBEs (in meV) of surface-bound excess electron states of $(H_2O)_n^-$ clusters.

Cluster	EBE				
	Ab initio[a]	Pol1	Pol3	Pol1-SC	Pol3-SC
W6a	429	423	422	425	423
W6b	572	569	567	559	559
W6c	330	346	338	344	338
W6d	349	331	328	339	336
W20a		1047	1039	1036	1029
W20c		656	650	646	644
W20f		354	347	332	327
W45s		1474	1469	1403	1394

[a]EBEs calculated using the EOM-MP2 method and the aug-cc-pVTZ basis set [16,17] augmented with a set of diffuse $6s$, $6p$, and $6d$ functions at the center of mass.

initio results reported in Table 4.1. This is simply a consequence of our repeating the ab initio calculations with a larger basis set after the model potentials were parametrized.

For W12, W16, W20, and W24a the Pol3-SC calculated EBEs are 21-49 meV larger than the ab initio results. However, for these cases much of the discrepancy is likely due to non completely converged ab initio values rather than to limitations in the Pol3-SC model. The non-convergence of the ab initio EBEs comes from two sources, (1) the use of the ADC(2) method rather than the computationally more demanding EOM-CCSD method for the larger clusters, and (2) the truncation of the atomic basis sets. Based on exploratory EOM-CCSD calculation on W16, it appears that the converged EBEs of the W12, W16, W20, and W24a model clusters could be 20-80 meV greater than the ADC(2) ab initio values reported in ref 15. For W6a, the cluster used for the parameterization, the model potential EBEs are slightly (4-7 meV) smaller than the ab initio result reported in Table 1. This is simply a consequence of our repeating the ab initio calculations with a larger basis set after the model potentials were parametrized.

It was noted above that the four model potential approaches introduced in this study
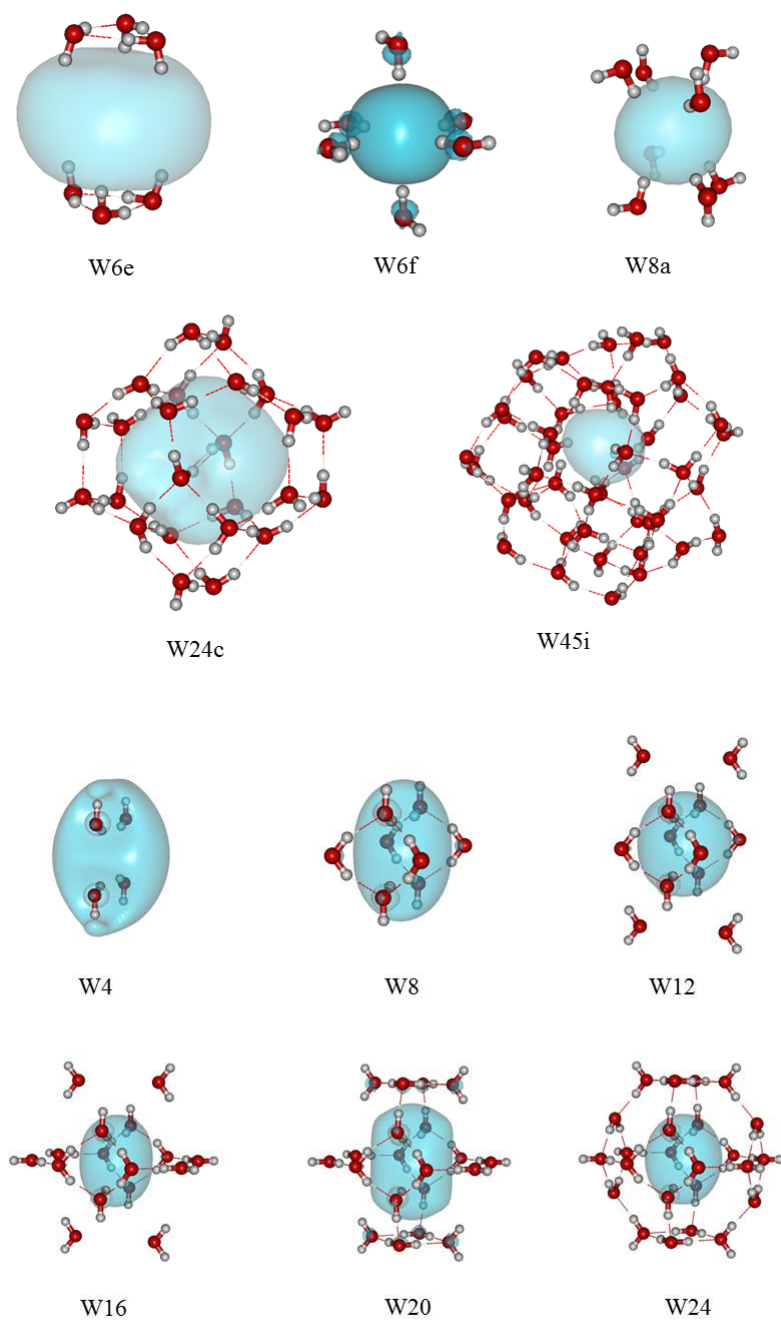
Figure 4.2: Water clusters with interior-bound excess electron. W4 has significant surface-bound character but is included here as it is derived from W24a. The charge densities of the excess electrons are depicted using a surface that encloses 90% of the charge.

Table 4.2: EBEs (in meV) of internal excess electron states of $(H_2O)_n^-$ clusters.

Cluster	EBE				
	Ab initio	Pol1	Pol3	Pol1-SC	Pol3-SC
W6e	533 [a]	563	560	540	541
W6f	823 [b]	801	903	764	831
W8a	965 [a]	984	1160	880	992
W4	197[b]	182	205	188	205
W8	965[b]	982	1018	951	984
W12	611[b]	680	727	619	660
W16	478[b]	561	616	459	499
W20	376[b]	554	579	408	422
W24a	474[b]	745	772	500	518
W24c		468	434	237	198
W45i		2500	2540	2038	2049

[a]From EOM-MP2 calculations using the aug-cc-pVTZ basis set augmented with a 7s7p set of diffuse functions located at the center of mass.

[b]From ref 15. Results for W4 and W8f are from EOM-MP2 calculations. The results for W6f and W12-W24a are from ADC(2) calculations.

give similar EBEs for the surface-bound anions. A very different situation is found for the interior-bound excess electron species. For W8 and W12-24a, the models treat electron-water and water-water polarization self-consistently give much smaller EBEs than do the models that do not. Surprisingly, with the exception of W6f and W8a, the use of three polarizable sites per monomer proves relatively unimportant. For W6f and W8a the models with three polarizable sites give appreciably larger EBEs than those employing a single polarizable site. However, the reduction in the EBE upon inclusion of self-consistent electron-water and water-water polarization is more important when the model includes three polarizable sites, with the result that the Pol1 model fortuitously gives EBEs similar to those from the Pol3-SC model and from ab initio calculations for W6f and W8a. For the larger clusters the coupling of the electron-water and water-water polarization proves more important with the result that the Pol3-SC model gives significantly smaller EBEs than obtained with the Pol1 model.

Figure 4.3 reports the electron binding energies of the sub-clusters of W24a as described by the Pol1, Pol3, Pol1-SC, and Pol3-SC models and the corresponding ab initio results from ref 15. This figure clearly demonstrates the growing importance of many-body electron-water polarization effects with increasing cluster size. This is readily understood by the unfavorable orientation of the induced dipoles on the different water monomers resulting from the polarization of the monomers by the excess electron. Allowing for interaction between the induced dipoles results in a weakening of the electron binding energy.

All model potential results discussed to this point were obtained by parameterizing the calculated EBE to W6a which has a surface-bound excess electron state. We also parametrized the four models to W8a in which the excess electron is largely cavity-bound. With this parameterization, the errors in the non-self-consistent models are roughly halved for the cavity-bound excess electron states, while there is only minor degradation of the results for surface-bound anions. This appears to be the consequence of the parameterization to W8a resulting in a weaker electron-water repulsive potential, which, in turn, leads to more strongly damped electron-water polarization interactions.

We have also tested the various models on the calculation of the electronic excitation energies of the clusters. As expected, the energies of the p-like excited states are less impacted by the self-consistent treatment of electron-water and water-water polarization than
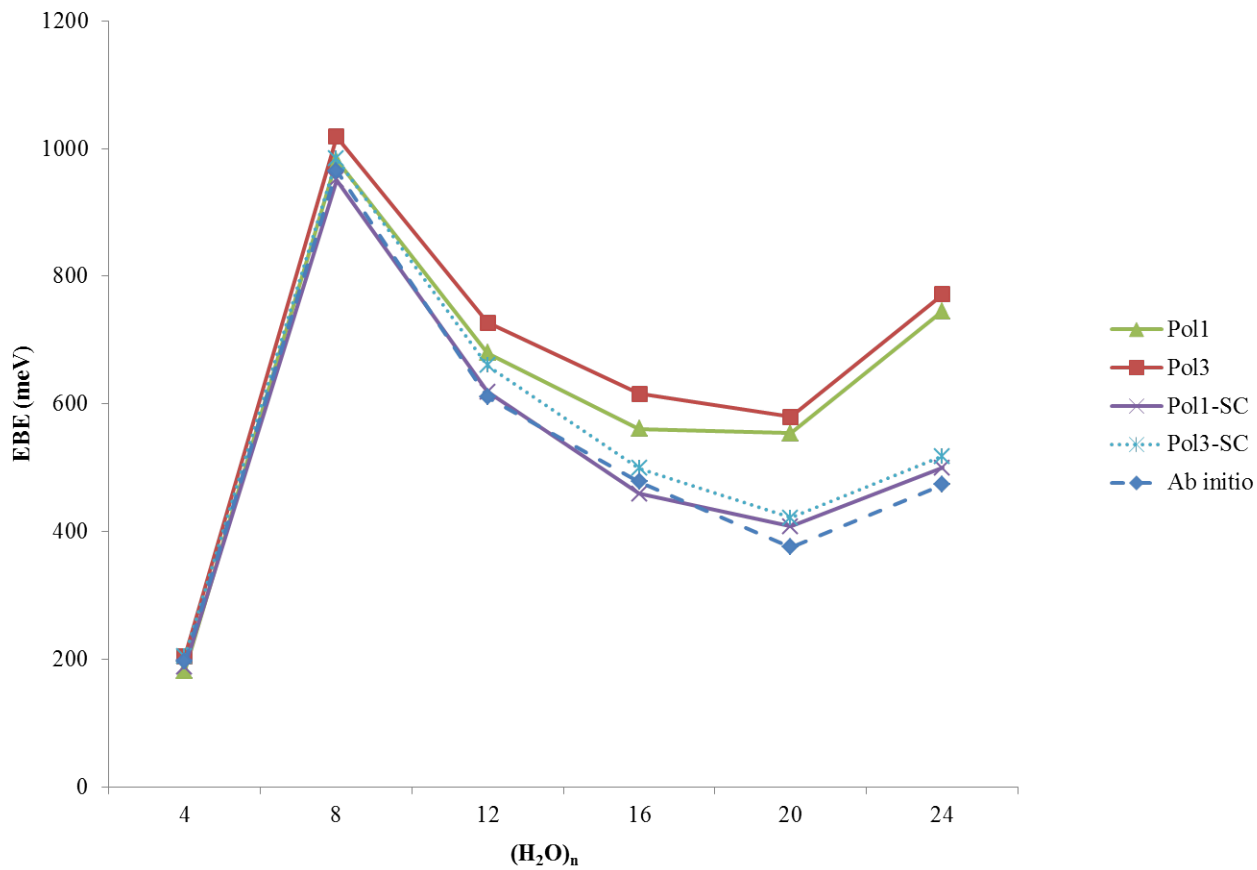
Figure 4.3: Variation in electron binding energy upon progressive build-up of the W24a cluster. Ab initio results are from ref 15

are the ground state energies. For the W45i cluster the Pol-SC model gives an excitation energy of 1.66 eV *vs.* the 1.93 eV value obtained with the Pol1 model.

4.4   CONCLUSIONS

In this work we introduced a self-consistent polarization model for the interaction of an excess electron with water clusters. The present study and those of Jacobson *et al.*[45] and of Stampfli[71] demonstrate that a self-consistent treatment of electron-water and water-water interactions is important for establishing the relative energies of the surface-bound and cavity-bound excess electron species. For a representative W45 cluster, the self-consistent treatment of electron-water interactions changes the relative stability of surface-bound and cavity-bound anions by as much as 320 meV. In that context it is interesting to note that much of the recent computational work on excess electron-solvent systems has used a non-self-consistent treatment of electron-solvent and solvent-solvent interactions.[24,36,80,81] Most encouragingly, the present work and that of ref [35] indicate that carefully parametrized self-consistent polarization models can account in a quantitative manner for the binding of excess electrons to water clusters.

One disadvantage of polarization model approaches is that they do not allow one to separate the many-body effects into dispersion, induction, and induction-dispersion contributions. To accomplish this separation it would be highly desirable to extend the Drude model described in the Introduction to account for many-body interactions involving the excess electron and two or more Drude oscillators. Efforts along this line are underway in our group.

4.5   ACKNOWLEDGMENTS

5.0 EXISTENCE OF A CORRELATION-BOUND S-TYPE ANION STATE OF C_{60}

This work was published as: Vamsee K. Voora, Lorenz S. Cederbaum, and Kenneth D. Jordan, *J. Phys. Chem. Lett.*, **2013**, *4*, 849853.[1]

C_{60} (buckminsterfullerene) has several bound valence anion states that have been the subject of numerous experimental and theoretical studies.[60,82–88] The ground state anion is highly stable, having a vertical electron detachment energy of 2.689$\pm$ 0.008 eV.[82] Given the high polarizability of C_{60}, one might anticipate that it would also have a spatially-extended s-type correlation-bound anion. A correlation-bound anion is an anion which is unbound in the Hartree-Fock approximation and for which binding occurs from dispersion-type electron correlation effects.[11,12,15,89] Within the context of model potentials such anions are often called polarization bound. The orbital occupied by the excess electron tends to be very diffuse and to have relatively little weight in the valence region. Although early electron scattering[90,91] and flowing afterglow Langmuir probe (FALP) experiments[92,93] were interpreted as indicating the absence of threshold s-wave electron capture, more recent Rydberg electron transfer, electron scattering, and FALP studies are consistent with s-wave capture near 0 eV.[94–99] C_{60}^{-} anions formed by low-energy electron capture are long-lived, consistent with a nuclear Feshbach resonance capture mechanism.[100] Thus experiments provide strong support for a low-energy long-lived nonvalence A_g symmetry anion of gas-phase C_{60}, but do not prove that the anion is bound and do not provide information on the charge distribution of this species.

Several publications have introduced one-electron model potentials for an excess electron

---

[1]V.K.V contributed the numerical data. L.S.C gave useful suggestions. K.D.J contributed to the discussion.

interacting with C_{60}.[94,95,101] Depending on the choice of parameters, these predict the s-type to be bound by a few meV to a few tens of meV. These models employ an attractive long-range polarization potential, together with a repulsive potential starting near the cage radius. A recent theoretical study of C60 using a many-body Greens function approach failed to give a bound s-type anion.[102]

STM studies of C_{60} molecules on a Cu(111) surface[103,104] have provided evidence for nonvalence s-, p-, and d-type anion states associated with the C_{60} molecules. The existence of such spatially extended anionic states is consistent with the results of two-photon photoemission studies of $C_{60}/Au(111)$ by Zhu et al.[105] Based on the STM results of ref 103, the s-type anion state of C_{60} on the Cu(111) surface is bound by about 0.94 eV relative to the vacuum level. However, the presence of the metal surface is expected to significantly impact the energy of the anion state due to image potential effects and charge transfer between the metal and C_{60}. We note also that an s-type anion state has been invoked in the interpretation of inverse photoemission measurements of solid C_{60},[106] but the main support for this interpretation was provided by the examination of the virtual orbitals resulting from a DFT calculation on neutral C_{60}, a procedure which is not expected to give accurate electron binding energies and may, in fact, artificially bind an excess electron.[107,108]

It is clear from this summary of earlier work that the stability and the nature of the charge distribution of the correlation-bound s-type anion of an isolated C_{60} molecule remain unresolved. These issues cannot be addressed using wavefunction-based electronic structure methods that assume that the Hartree-Fock approximation provides a good zeroth-order wavefunction as the s-type anion since, with a flexible basis set, the lowest $2A_g$ state from a Hartree-Fock calculation on $[C_{60}+e^-]$ corresponds to the neutral molecule plus an approximation to a continuum function. Moreover, since long-range dispersion-type interaction between the excess electron and the electrons of C_{60} are expected to dominate the correlation contribution to the binding,[11,12,15,72,109] GGA-type density functional methods are not suitable for establishing the stability of an s-type anion state of C_{60}. In the present study, we examine the binding of the s-type anion of C_{60} by employing two ab initio methods - the equation-of-motion electron-affinity MP2 (EOM-MP2)[9,10] and the equation-of-motion electron-affinity coupled-cluster-singles-doubles (EOM-CCSD)[5] methods that do not suffer from the fact that the anion is not bound at the Hartree-Fock level. The former method is

sometimes referred to as EOM-CCSD(2).[10] The EOM methods describe the anion in terms of a configuration interaction calculation involving all symmetry-allowed one-particle ($1p$) and two-particle-one-hole ($2p1h$) configurations with the matrix elements being evaluated using a similarity transformed Hamiltonian. In the case of the EOM-MP2 and EOM-CCSD methods the transformations use, respectively, the doubles amplitudes from MP2 and CCSD calculations on the ground state neutral molecule. The EOM-CCSD method obviously recovers higher-order electron correlation effects absent in the EOM-MP2 method.

All calculations were performed for a C_{60} molecule with CC bond lengths of 1.458 and 1.401 Åtaken from an electron diffraction measurement.[110] Three different basis sets were employed for the valence space. The largest of these is the $4s3p2d$ atomic-natural orbital (ANO) basis set of Roos and co-workers.[18] The two smaller basis sets, denoted mod-ANO($+s$) and mod-ANO($+sp$) delete, respectively, the outermost p and d and the outermost d functions from the ANO basis set. Even the full ANO basis set does not include sufficiently diffuse functions for describing a weakly-bound s-type anion state, and for that purpose, we also included a set of diffuse Gaussian functions at the center of mass of the molecule. Three such sets $4s4p$, $6s6p$ and $4s4p4d$ were considered. (In principle, one could describe the polarization bound anion by using sufficiently flexible atom-centered basis sets, but this would result in serious linear dependency problems.) The EOM-CCSD and EOM-MP2 calculations were carried out using the CFOUR code.[20]

Before discussing the results for the s-type anion, we consider first the results of calculations on the $^2T_{1u}$ ground state of the anion. For this species, EOM-MP2 and EOM-CCSD calculations with the mod-ANO(+s)+6s6p basis set give, respectively, electron binding energies of 2.04 and 2.48 eV. (Here we are using the sign convention that a positive electron binding energy (EBE) corresponds to a bound anion.) The EOM-CCSD result, in particular, is in close agreement with the experimental value of 2.69 eV.[82] Although the charge distributions are very different for the valence-bound and s-type anion states, these results suggest that the EOM-MP2 method is likely to underbind the s-type anion state.

Table 5.1 summarizes the EBEs for the correlation bound anion. For all basis sets considered both the EOM-MP2 and EOM-CCSD methods predict a stable A_g symmetry s-type anion, with the electron binding energy being greater with the EOM-CCSD method. The EOM-CCSD calculations with the mod-ANO($+s$)+$6s6p$ basis set gives an EBE of the

Table 5.1: Calculated EBEs (meV) of the s-type anion of C_{60}.

basis set[a]	method	
	EOM-MP2	EOM-CCSD
mod-ANO(+s)+6s6p	60	90
mod-ANO(+s)+4s4p	58	
mod-ANO(+s)+4s4p4d	64	
mod-ANO(+sp)+4s4p	67	
ANO+4s4p	82	
CBS estimate[b]	88	120

[a]The exponents of the s, p and d functions located at the center of the cluster are in a geometric series ranging from 0.005000 to 0.000884 for s, 0.010000 to 0.001768 for p, and 0.02 to 0.0034 for d.

[b]Estimate of the complete-basis-set limit electron binding energy, obtained as described in the text.

s-type anion state of 90 meV. When using the same basis set, the EOM-CCSD method provides EBEs of the s-type anion about 50% larger than those obtained using the EOM-MP2 method. This is in contrast to the situation for water clusters where the two EOM approaches give similar binding energies for an excess electron.[15] With the EOM-MP2 method expansion of the mod-ANO(+s)+4s4p basis set to include diffuse p functions on the C atoms or diffuse d functions at the fullerene center leads to increase of the EBE by 9 and 6 meV, respectively. Using the full ANO basis set (which includes on the other carbon atoms the outer s, p, and d functions) together with the +4s4p functions leads to a 15 meV increase in the EBE compared to the result obtained with the mod-ANO(+sp)+4s4p basis set. Applying these corrections, assuming additivity, to the EOM-CCSD EBE calculated with the mod-ANO(+s)+6s6p basis set, leads to an estimated EBE of 118 meV. Comparison of the basis sets used in this study to that used in ref 102 suggests that the failure of the Green's function calculations of ref 102 to give a bound s-type anion of C_{60} is the result of the use of a basis set lacking sufficiently diffuse basis functions.

In order to elucidate the charge-density distribution of the excess electron, we calcu-

lated the natural orbitals[111] of the EOM-MP2 wavefunction of the anion using the mod-ANO($+sp$)$+4s4p$ basis set. The excess electron occupies an s-type natural orbital, designated ϕ_{nat}, with an occupation of 0.992. Hereafter, we will refer to this as the singly-occupied natural orbital (SONO). Figure 5.1 plots the charge density, radial distribution function, and integrated excess charge density of ϕ_{nat} with the origin taken to be the center of the C_{60} molecule. About 9% of the charge of the excess electron is located inside and about 91% is located outside the C_{60} cage. The largest maximum in the radial distribution function occurs near 13 Bohrs, as compared to the cage radius of about 6.8 Bohrs. About 10% of the charge of the excess electron is at a distance of over 30 Bohrs from the center of the molecule. In addition to ϕ_{nat}, the anionic wavefunction has contributions from several natural orbitals with occupation numbers of 0.1 or smaller. These natural orbitals are pivotal for describing the dispersion interaction between the excess electron and the valence electrons of the C_{60}. We also note that about 5% of the charge density of the excess electron falls within the van-der-Waals shell of C_{60}, so that non-dispersion correlation effects are expected to play a non-negligible role in the binding of the excess electron.

Additional insight into the factors important for binding of the excess electron in the s-type orbital is provided by Figure 5.2 which depicts the electrostatic and polarization potentials for the interaction of a negative point charge with C_{60} as a function of the distance r from the center of the molecule (along an axis going through the bond between two six-membered rings) calculated at the HF/mod-ANO($+s$) level of theory. The polarization potential was computed by subtracting the electrostatic contribution from the net energy of the point-charge-C_{60} interaction energy. The electrostatic potential is attractive (by 1 eV) in the interior of the C_{60} cage. This is a consequence of the surface curvature causing a hybridization of the carbon "pπ" orbitals, which, in turn, results in each carbon atom acquiring a dipole moment (in a distributed multipole-type analysis[112]). The additional electrostatic attraction near the inner and outer van der Waals surfaces is due to charge penetration.[113] Most importantly, the polarization potential is attractive both inside and outside the C_{60} cage. The non-zero value of polarization potential at the cage center is a consequence of a radial shift in electron density of C_{60} induced by the presence of a point charge at the center rather than to dipole polarization. Thus both polarization and electrostatics contribute to an attractive potential for a negative point charge near the
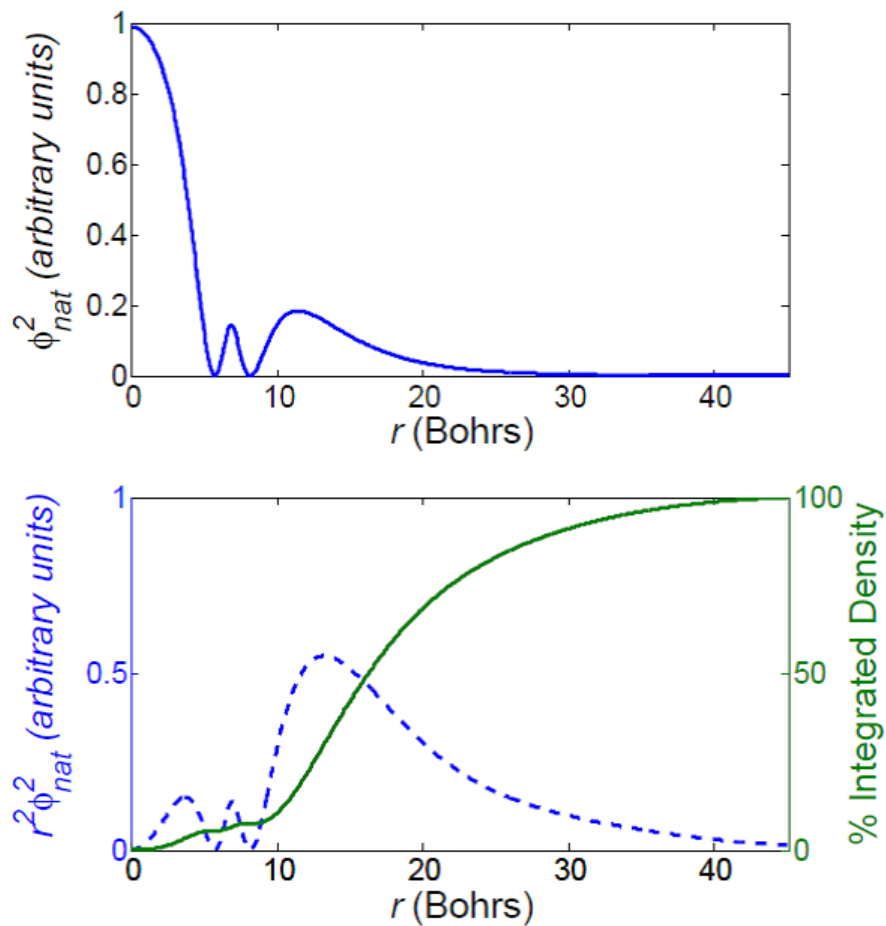
Figure 5.1: The "singly occupied" natural orbital ϕ_{nat} accommodating the excess electron in the s-like anionic state of C60. Shown are (a) ϕ^2_{nat} and (b) the radial distribution $r^2\phi^2_{nat}$ (blue) as well as the integrated density (green) as a function of the distance r from the center of the cage. About 9% of the charge is enclosed within cage. The natural or obital shown is from EOM-MP2/mod-ANO($+s$)+4s4p calculations.

center of the C_{60} cage, as has been noted before.[114] This is consistent with our finding that a significant fraction (9%) of the charge density of the natural orbital occupied by the excess electron in the s-type anion is localized inside the cage, and is in contrast to earlier model potential studies, where it was assumed the potential is repulsive inside the cage.

It is noteworthy that the beyond the outer van der Waals surface the polarization potential is much more attractive than the $-\alpha/2r^4$ potential employed in some prior model potential studies of an excess electron interacting with C_{60}.[95,101] This is a consequence of the fact that a significant fraction of the induced dipole of C_{60} is due to charge-flow polarization[113] with net electron transfer from one side of molecule to the other. This causes the point inducible dipole approximation to fail unless the distance of the point charge from the center of the molecule is appreciably greater than the diameter of the molecule. As seen from Figure 5.2, the potential outside the C_{60} sphere is well fit to $-\alpha/2r^4 - \alpha/2r^8$ where α is the experimental dipole polarizability, and β is a fitting parameter. In addition, between the origin and the inner van der Waals radius, the electrostatic plus polarization potential is well fit to (A+Br2) where A and B are 2.07 eV and 0.15 eV Bohr^2, respectively.

It is instructive to construct a model potential for the s-type anion of C_{60} incorporating the essential physics described above. In designing such a model potential, the electrostatics and polarization contributions described above were damped near the C_{60} radius and combined with a repulsive potential of the form $Cexp(-\gamma|r - R_0|)$ term, where R_0 is the cage radius, and the parameters C and γ are chosen so as to closely reproduce our best ab initio estimate of the binding energy of the polarization bound anion state. This accounts in an effective manner for the short-range (i.e., close to the carbon atoms) correlation and exchange contributions as well as the effect of orthogonalization of the a_g s-type orbital occupied in the anion state to the valence a_g orbitals. (Other authors have introduced model potentials that are much more attractive near the cage radius, [116,117] but these do not incorporate the effects of orthogonalization in the model potential and give rise to several bound a_g orbitals.) The charge distribution for the s-type excess electron orbital obtained using this model potential (shown in Figure 3.3) is similar to that of the s-type natural orbital obtained from the ab initio calculations in that most of the charge of the excess electron is localized outside the cage with a similarly peaking radial distribution.

In summary, we have reported the first ab initio calculations giving a bound 2Ag s-type
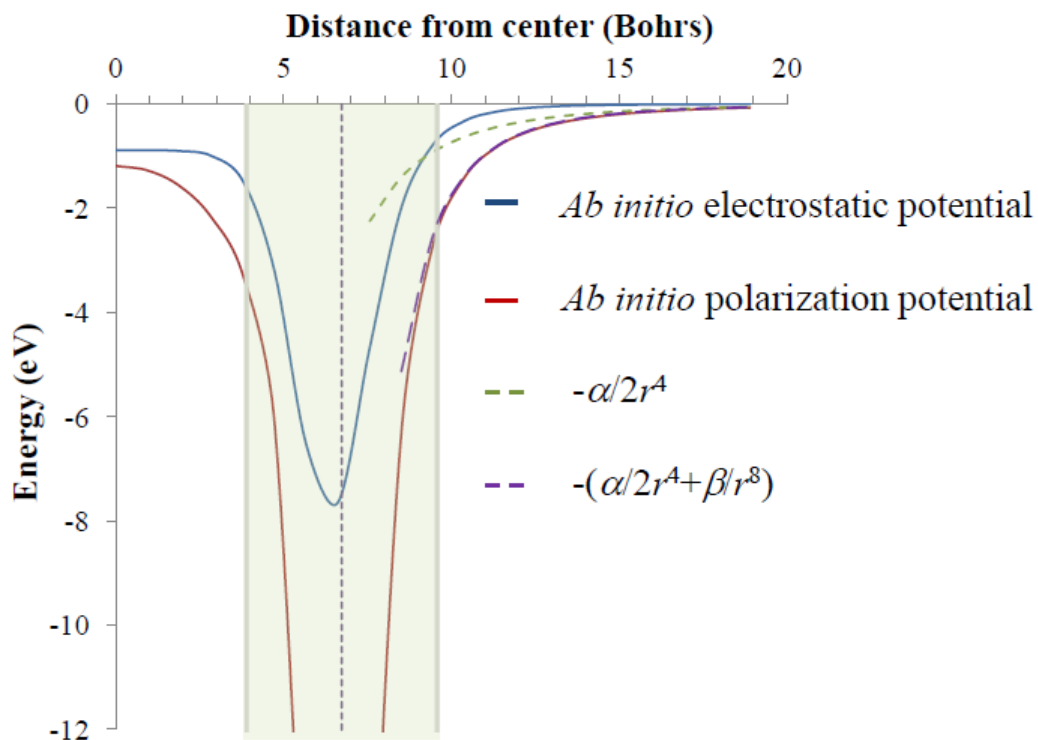
Figure 5.2: Ab initio (HF/mod-ANO(+s)) electrostatic and polarization potentials for a point negative charge along a line passing from the center of C_{60} through the mid-point of the C-C bond shared by two six-membered rings. Outside the cage the ab initio polarization potential differs significantly from $-\alpha/2r^4$ with α=540 a.u.,[115] while $-\alpha/2r^4 - \alpha/2r^8$, with $\beta = 3.75x10^6$ a.u., with distances in Bohrs, gives a good fit to the ab initio polarization potential in this region. (Energies have been converted from a.u. to eV for plotting purposes.) The vertical dashed line indicates the radius of C_{60}, and the shaded area extent of the carbon atom, as given by their van der Waals radii.
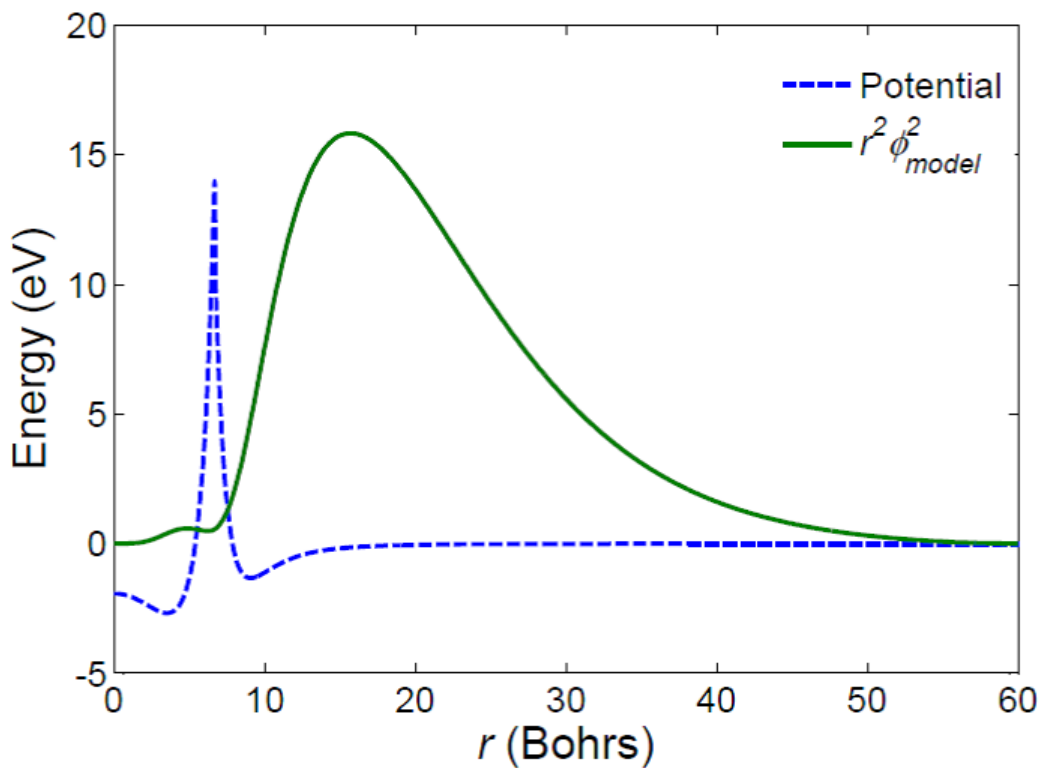
Figure 5.3: Model potential for an excess electron interacting with C_{60} (dashed blue curve) and the radial distribution (solid green curve) of the ground state eigenfunction, ϕ_{model}. The model potential was constructed by combining the electrostatic and polarization potentials shown in Fig. 2 with damping factors plus a repulsive term $C exp(-\gamma|r - R_0|)$, where R_0 is the radius of the cage. The parameters C and γ were chosen so that the resulting model potential gives an EBE close to that obtained in the EOM-MP2 calculations.

state of the C_{60} anion. Our best estimate of the electron binding energy of this species is 120 meV. At the EOM-MP2 level of theory, about 9% of the charge density of the excess electron is contained in the interior of the C_{60} cage and about 91% is outside. The ratio of interior vs. exterior charge density of the excess electron is expected to depend sensitively on the size and curvature of the fullerene as well as on whether the cage is occupied by atoms or molecules.26 To test the sensitivity of the EBE to occupation of the cage, we also carried out EOM-MP2 calculations of the s-type correlation bound anion states of the He@C_{60}, NeC_{60}, and H_2O@C_{60} endohedral complexes using the mod-ANO($+s$)+$4s4p$ basis set for the carbon atoms and the aug-cc-pVDZ[16,17] basis set for the guest species. The resulting electron binding energies are 19, 26, and 46 meV, compared to 58 meV for C_{60} at the same level of theory. The smaller electron binding energies for the endohedral complexes is a consequence of the additional node(s) of the SONO due to the presence of the guest species. The weaker binding of the excess electron for He@C_{60} than for Ne@C_{60} is somewhat surprising and could be due in part to the higher polarizability of Ne than of He. It could also be the consequence of basis set superposition error caused by the deletion of the outermost p and d functions from the ANO basis set. The H_2O@C_{60} system is particularly interesting in that one might expect the dipole moment of the encaged water molecule to act so as to enhance the electron binding. However, the induced dipole associated with the C_{60} molecule nearly cancels the dipole of the water monomer, so that the net dipole moment of H_2O@C_{60} is only about 0.5 D.[118] Hence, the long-range dipole field is relatively unimportant for the correlation bound anion of H_2O@C_{60}. We also noted that in designing one-electron model potentials to describe polarization-bound excess electron states of fullerenes, it is important to account for the attractive potential in the interior of the cage as well as to include polarization contributions beyond the dipole term outside the fullerene surface. Comparison of our result for the binding of the s-type anion of the gas-phase molecule to those for C_{60} molecules adsorbed on the Cu(111) surface[103] reveals that the s-type the anion of C_{60} is stabilized by about 0.8 eV upon adsorption of the molecule on the surface. Finally, we note that in a many-electron treatment, dispersion-type interactions between the excess electron and the electrons of the C_{60} molecule play a crucial role in the binding of the excess electron. The importance of such correlation effects has been previously noted for excess electron states of $(Xe)_n$ clusters[12] and certain $(NaCl)_n$ clusters[11] as well as for

the cavity-type excess electron states of $(H_2O)_n$ clusters.[15,89]

6.0   NONVALENCE CORRELATION-BOUND ANION STATES OF SPHERICAL FULLERENES

Bound anion states of molecules and clusters can be classified as valence-bound, electro-statically-bound, or correlation-bound depending on the nature of interaction between the excess electron and the molecule. In valence-bound anion states, the excess electron is bound by short-range interactions, while in electrostatically-bound anion states, it is bound primarily through interactions with the permanent multipole moments of the molecule(s). In nonvalence correlation-bound anion states, which are the topic of this chapter, long-range dispersion-type correlation interactions are essential for the binding of the excess electron.[11–13] By definition, correlation-bound anions states are not bound at the Hartree-Fock (HF) level of theory, and thus require the use of theoretical methods that do not depend on the HF method providing a suitable starting wavefunction. The existence of such anion states has been established for sufficiently large Xe_n clusters,[12] certain $(H_2O)_n$ clusters,[15] and, more recently, for C_6F_6[14] and the C_{60} fullerene.[13] Scanning tunneling microscopy(STM) and two-photon photo-emission studies of C_{60} and C_6F_6 on the Cu(111) surface provide evidence for very diffuse anionic states of the absorbed molecules[103,105,119,120] that we have attributed to correlation-bound anion states. In our work on the correlation-bound anion states of C_6F_6 and C_{60} the main theoretical approach was the ab initio electron attachment equation-of-motion coupled-cluster method,[5] which, due to computational demands, cannot be used for fullerenes much larger than C_{60}. A common characteristic of correlation-bound anion states is that the orbital occupied by the excess electron is very diffuse which suggests making it possible to also accurately characterize these species by use of model Hamiltonian

approaches.

In this work we present a one-electron model Hamiltonian for characterizing correlation-bound anion states of fullerenes. This is an extension of a model Hamiltonian approach that we previously introduced to characterize excess electrons interacting with water clusters.[89] The model employs polarization potentials within the context of the adiabatic approximation to account for the long-range dispersion interactions between the excess electron and the molecules.[36] Fullerenes have much smaller one-particle band gaps than water, imparting them with partial metallic character. As a result, their correlation-bound anion states can be thought of as counterparts to image-potential states of metallic surfaces,[121–124] and in the model Hamiltonian it is important to include charge-flow polarizability in addition to atom centered point inducible dipoles.[125–128] In the present work we extend our electron-water model Hamiltonian to include charge-flow polarization and parametrize it to treat correlation-bound anion states of fullerenes. Although model potentials have been introduced in the past to search for nonvalence anion states of C_{60},[94,95,101,129] these earlier models used simpler models of the electrostatics, polarization, and short-range repulsive interactions than employed in the present study. We apply the resulting model Hamiltonian to characterize the correlation-bound anion states of the C_{60}, $(C_{60})_2$, C_{240} and $C_{60}@C_{240}$ fullerene systems. The C_{60} and C_{240} fullerenes have a hexicosahedral symmetry, while $C_{60}@C_{240}$ denotes a C_{60} fullerene encapsulated inside the C_{240} fullerene.

The Hamiltonian describing the interaction of the excess electron with the fullerene is:

$$\hat{H}^{el}(\mathbf{r}) = \hat{T}^{el}(\mathbf{r}) + \hat{V}^{el-fullerene}(\mathbf{r}), \tag{6.1}$$

where $\mathbf{r}$ is the vector denoting the position of the electron, $\hat{T}^{el}$ is the kinetic energy operator, and $\hat{V}^{el-fullerene}$ the potential energy operator which consists of electrostatic, repulsion, and polarization terms:

$$\hat{V}^{el-fullerene}(\mathbf{r}) = V_{es}(\mathbf{r}) + V_{rep}(\mathbf{r}) + V_{pol}(\mathbf{r}). \tag{6.2}$$

The electrostatic potential, V_{es}, is modeled by atom-centered point dipoles:

$$V_{es}(\mathbf{r}) = -\sum_i^N \frac{\boldsymbol{\mu}_i \cdot \mathbf{R}_{ie}}{R_{ie}^3}, \tag{6.3}$$

where $\boldsymbol{\mu}_i$ is the atomic dipole moment at the ith site, $\mathbf{R}_{ie}$ is the vector between the ith site located at $\mathbf{R}_i$ and the electron at $\mathbf{r}$, and N is the number of atoms. For a graphene sheet, the leading atomic multipole moment is the quadrupole. However, for curved fullerene surfaces, a distributed multipole analysis of the charge-distribution gives finite atomic dipoles perpendicular to the surface. Although quadrupole and higher atomic multipole moments are non-negligible, we retain in our model only the atomic dipoles, fitting them to best represent the ab initio electrostatic potential at the center of the fullerene of interest. The resulting atomic dipoles are 0.0235 and 0.00965 a.u., for C_{60} and C_{240} respectively.

The repulsive potential accounts in an effective manner for exchange interactions between the excess electron and the electrons of the carbon atoms as well as for orthogonalization and charge-penetration effects. We express the repulsive potential in terms of an s-type Gaussian function on each carbon atom.

$$V_{rep}(\mathbf{r}) = -\sum_i^N a \exp(-bR_{ie}^2), \qquad (6.4)$$

where the summation is over the C atoms.

The final term in Eq. 6.2 is the polarization potential which incorporates the interaction of the excess electron with the induced moments resulting from the field from the electron on the fullerenes as well as from the interactions between fullerene molecules.

$$
\begin{aligned}
V_{pol}(\mathbf{r}) \;&= -(\mathbf{F}^e(\mathbf{r}))^T \cdot \boldsymbol{\alpha}^{fullerene} \cdot (\tfrac{1}{2}\mathbf{F}^e(\mathbf{r}) \\
&\quad + \mathbf{F}^{fullerene}) \\
&= -(\mathbf{F}^e(\mathbf{r}))^T \cdot \mathbf{M}^{ind},
\end{aligned}
\qquad (6.5)
$$

where $\mathbf{F}^e$ is a super-vector consisting of potentials, $\mathbf{V}^e$, and electric fields, $\mathbf{E}^e$, on the atoms of the fullerenes due to the electron, and $\mathbf{F}^{fullerene}$ is a super-vector that accounts for the potentials and fields between the fullerenes. $\boldsymbol{\alpha}^{fullerene}$ is the polarizability matrix of the fullerene(s) and accounts for both charge-flow and atom-centered point inducible dipoles. $\mathbf{M}^{ind}$ is a super-vector consisting of the induced charges, $\mathbf{q}$ (due to charge-flow) and the induced dipoles, $\boldsymbol{\mu}$, on the atomic sites (See Appendix B for details on $\boldsymbol{\alpha}^{fullerene}$ and $\mathbf{M}^{ind}$). The one-electron Schrödinger equation is solved using discrete variable representation (DVR) grid-type basis set[76] as implemented in the PISCES code[78] developed in our group for describing excess electron systems.

Table 6.1: EBEs (eV) of nonvalence correlation-bound anion states of fullerenes.

C_{60}	$(C_{60})_2$	C_{240}	$C_{60}@C_{240}$
0.13(s)	0.25($s\sigma_g$)	0.70(s)	0.56(s)
-0.01(p)	0.10($s\sigma_u$)	0.38(p)	0.33(p)
	0.06($p\pi_u{}^a$	0.28(s)	0.29(s)
	0.01($p\sigma_g$)	0.15(d)	0.16(d)
		0.02(p)	

[a]This state is doubly degenerate.

The model potential described above was used to characterize the correlation-bound anionic states of C_{60}, C_{240}, $(C_{60})_2$ and $C_{60}@C_{240}$. For C_{60}, the model Hamiltonian gives a single s-type correlation-bound anion state with an EBE of 0.13 eV, which, because of the use of this species in determining the parameter in the damping function for the polarization potential, is essentially identical to the EOM-CCSD result(we are using the sign convention that a positive EBE corresponds to a bound anion). The orbital occupied by the excess electron and its radial distribution function are shown in Figure 6.1. The model Hamiltonian was also used in conjunction with the stabilization method[130] to search for a p-type temporary anion of C_{60}. These calculations locate a p-type temporary anion at -0.01 eV. For the other three fullerene systems multiple correlation-bound anion states are identified (see Table 1).

For the C_{60} dimer the calculations were carried out for a 19 Bohr center-to-center separation of the molecules. This distance was chosen to match the experimentally observed distance between the C_{60} monomers of the C_{60} dimer on the Cu(111) surface.[103] The most stable correlation-bound anion state of $(C_{60})_2$ is calculated to have an EBE of 0.25 eV and corresponds to the plus combination of the s-type correlation-bound anion states of the isolated molecules (denoted as $s\sigma_g$). In addition, there are correlation-bound anion states that correspond to $s\sigma_u$, as well as to $p\pi_u$ and $p\sigma_g$ supermolecular orbitals (see Figure 6.2). The calculated splitting between the lowest energy $s\sigma_g$ and $s\sigma_u$ states of $(C_{60})_2$ is 0.15 eV, in reasonable agreement with the experimentally observed splitting of 0.26 eV for the C_{60}
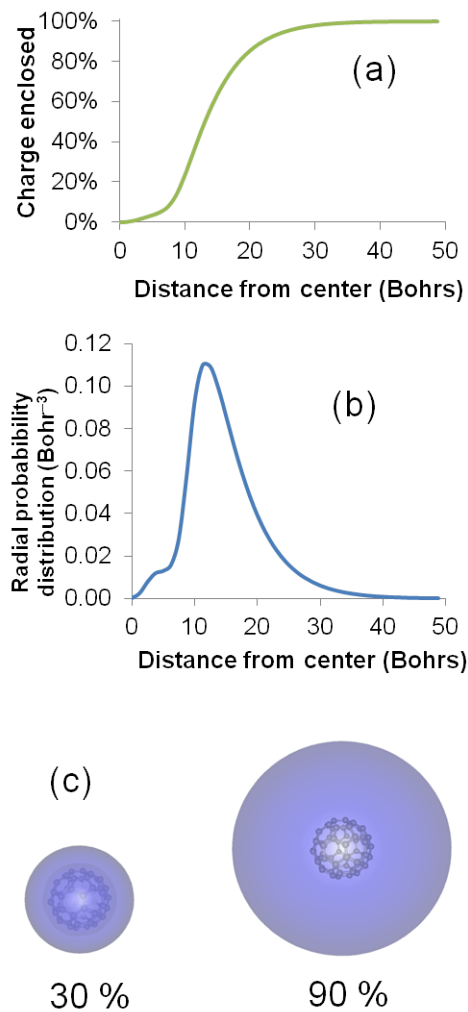
Figure 6.1: Charge distribution of the correlation-bound s-type anion state of C_{60} using the model potential. (a) shows the charge enclosed as a function of the distance from the center of C_{60} while (b) depicts the radial distribution of the excess electron. (c) illustrates the orbital occupied by the excess electron, at isosurfaces containing 30 and 90% of the charge.

dimer on Cu(111). We note also that the bound $p\pi_u$ and $p\sigma_g$ anion states of $(C_{60})_2$ can be viewed as arising from the p-type temporary anion state of C_{60}.

For C_{240}, the second smallest fullerene with hexicosahedral symmetry, the calculations give five correlation-bound anion states that are $1s$, $1p$, $2s$, $1d$ and $2p$ in nature. The most stable of these is bound by 0.70 eV which is about five times greater than the EBE of the s-state of C_{60} anion. As seen from Figure 6.3, for the lowest energy correlation-bound anion of C_{240} most of the charge density of the excess electron is localized inside the cage. The second most stable correlation bound anion of C_{240}, labeled $1p$, has significant charge both inside and outside the cage. The three higher-lying anion states have most of the charge density of the excess electron outside the cage. The existence of the correlation-bound anion states with significant charge either inside of or outside of the cage is closely related to the "+" and "-" states of graphene discussed by Silkin et al.[121]

Given the localization of the excess electron associated with the $1s$ nonvalence correlation-bound anion state of C_{240}, one could question the validity of the model Hamiltonian approach to this species. It is relevant to note, therefore, that we have previously demonstrated in the case of water clusters that our model Hamiltonian approach successfully described both the very diffuse as well as more localized nonvalence correlation-bound anion states of these clusters.[89] We note also that over 82% of the charge of the excess electron of the $1s$ state of C_{240} is outside the region defined by the inner and outer van der Waals shells of the molecule. For these reasons, we are confident that the model Hamiltonian is providing a semi-quantitatively correct description for the wavefunction and EBE of this species.

We also characterized the correlation-bound anion states of $C_{60}@C_{240}$. As expected, the lowest energy correlation-bound anion state of $C_{60}@C_{240}$ is appreciably less stable than that of C_{240} itself. This is essentially an "excluded volume" effect. On the other hand, the lowest p-type, d-type and the second s-type correlation-bound anion states of C_{240} which have most of their charge density outside the cage are relatively unimpacted by the encapsulation of the C_{60} molecule.

In order to better understand the impact of the encapsulation of the C_{60} on the correlation bound states of C_{240}, we plot in Figure 6.4 the radial distribution functions of the two lowest energy s states of C_{240} and $C_{60}@C_{240}$. As expected the lowest energy s-state of $C_{60}@C_{240}$ has more charge outside of the C_{240} cage than does the corresponding state of

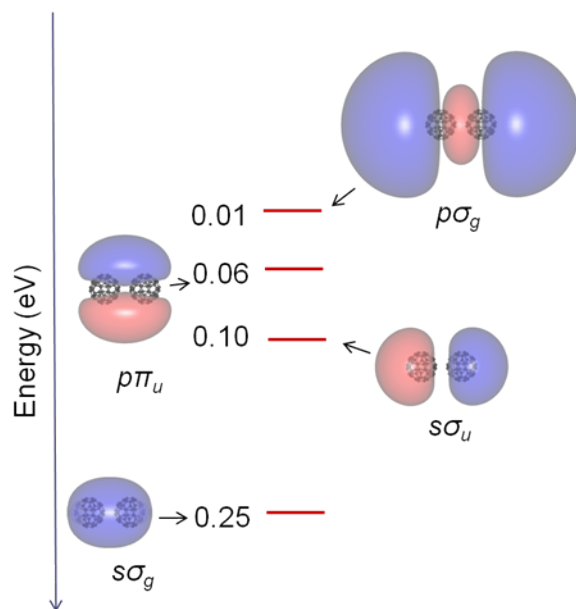Figure 6.2: Correlation-bound anion states of $(C_{60})_2$ at a center-to-center separation of 19 Bohrs between the two fullerene molecules. The orbital isosurfaces correspond to 80% of the charge of the excess electron enclosed.
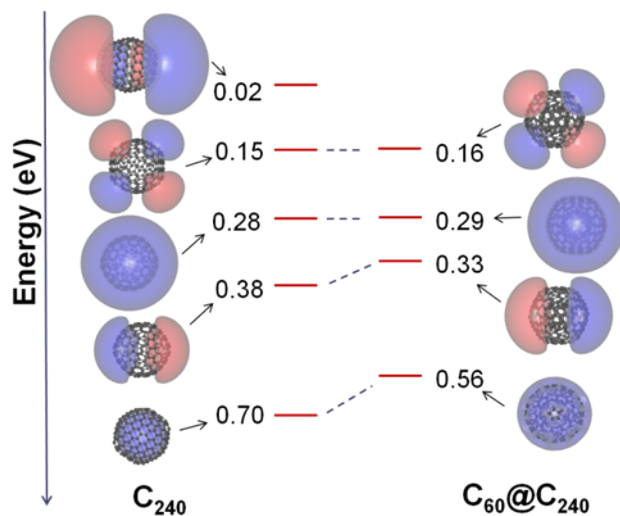

Figure 6.3: Correlation-bound anion states of C_{240} and $C_{60}@C_{240}$. The orbital isosurfaces correspond to 80% of the charge of the excess electron enclosed.
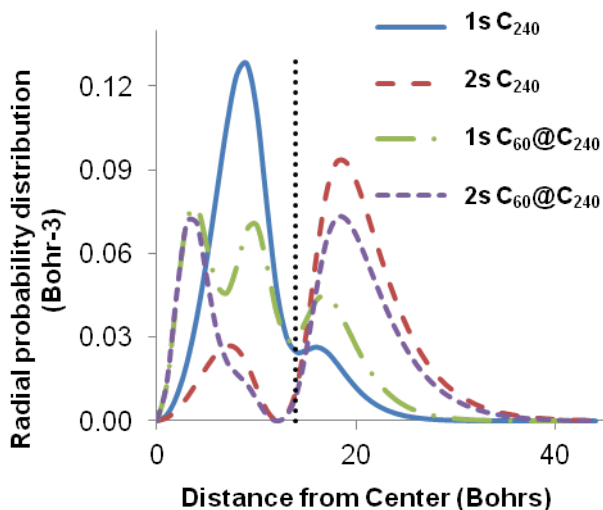
Figure 6.4: Radial distribution functions of the s-type states of C_{240} and $C_{60}@C_{240}$. The radius of C_{240} is 13.9 Bohrs.

C_{240}. However, the presence of the C_{60} also causes a shift of charge density from near the inner "wall" of the enclosed C_{240} to near the inner wall of enclosed C_{60}.

We have also separated the net EBE of each correlation-bound anion state considered into kinetic energy, electrostatics, repulsive and polarization contributions, summarizing results in Figure 6.5. For C_{60} the calculations give, respectively, values of -191, -476, 42 and 755 meV for the kinetic, repulsion, electrostatic and polarization contributions to the s-type anion state.(Here we are continuing to use the convention that positive contributions are stabilizing.) The confinement of the electron thus introduces sizable kinetic energy, and repulsive contributions. The attractive electrostatic interaction is quite small, and the stability of the s-type anion of C_{60} is mainly due to the sizable (755) polarization interaction which more than compensates for the confinement. The much stronger binding of the lowest energy s-type state of C_{240} compared to that of C_{60} is largely a consequence of the much greater polarization contribution of the latter. Not surprisingly, the individual contributions to the EBE of the lowest s-type state of $C_{60}@C_{240}$ are very different from the corresponding results for C_{240}, with the electrostatics, repulsive, and polarization contributions all being much larger in magnitude in the former. More surprising is the finding that the individual

contributions to the EBE of the $2s$ anion state of $C_{60}@C_{240}$ are very different from those of the $2s$ anion state of C_{240} itself. This is a consequence of an increase in charge density near the inner "wall" of C_{60} of $C_{60}@C_{240}$.

In this work we have introduced a one-electron model Hamiltonian for describing the highly extended correlation-bound anion states of fullerenes. The model includes both point-inducible dipoles and charge-flow polarization, both of which are important for describing the polarization potential. The model is applied to C_{60}, C_{240}, $(C_{60})_2$, and $C_{60}@C_{240}$. Whereas, C_{60} is found to have a single s-type correlation bound anion state, the larger systems have multiple correlation-bound anion states. For the C_{60} dimer, at a separation of 19 Bohrs, the model potential gives a splitting of 0.15 eV between the two lowest energy ($s\sigma_g$ and $s\sigma_u$) correlation bound anion states as compared to the 0.26 eV splitting measured experimentally for $(C_{60})_2$ on the Cu(111) surface. The discrepancy between the calculated and measured splittings suggests that the interactions of the C_{60} molecules with the Cu(111) surface, present in the experimentally studied system but lacking in the gas-phase dimer investigated here, significantly impact the splitting. In the case of C_{60}, we also located a p-like resonance which is unbound by only 0.01 eV. The model Hamiltonian developed in this work has been incorporated in our in-house PISCES code, which is freely available upon request. It can be readily extended to treat excess electrons interacting with graphene flakes and carbon nanotubes.
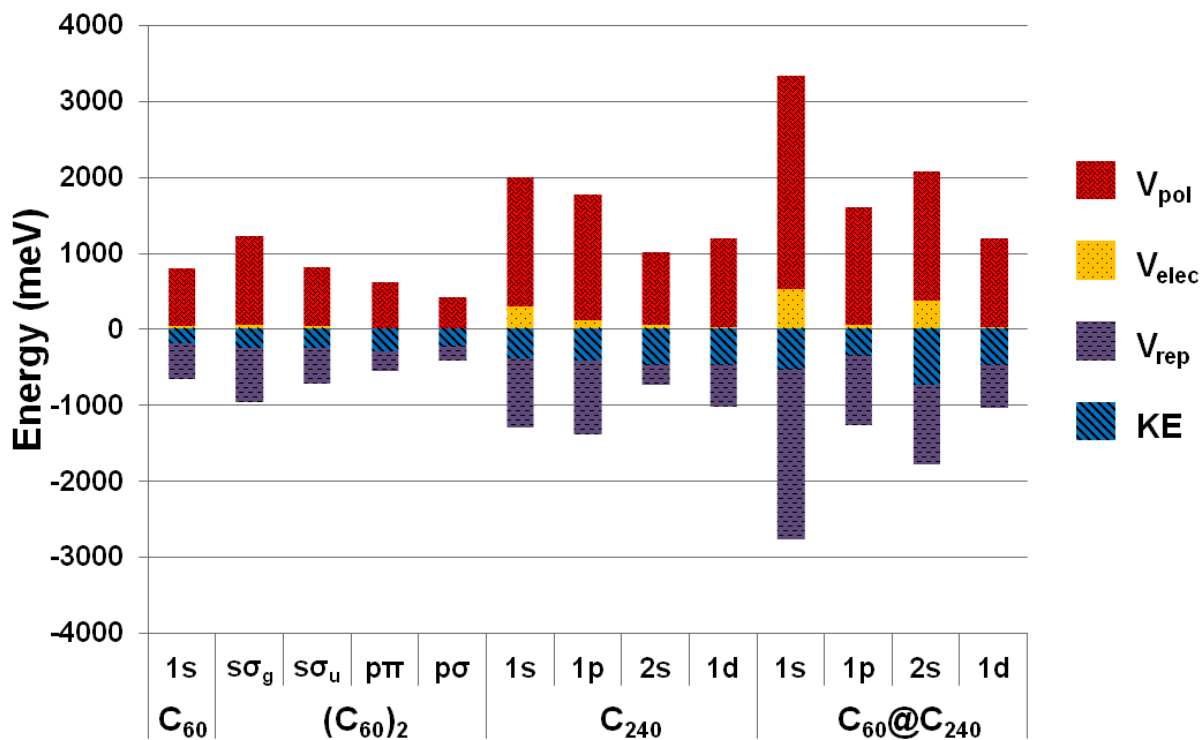
Figure 6.5: Contributions of the electrostatic, repulsion, polarization and kinetic energy(KE) to the EBE of the correlation-bound anion states of C_{60}, $(C_{60})_2$, C_{240}, and $C_{60}@C_{240}$.

7.0   NONVALENCE CORRELATION-BOUND ANION STATE OF C_6F_6: DOORWAY TO LOW-ENERGY ELECTRON CAPTURE

7.1   INTRODUCTION

The anion states of perfluorobenzene, C_6F_6, have been a subject of a large number of experimental and theoretical studies.[131–139] Electron scattering studies provide evidence for π^* anion states with vertical attachment energies of 0.42 and 4.5 eV[140–142] and do not provide evidence for a low-lying σ^* anion. Field and coworkers have concluded that C_6F_6 also has a virtual state in the *s*-wave channel.[136] (A virtual state is a state that would be bound were the potential slightly more attractive). Near threshold electron capture has been attributed to electron trapping via the nuclear Feshbach resonance mechanism,11 a process that does not require that the anion be bound at the geometry of the neutral. Indeed, C_6F_6, is known to form a stable valence-type anion with a non-planar structure and a vertical electron detachment energy of about 1.5 eV.[133,143] The adiabatic electron affinity (EA) for forming the valence anion is 0.5 eV.[132] The resulting anion is believed to have C_{2v} symmetry[132,144] as shown in Figure 7.1. In a simple molecular orbital picture the driving force of the buckling can be understood in terms of hybridization of the low-lying π^* and σ^* orbitals upon out-of-plane C_{2v} symmetry distortion. Interest in the anion states of C_6F_6 is further motivated by various liquid phase and surface science experiments. Electron mobility in liquid C_6F_6 is unusually high, and the experiments have been interpreted in terms of an anion state delocalized over many molecules.[138] Two-photon photoemission[119,145–147] and

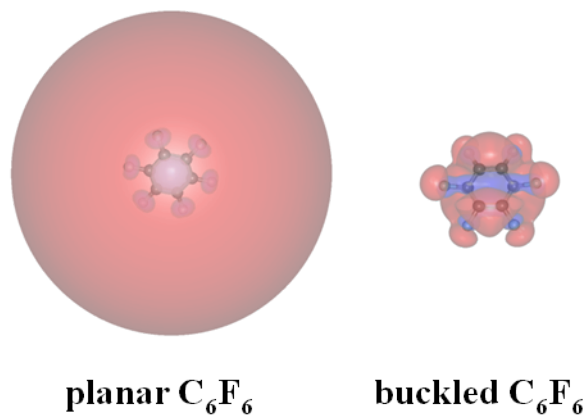**planar C$_6$F$_6$**   **buckled C$_6$F$_6$**

Figure 7.1: Isosurfaces of the singly-occupied natural orbital of C$_6$F$_6^-$ from the EOM-MP2 calculations for the correlation-bound anion (left) and the valence-bound anion (right). The surfaces shown enclose 90% of the charge density.

voltage-dependent STM[120] measurements of C$_6$F$_6$ on Cu(111) surfaces provide evidence for electron capture into a an anion state of C$_6$F$_6$ with an extended charge distribution. In some of these experimental studies the state involved was designated as σ^*, with the implication that it is valence-like in character.

In this work we investigate the possibility that C$_6$F$_6$ at its geometry supports a nonvalence correlation-bound anion state. Such anions are unbound in the Hartree-Fock approximation, but with a proper treatment of electron correlation effects, the excess electron binds in a diffuse "s-like" orbital, with the long-range dispersion-type interactions between the excess electron and the electrons of the molecule being pivotal to the electron binding. An s-type correlation-bound anion was recently demonstrated by us to exist for C$_{60}$.[13] Other correlation-bound anions have been characterized by Sommerfeld et al.[11] and Bezchastnov et al.[12] The key to describing such anions theoretically is the use of methods that allow the singly occupied orbital to relax in response to the dispersion-type correlation effects. In the present study we use the equation-of-motion coupled-cluster singles-double EOM-CCSD[5] and EOM-MP2 (often referred to as EOM-CCSD(2))[9,10] methods to characterize the lowest energy anion state of C$_6$F$_6$ and the two lowest energy anion states of (C$_6$F$_6$)$_2$.

7.2   COMPUTATIONAL DETAILS

The geometry of the neutral C_6F_6 molecule was optimized at the MP2 level using the aug-cc-pVDZ Gaussian type orbital basis set.[16,17] The EOM-MP2 method was used to optimize the geometry of $C_6F_6^-$ and to calculate the potential energy of $C_6F_6^-$ along the buckling coordinate. These calculations were performed using the aug-cc-pVDZ basis set augmented with a $7s7p$ set of diffuse Gaussian functions located at the center of the ring. The supplemental set of functions has exponents ranging from 0.025 to 0.000025 for s, and from 0.02168 to 0.00002168 for p, distributed in an even tempered manner. Single-point calculations of the electron binding energy (EBE) at the geometry of the neutral and the optimized structures of anion were carried out with both the EOM-MP2 and EOM-CCSD methods using the aug-cc-pVTZ basis set [16,17] augmented with the $7s7p$ set of functions described above. Since the EBEs obtained with the EOM-MP2 and EOM-CCSD methods are nearly identical, we report only the EOM-MP2 results here. The EOM calculations were carried out with the CFOUR[20] code.

7.3   RESULTS AND DISCUSSION

At the equilibrium geometry of C_6F_6, the EOM-MP2 calculations predict the anion to be bound by 0.135 eV (this result was obtained using the aug-cc-pVTZ+$7s7p$ basis set, and is 0.045 eV lager than the EBE obtained using the aug-cc-pVDZ+$7s7p$ basis set). Figure 7.1 plots the singly occupied natural orbital of $C_6F_6^{-1}$ from the EOM-MP2 calculations, both at the planar geometry of the neutral as well as at the optimized geometry of the non-planar anion. From this figure it is seen that the anion is far more diffuse in the planar structure. Even though C_6F_6 is not spherical, it is instructive to plot $r^2\phi_{nat}^2$ for the planar and buckled forms of the anion (see Figure 7.2). This representation makes clearer the highly diffuse nature of the singly occupied natural orbital (NO) for the planar structure. These results are consistent with the anion being nonvalence for the planar structure and valence for the buckled structure. Although the buckled valence anion is generally referred to as σ^*, it is clear from Figure 7.1 that it involves significant σ^*/π^* mixing.
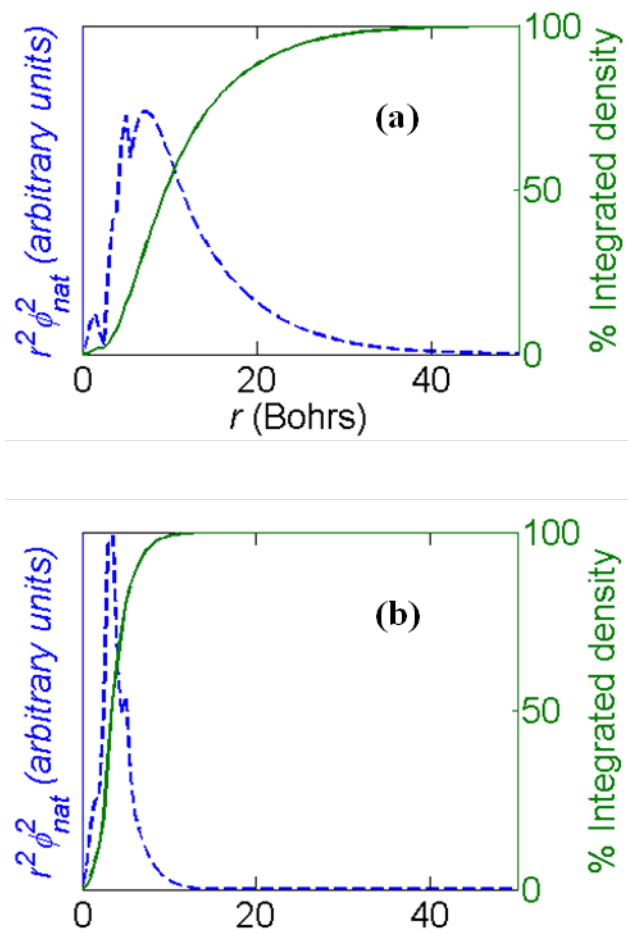
Figure 7.2: Radial distribution and integrated density of the singly-occupied natural orbital of $C_6F_6^-$ from EOM-MP2 calculations. Results are shown for the (a) planar correlation-bound and (b) buckled valence-bound forms of the anion.
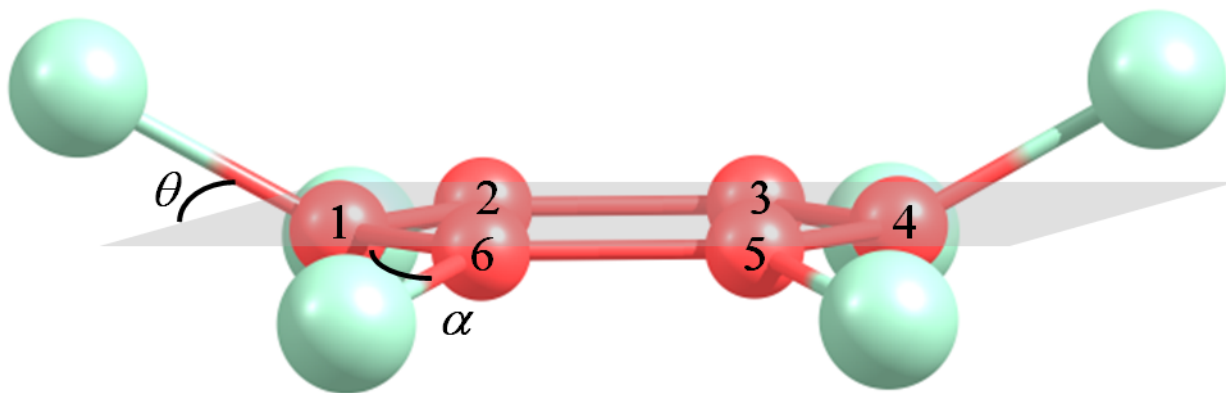
Figure 7.3: Definitions of the key angles defining the buckling coordinate of $C_6F_6^-$ used in calculating the potential energy curve for buckling of the anion. For the minimum energy structure $\theta = 20.0°$ and $\alpha = 8.0°$.

Analysis of the EOM wavefunction of the correlation-bound anion shows that the dominant configurations (coefficients 0.1-0.8) are those with the unpaired electron occupying various Hartree-Fock virtual orbitals of a_{1g} symmetry. These configurations generate the proper linear combination of a_{1g} virtual orbitals needed to describe the singly-occupied natural orbital in the dominant configuration represented in terms of natural orbitals. There are also several configurations with coefficients on the order of 0.01-0.02 in which the excess electron is excited from the diffuse s-like orbital into very diffuse p-like orbitals, while simultaneously one of the valence electrons of C_6F_6 is also electronically excited. These excited configurations describe dispersion interactions between the excess electron and the valence electrons of C_6F_6, which are essential for the binding of the excess electron.

As shown in Figure 3.3, two angles undergo appreciable change as the anion buckles. These are θ, involving the fluorine atoms attached to C1 and C4 and which has the value of about 20° in the optimized structure, and α, involving the fluorine atoms attached to C2, C3, C5, C6, and which has a value of about 10° in the optimized structure.

Figure 4.4 plots the anion and neutral potential energy curves as a function of the buckling coordinates. The θ and α values used in generating this potential were obtained by linear interpolation between their values for the planar molecule and for the optimized buckled form of the anion. The energy of the neutral was also computed along the buckling

73

pathway. Significantly, as the anion buckles it evolves into the non-planar valence-bound anion without a barrier. The energy of the anion is stabilized by 0.30 eV in going from the planar structure of the neutral molecule to the optimized buckled structure of the anion. Of this, 0.13 eV of the stabilization results from the relaxation of the planar geometry of the neutral molecule to the planar geometry of the anion.

The resulting potential energy curve can be viewed as arising from an avoided crossing between nonvalence correlation-bound and valence-bound anion states. To put this on more concrete footing we have also carried out EOM-MP2 calculations of the lowest EA of C_6F_6 with the cc-pVDZ basis set. Due to the absence of diffuse basis functions, these calculations, when combined with the MP2 energy of the neutral molecule, provide an estimate of the energy of the valence-type anion state in a diabatic picture. In plotting the diabatic potentials in Figure 7.4, we have assumed that the anion is purely valence-like at a buckling angle of 20° and purely correlation-bound for the planar structure. We have also assumed that in the diabatic picture the EBE of the correlation-bound anion is essentially independent of the buckling angle. The resulting diabatic curves cross at a buckling angle of about 7° at which the off-diagonal coupling between the diabatic states is about 0.25 eV. The diabatic potential for the valence-bound anion crosses the neutral potential at a θ value near 4°. For θ angles less than 4°, this state would be subject to electron detachment. However in the present calculations auto-ionization is suppressed by the use of a basis set lacking diffuse functions.

It is of interest to contrast C_6F_6 with benzene. Benzene and C_6F_6 have approximately the same polarizability, and, as a result, the main difference in the electron-molecule interaction potentials of these two molecules is in the electrostatic contribution. Figure 7.5 displays the ab initio electrostatic and polarization potentials calculated at the MP2/aug-cc-pVDZ level for a point negative charge approaching C_6F_6 along the C_6 axis perpendicular to the plane of the molecule. The computations for electrostatic and polarization potentials were carried out using a negative point charge. First the total potential was calculated in the presence of the point charge. The electrostatic potential was then calculated and subtracted from the total potential to obtain the polarization potential. As seen from Figure 7.5, both the electrostatic and polarization interactions are sizeable and attractive for C_6F_6, being of the order of 0.5 eV at a distance of 5 Bohrs from the ring. In contrast, the electrostatic inter-

74
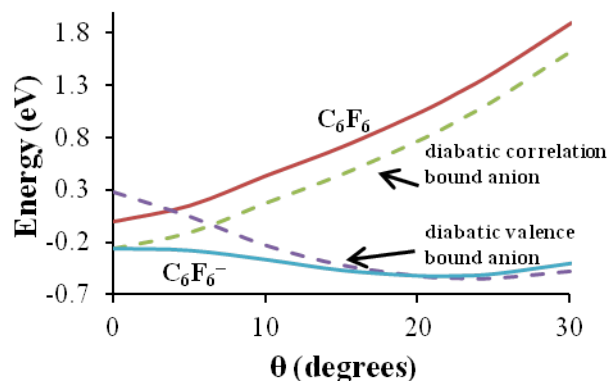
Figure 7.4: Potential energy curves of $C_6F_6^-$ and C_6F_6 along the buckling coordinate leading to the C_{2v} minimum of the anion. The θ and α angles were generated by a linear interpolation between their values in the the planar structure and their values in the C_{2v} potential energy minimum of the anion. For the specified values of these angles all other degrees of freedom were optimized using the EOM-MP2 method with the aug-cc-pVDZ+$7s7p$ basis, followed by single-point calculations using the aug-cc-pVTZ+$7s7p$ basis set. The diabatic potential for the valence anion was obtained from EOM-MP2 calculations using cc-pVDZ basis set with the energies being shifted so that at $\theta=20°$ the resulting energy of the anion matches that obtained from the EOM-MP2/aug-cc-pVTZ+$7s7p$ calculations.

Figure 7.5: Polarization and electrostatic potentials for a point negative charge interacting with C_6F_6. The point charge is located along the C_6 axis, and the distance is measured from the center of the ring. The potentials were calculated at the MP2/aug-cc-pVDZ level.

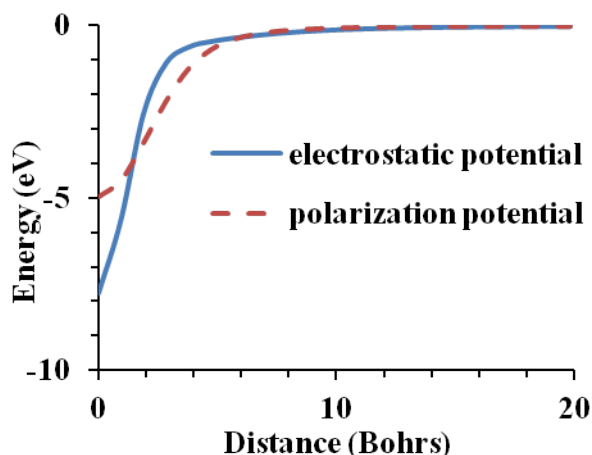action between a point negative charge on the C_6 axis with benzene is repulsive for distances greater than about 2 Bohrs from the center of the ring. The difference in the electrostatic potential for C_6F_6 and benzene is due to the carbon atoms being positively charged in the former and negatively charged in the latter. For benzene EOM-MP2 calculations do not give a correlation-bound anion. Thus, even though correlation effects are crucial for binding the excess electron to the planar C_6F_6 molecule, the favorable electrostatic potential in the vicinity of the carbon atoms is also important.

We have also carried out EOM-MP2 calculations on the coplanar perfluorobenzene dimer extracting the energies of the two lowest anion states. These calculations were motivated by the STM measurements of Dougherty et al. of C_6F_6 on Cu(111).[120] The relative orientation of the monomers is chosen to correspond closely to that of the monomers on Cu(111) at monolayer coverage and is depicted in Figure 7.6. (The geometry of each monomer is constrained to that optimized for the neutral.) Figure 7.6 also reports, as a function of the intermonomer separation, the EBEs of the two states as calculated using the EOM-MP2 method with the aug-cc-pVDZ+7s7p basis set. As expected, the dimer possesses two low-energy anion states, that can be viewed as arising from the plus ("bonding") and minus ("antibonding") combinations of the monomer-localized natural orbitals associated
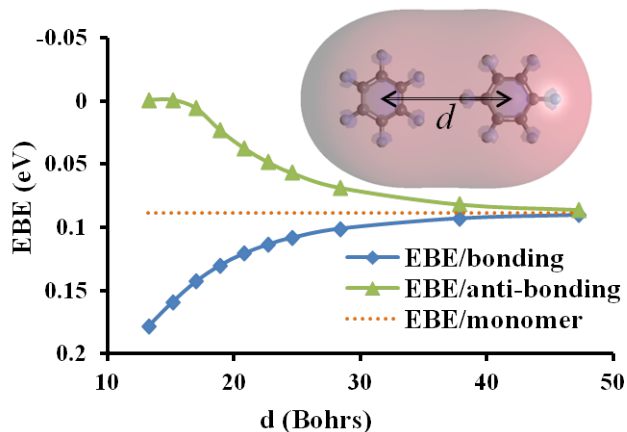
Figure 7.6: EBEs of the C_6F_6 dimer as a function of the intermolecular distance, d and plot of the singly occupied natural orbital. The EBEs were obtained from EOM-MP2 calculations using the aug-cc-pVDZ $+7s7p$ basis set on each monomer. The inset displays the singly occupied natural orbital of the ground state of $(C_6F_6)_2^-$ $(d = 15$ Bohrs) using the surface enclosing 70% of the density calculated using the EOM-MP2 method.

with the correlation-bound anions. Most strikingly, the lowest anion state is appreciably stabilized (relative to that of the monomer) even for monomer separations as large as 30 Bohrs. This is a consequence of the highly extended nature of the wavefunction of the correlation-bound anion (see Figure 7.2). The singly-occupied natural orbital of the lowest anion state of the dimer is shown in Figure 7.6, from which it is seen that the natural orbital encompasses both monomers. The antibonding state ceases to be stable (i.e., collapses onto the neutral plus a free electron) for monomer separations less than 17 Bohrs. We note that both anion states would be stabilized by about 0.045 eV were the calculations carried out in the more flexible aug-cc-pVTZ+$7s7p$ basis. At the equilibrium geometry of the C_6F_6 dimer, the ground state anion of the dimer is stabilized by 0.07 eV compared to the anion of the monomer. Based on our results for the dimer, we expect that for a two-dimensional array of C_6F_6 molecules (arranged as in monolayer coverage on the Cu(111) surface) the band associated with the correlation-bound anion would have a width of 0.8 eV, which is of the same magnitude as the band-width (1.25 eV) of the relevant feature in the two-photon photoemission experiments.[147] In contrast, exploratory calculations on

σ^* and π^* valence anion states of C_6F_6 dimer (using basis sets that avoid collapse onto the continuum), give splitting between the bonding and antibonding combinations of the monomer orbitals that are about an order of magnitude smaller than for the correlation-bound anion, providing support to our proposal that the correlation-bound C_6F_6 anion is responsible for the resonant process seen in the STM and two-photon photoemission experiments of C_6F_6 on Cu(111).

7.4   CONCLUSIONS

In this study we have demonstrated that, in its planar equilibrium structure, C_6F_6 possesses a diffuse nonvalence correlation-bound anion state lying energetically about 0.135 eV below the neutral molecule. This species evolves without a barrier into the valence-bound anion as the molecule buckles. Our calculations suggest that the large s-wave cross section for scattering of low-energy electrons from C_6F_6 is a result of the correlation-bound anion rather than to a virtual state. We also carried out calculations on the low-lying anion states of the C_6F_6 dimer and find that when the separation corresponds to that between molecules on the Cu(110) surface at monolayer coverage, there is a sizeable energy splitting between the bonding and antibonding correlation-bound anion states. These results suggest that the extended anion state of C_6F_6 on Cu(111) observed in two-photon photoemission and in STM measurements may correspond to the correlation-bound anion characterized in the present study rather than to a valence σ^* anion. A correlation-bound anion, delocalized over several C_6F_6 molecules may be the entity responsible for the high electron mobility in liquid C_6F_6.

8.0   NONVALENCE CORRELATION-BOUND ANION STATES OF PLANAR POLYCYCLIC AROMATIC SYSTEMS

Nonvalence correlation-bound anions have been identified for a wide range of species including $(Xe)_n$ clusters,[12] C_{60},[13] C_6F_6,[14] and certain $(NaCl)_n$[11] and $(H_2O)_n$ clusters.[15] By definition, for nonvalence correlation-bound anions the excess electron is unbound in the Hartree-Fock approximation, and upon inclusion of long-range dispersion correlation effects it becomes bound in a diffuse nonvalence orbital. In describing correlation-bound anions theoretically it is necessary to employ a method that allows for orbital relaxation in response to correlation effects. Two such methods are the equation-of-motion coupled cluster method[5,9,10] and the algebraic diagrammatic Green's function methods.[4] Nonvalence correlation-bound anion states of molecules and clusters are closely related to image-potential states of metal surfaces. Graphene and also graphene flakes are known to possess image potential states.[122] This naturally leads to the question of the minimum size acene that can support a nonvalence correlation-bound anion state. In particular, given the existence of a correlation-bound anion of C_{60} one might expect that acenes of comparable size might support such diffuse anions states. In ref 122 the smallest grapahene flake found to have an image potential state was about 300 fused rings in diameter, much larger than we would have expected based on the C_{60} result. In this work, we use the EOM-MP2 method to explore the possible existence of correlation-bound anion states of acenes with seven to nineteen rings.

A major challenge in using ab initio methods for describing correlation-bound anions of large molecules is the adoption of a sufficiently flexible basis while avoiding linear dependency problems. In this work we employ the ANODZ[18] basis set augmented with a $1s1p$ set of diffuse Gaussian functions on each hydrogen atom and a $6s6p$ set of diffuse primitive Gaussian type orbitals on each side of the acene. The latter diffuse sets are centered 6.0 Å

from the central ring and contained exponents ranging from 0.005000 to 0.000884.

The acenes examined include coronene, hexabenzocoronene, circumcoronene, the stacked coronene dimer with a 3.7 Å intermolecular separation, and linear acenes with three to eleven fused rings. The calculations do not give a correlation-bound anion state of coronene or the linear acenes smaller than undecacene, but do give a correlation-bound anion state of the other species considered. In the correlation-bound anion states, the excess electron is predominantly localized around the edges rather than above and below the plane of the molecule. This result is a consequence of an attractive electrostatic interaction between the excess electron and the H atoms of the acene and an unfavorable electrostatic interaction with the peripheral carbon atoms of the acenes. It is important to note that the electrostatic interactions, in the absence of correlation effects, are inadequate for binding the excess electron.
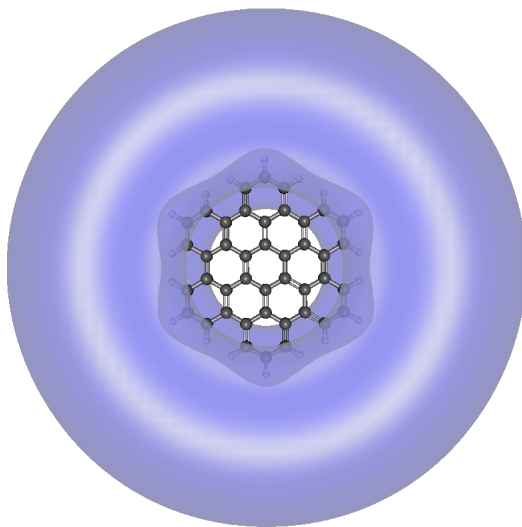
Figure 8.1: Correlation-bound anion state of hexabenzocoronene

Although coronene does not support a nonvalence correlation-bound anion, perfluoro-coronene does, with an EBE of 257 meV. In this case the excess the excess electron is localized above and below the plane of the molecule. Here, the positively charged carbon atoms around the perimeter play an important role in the binding of the excess electron. Replacing the CH groups of coronene with N atoms also results in a stable correlation-bound anion with an EBE of 387 meV. As for the fluorine derivative the excess electron is localized above and below the plane of the ring.
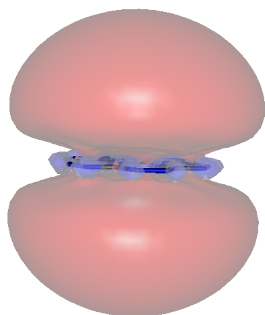
Figure 8.2: Correlation-bound anion state of nitrogenated coronene.

The EBE of the nonvalence correlation-bound anion of the coplanar coronene dimer is 38 meV. The smallest linear acene that has nonvalence correlation-bound anion at the EOM-MP2 level of theory is undecacene with an EBE of only 7 meV. Again, much of the charge distribution of the excess electron is localized around the periphery of the ring system.
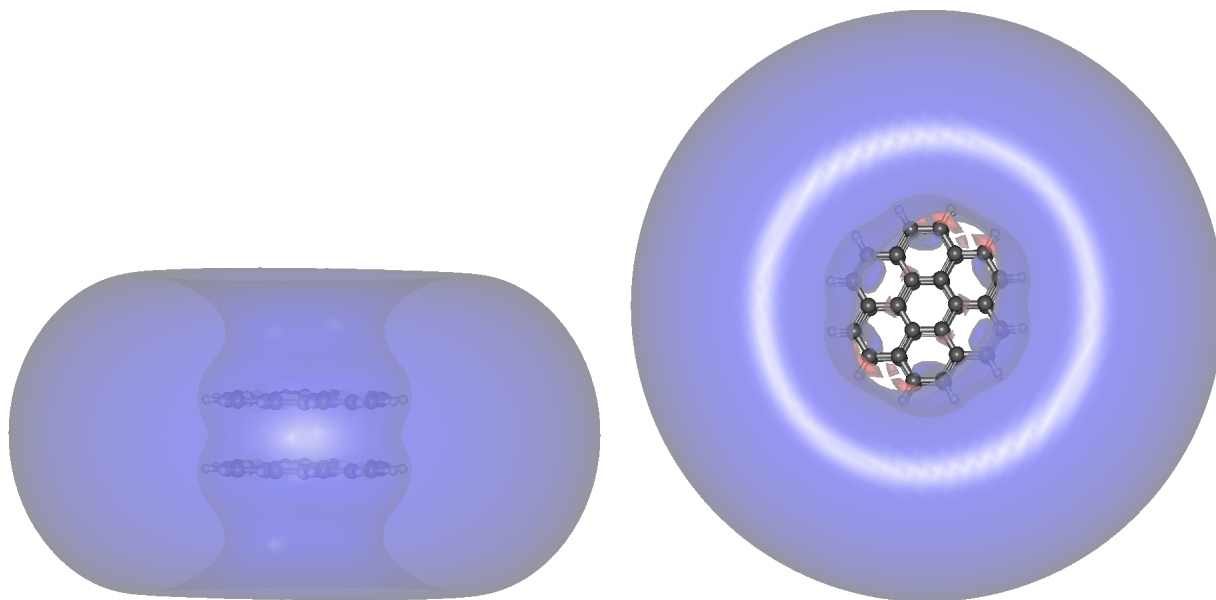
Figure 8.3: Correlation-bound anion state of coronene dimer: a) side view and b) top view.
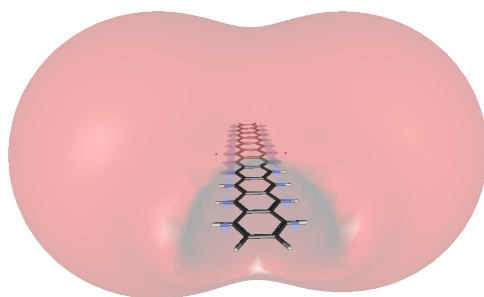
Figure 8.4: Correlation-bound anion state of undecacene.

These studies indicate that for sufficiently large molecules or clusters of polycyclic aromatic systems, nonvalence correlation-bound anion states are an essential feature. In particular, acenes as small as hexabenzocoronene with 13 fused rings and undecacene with 11 fused rings, are predicted to have correlation-bound anions. These are much smaller than graphene flakes that have been observed. For the unsubstituted acenes, the excess electron is localized around the periphery of due to the electrostatic interaction with the positively charged H atoms. With suitable substitution, one can shift the charge distribution of the excess electron so that it is localized above and below the plane of the ring. The results of this study will serve as valuable benchmarks for developing model potentials that can be used to treat larger systems, where ab initio calculations would be intractable.

9.0 SUMMARY

A class of anionic states that can be described as nonvalence correlation-bound is explored in this thesis. The excess electron in a nonvalence correlation-bound state is mostly located beyond the van der Waals region of the molecule. Correlation effects are essential to bind the excess electron in such anionic states. The Hartree-Fock method fails to bind the excess electron in these anionic states. Using a model $(H_2O)_4$ cluster and a CO_2 molecule it was shown that Hartree-Fock orbital based methods such as ΔSCF, MP2, and CCSD(T) fail to bind the excess electron when it is correlation-bound. Only methods such as EOM-CCSD, EOM-MP2, ADC(2), OMP2, and BCCD(T) that incorporate orbital relaxation with respect to correlation effects can describe the binding of excess electron in nonvalence correlation-bound states.

Using EOM-CCSD, EOM-MP2 and ADC(2) methods, benchmark ab initio EBEs were computed out for large-water clusters. The three methods gave similar electron binding energies suggesting that the computationally cheaper ADC(2) method could be employed in calculations of larger water clusters. The agreement also showed that orbital relaxation with respect to second-order correlation effects is sufficient for the description of electron binding to water clusters. While ab initio calculations provided the much needed insight into the nature of correlation and relaxation effects for electron binding in water clusters, such ab initio computations were still prohibitive for large clusters with hundreds of molecules. One-electron model Hamiltonians are a computationally cheaper alternative. A new one-electron self-consistent polarization-based model Hamiltonian was developed and was shown to give good agreement with ab initio studies. The self-consistent treatment of polarization potential was shown to be especially important for interior solvated clusters.

EOM methods were then used to investigate an s-type nonvalence correlation-bound state of C_{60}^-. Experiments have been inconclusive on the existence of this state. Using

EOM-CCSD methods it was established that C_{60} binds the excess electron by about 120 meV. The excess electron in the s-type state was shown to have only 9% of the charge localized inside the C_{60} cage and the remaining 91% was localized outside. Encapsulation of molecules such as He, Ne and H_2O was shown to decrease the electron binding energy of the s-type state due to an excluded volume effect. Based on the ab initio electron binding energy and potentials, a one-electron model-potential was then developed to investigate nonvalence correlation-bound states of spherical fullerenes. The model potential included both charge-flow and dipole polarizations. The model potential was used to demonstrate the existence of multiple nonvalence correlation-bound anion states for large fullerenes and, hybridization of nonvalence correlation-bound states.

A nonvalence correlation-bound anion state was established for C_6F_6. This state was shown to evolve into the valence-bound anion state upon buckling of the the ring. This study showed that nonvalence correlation-bound states can act as doorways for the formation of more stable valence-anionic states. Ab initio methods were also used to establish nonvalence correlation-bound states of large planar acenes. The excess electron in these states was shown to be located along the edges rather than above and below the planes of these acenes. The nonvalence correlation-bound states for large fullerenes and acenes are an important finding as they are finite size analogues of image-potential states of metallic surfaces.

These studies indicate that nonvalence correlation-bound states can be found for a variety of molecules. In almost all cases studied here, these states were either previously unknown, controversial or even overlooked. Using methods that do not depend on Hartree-Fock reference enabled the identification of nonvalence correlation-bound states in the current studies. I hope that these studies could guide future investigations and applications of the correlation-bound anion states.

APPENDIX A

A BOTTOM-UP VIEW OF WATER NETWORK-MEDIATED CO$_2$ REDUCTION USING CRYOGENIC CLUSTER ION SPECTROSCOPY AND DIRECT DYNAMICS SIMULATIONS

A.1   ABSTRACT

The transition states of a chemical reaction in solution are generally accessed through exchange of thermal energy between the solvent and the reactants. As such, an ensemble of reacting systems approaches the transition state configuration of reactant and surrounding solvent in an incoherent manner that does not lend itself to direct experimental observation. Here we describe how gas-phase cluster chemistry can provide a detailed picture of the microscopic mechanics at play when a network of six water molecules mediates the trapping of a highly reactive hydrated electron onto a neutral CO$_2$ molecule to form a radical anion. The exothermic reaction is triggered from a metastable intermediate by selective excitation of either the reactant CO$_2$ or the water network, which is evidenced by the evaporative decomposition of the product cluster. Ab initio molecular dynamics simulations of ener-

---

gized $CO_2 \cdot (H_2O)_6^-$ clusters are used to elucidate the nature of the network deformations that mediate intracluster electron capture, thus revealing the detailed solvent fluctuations implicit in the Marcus theory for electron transfer kinetics in solution.

A.2 INTRODUCTION

Gas phase cluster chemistry is playing an increasingly important role in clarifying the molecular-level speciation of ubiquitous aqueous ions such as the hydrated proton[148–151] as well as more elusive transients such as the hydrated electron.[28,152–160] The primary focus of most spectroscopic efforts has been the characterization of isomers[161–163] that can, in favorable cases, yield detailed pictures of the interdependent deformations of solute and solvent.[162] An emerging frontier in this endeavor involves leveraging the knowledge of the stationary points on the potential energy surface, gained by isomer-selective spectroscopies[164,165] and electronic structure calculations,[159,166–169] to elucidate the dynamics of aqueous reactions in a regime where the role of the water network can be explored with explicit molecular detail. In this article, we describe how recent developments in cryogenic ion chemistry[162,170] allow us to trap reactants in a metastable condition with size-selected clusters and to photo-initiate a reaction through vibrationally mode-selective excitation of either the reactant or the solvent constituents. The level of theory required to address this chemistry is established through analysis of the vibrational spectra of the metastable complex. Molecular dynamics simulations are then employed to reveal the cooperative interactions that underlie a water network-mediated chemical transformation.

We focus here on the cluster variation of the aqueous process in which CO_2 is reduced to the CO_2^- radical anion by scavenging a hydrated electron (e_{aq}^-).[171] This reaction has been well characterized in the context of aqueous radiation chemistry, where the reduction of CO_2 proceeds with diffusion-controlled kinetics.[171–173] The microscopic analogues of e_{aq}^-, $(H_2O)_n^-$, have been extensively studied over the past twenty years,[24,38,63,70,155,156,160,164,174–179] and there is a consensus that, in the small cluster ($n < 20$ or so) regime, the species that are synthetically accessible accommodate the excess electron in a diffuse orbital located on the outside of the H-bonded water network.[63,69,152,153,160,167,180] For a given size, there are

variations in the observed electron binding energies because a cluster can exist in several isomeric forms (i.e., with different network morphologies),[25,177,181,182] and here we are primarily concerned with the class that displays the highest electron binding energy (denoted type I).[63,160,174] At small sizes ($n \leq 20$), the type I clusters exhibit preferential electron attachment to a water molecule held to the network by a double H-bond acceptor (AA) motif.[28,152,159] Figure A.1 presents the structure and the vibrational spectrum of the hexamer anion most relevant to this work, highlighting the fact that the bands associated with the AA water molecule dominate the IR spectrum in OH stretching region. In addition, the HOH intramolecular bending vibration of the AA molecule (ν_{AA}) is uniquely red-shifted compared to those of all other network sites.[152]

A.3 RESULTS AND DISCUSSION

A.3.1 Reaction Exothermicity and Potential Energy Landscape

The traditional way to carry out an electron scavenging reaction in the cluster regime involves collisions between anionic water clusters and an acceptor molecule, in our case, carbon dioxide:[171]

$$CO_2 + (H_2O)_n^- \rightarrow CO_2^- \cdot (H_2O)_{n-m} + mH_2O \tag{A.1}$$
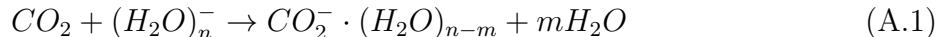
This is an evaporative charge-transfer process, where the reaction exothermicity is released by ejection of m solvent (water) molecules. The reaction exothemicity is actually cluster size dependent as evidenced by the m dependence on n, such that m increases from 1 for n = 6 to 3 for n = 15.[183]

There are two important contributions to the overall energetics: one from the difference in thermodynamic or adiabatic electron affinities (AEA) of $(H_2O)_n$ and CO_2, and the other from the hydration energy of the product CO_2^- ion. Interestingly, the AEA of CO_2 is negative ($\sim$-0.6 eV), which means that the isolated anion is unstable relative to the neutral molecule and a free electron.[184] The electron ejection process is quite slow, however, because of the poor vibrational (i.e., Franck-Condon) overlap between the zero-point vibrational level of bent CO_2^- and the vibrational levels of linear CO_2. To access configurations with
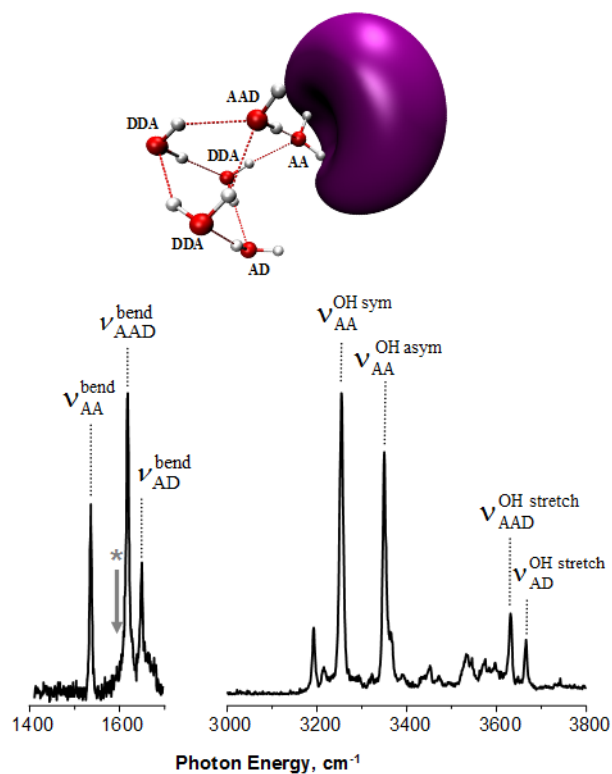
Figure A1: Structure and Ar-tagged vibrational spectrum of the type I water hexamer anion, $(H_2O)_6^-$. The excess electron preferentially binds a single water molecule with both of its protons directed into the excess electron cloud in a double H-bond acceptor (AA) binding motif. The HOH bending fundamental (ν_{AA}^{bend} bend) associated with the AA binding site is uniquely red-shifted relative to that in an isolated water monomer, highlighted with a starred arrow.

significant vibrational overlap, the system must have sufficient excess energy to reach the crossing seam between the CO_2^- and CO_2 potential energy surfaces. Effectively, this means that there is a barrier to formation of the CO_2^- anion in isolation. If a barrier is retained in the cluster, it would enable capture of the CO_2 molecule by the negatively charged water cluster without spontaneous transfer of the excess electron.

Upon intracluster electron transfer in reaction A.1, the more compact CO_2^- ion is very efficiently hydrated compared to the diffuse electron. (In aqueous solutions, for example, the hydration enthalpy of the excess electron is only 40% that of the radical anion.)[171,185,186] As a result, geometrically relaxed $CO_2^- \cdot (H_2O)_j$ cluster anions are stable relative to electron loss even at small sizes. The enhanced hydration energy of the valence anion relative to the diffuse electron of $(H_2O)_6^-$ results in a lower bound for the overall exothermicity of about 0.5 eV for reaction A.1 at $n = 6$. This value was deduced from the observation that the bimolecular reaction occurs with loss of $\sim$1.1 water molecules for $n = 6$.[185,187–190] We note that the $(H_2O)_6^- \cdot Ar_k$ cluster retains less internal energy prior to the collision than the $CO_2^- \cdot (H_2O)_j$ product due to the much lower binding energy of Ar (500 cm^{-1}) relative to that of a water molecule ($\sim$3400 cm^{-1}).[153] This effect is included in the experimental observation leading to the determination of the reaction exothermicity at $n = 6$.

Significant features in the overall potential energy landscape controlling this reaction are indicated in a qualitative manner in Figure A.2. (For simplicity, the Ar atom has not been included.) Our goal is to trap the reactive intermediate in the shallow well (denoted R) corresponding to attachment of a neutral CO_2 molecule to the anionic water cluster that retains the excess electron in a diffuse orbital. We then structurally characterize this entrance channel complex before inducing the reaction by selective vibrational excitation of various modes in the reactant complex:

$$CO_2^- \cdot (H_2O)_6^- \cdot Ar + h\nu \rightarrow [CO_2 \cdot (H_2O)_6]^- \cdot Ar$$

$$\rightarrow [CO_2 \cdot (H_2O)_6]^- + Ar \rightarrow CO_2 \cdot (H_2O)_j^- + (6-j)H_2O + Ar. \quad \text{(A.2)}$$
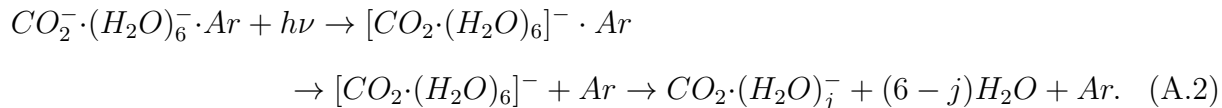
The formation of the $CO_2^- \cdot (H_2O)_j$ product isomer (denoted P in Figure A2) is accompanied by the release of the reaction exothermicity through evaporation of Ar as well as of one or more water molecules. (It is anticipated that the Ar atom evaporates prior to the electron transfer step, as discussed further in section A.2.6.) To aid in the interpretation of the

experimental results, electronic structure calculations have been carried out to elucidate the structures of the R $CO_2 \cdot (H_2O)_6^-$ reactant and P $CO_2^- \cdot (H_2O)_j$ product complexes. In addition, ab initio molecular dynamics (AIMD) simulations have been performed to provide a microscopic picture of how a thermally activated water network deforms to promote the $R \rightarrow P$ interconversion.

A.3.2 Ar Mediated Synthesis of the Entrance Channel Reaction Intermediate

To synthesize the R isomer, we exploit the recent observation by Motegi et al.[191] that the key reactive intermediate in the analogous reaction of $(H_2O)_6^-$ with nitromethane, CH_3NO_2, can be trapped prior to exothermic formation of the $CH_3NO_2^-$ radical anion by using Ar-cluster-mediated condensation:

$$CH_3NO_2^- + (H_2O)_n^- \cdot Ar_q \rightarrow CH_3NO_2 \cdot (H_2O)_n^- + qAr \tag{A.3}$$

carried out in a supersonic free jet ion source.[153,163] Basically, the rapid evaporation of the Ar atoms quenches the system into the metastable minimum corresponding to R. In the present application of the method, water cluster anions with multiple argon atoms attached were first created in a supersonic expansion (Ar seeded with a trace amount of water vapor) through a pulsed valve (Parker-Hannifin, 10-Hz repetition rate, 0.5 mm-nozzle), and ionized with a counterpropagating 1 keV electron beam. To generate the R isomer, carbon dioxide vapor was then introduced into the main chamber through a second pulsed value located about 12 cm from the supersonic nozzle. This procedure creates a background gas that is entrained into the supersonic flow where it undergoes reactive collisions with cluster ions formed earlier in the expansion.[192] Figure A3 presents mass spectra of the cluster distributions illustrating the preparation of the reactant, water-based anions (upper trace) and formation of products after entrainment of CO_2 vapor into the expansion (lower trace). The peaks highlighted in blue correspond to the carbon dioxide-water distribution $[CO_2 \cdot H_2O)_n]^-$ (where the progression shown starts at $n = 4$ and peaks at $n = 5$). A peculiarity of the water anion distribution is that it begins promptly at $n = 6$, and the maximum in the $[CO_2 \cdot H_2O)_n]^-$ products at $n = 5$ results from the exothermicity of the reaction of $(H_2O)_n^-$ with CO_2 followed by loss of a water molecule. The first Argon-tagged species in
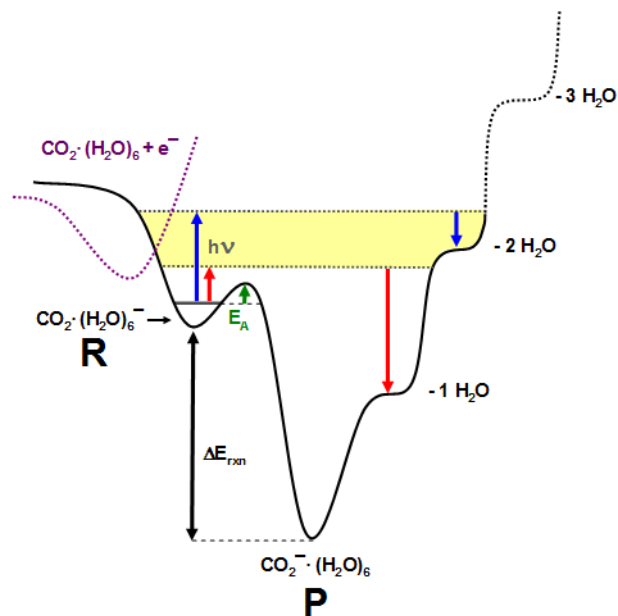
Figure A2: Potential energy landscape illustrating the anionic and neutral species involved in the carbon dioxide-water system. Two forms of the $[CO_2 \cdot (H_2O)_6]^-$ anion exist: one where the excess electron resides in a valence orbital (the radical anion of carbon dioxide), denoted P, and another, denoted R, where the excess electron is retained in a diuse electron cloud. Excitation of the high energy isomer induces the loss of one or two H_2O molecules due to the exothermicity, δE_{rxn}, of the intracluster electron capture reaction. The activation energy for the intracluster reaction, EA, is shown with a green arrow. The purple dotted line shows the neutral surface of the complex.

the $[CO_2 \cdot H_2O)_6]^-$ progression is highlighted with the red dotted line, and is the main target in the present study.

A.3.3 Determination of Isomer Distribution using Electron Photodetachment

It is expected that both R and P isomers of $[CO_2 \cdot H_2O)_6]^- \cdot Ar$ might be prepared with this synthetic scheme. The two isomers can be readily differentiated, however, due to the large difference in their electron binding energies, which can be measured using photoelectron spectroscopy. It is important to consider both the vertical electron detachment energy (VDE), which describes the energy required to remove the electron when the structure is frozen at the equilibrium geometry of the anion, and the adiabatic electron affinity (AEA) describing the minimum energy required to remove an electron in a situation where the neutral cluster relaxes to its equilibrium geometry. In most cases, only the VDE is directly observed in photoelectron spectroscopy because the vibrational overlap between the $v = 0$ levels of the anion and neutral is often negligibly small (as is the case here). The VDE of the highest binding, type I form of $(H_2O)_6^-$ is 0.48 eV,[182] while the AEA is on the order of 0.12 eV.[174] The difference between the VDE and AEA is the reorganization energy (RE), which reflects the extensive change in geometry that occurs when the water network accommodates an excess electron.[193] The large RE value is key to our approach because most vibrational fundamentals occur below the cluster VDE, but above its AEA. As a result, vibrationally-mediated electron ejection from the bare $(H_2O)_6^-$ cluster occurs in a two-step process (denoted autodetachment) in which vibrational energy in a specific mode is first degraded into thermal excitation before finally emitting slow electrons through a statistical mechanism, akin to evaporation, called thermionic emission.[174,193,194] This provides an opportunity to trap the excess electron if an electron scavenger is present in the vibrationally excited cluster. The VDEs of the R and P isomers are quite different (0.5 and 3.0 eV, respectively),[195,196] and we therefore measured the photoelectron spectrum of the $[CO_2 \cdot H_2O)_6]^- \cdot Ar$ ions created by Ar-mediated condensation of CO2. This was carried out with the velocity map imaging method,[197–199] and Figure A4 compares the photoelectron spectrum from $[CO_2 \cdot H_2O)_6]^- \cdot Ar$ with that of $(H_2O)_6^- \cdot Ar$ as well as that reported earlier for the isomer P form of $CO_2^- \cdot (H_2O)6$.[183] Note that the observed VDE for $[CO_2 \cdot (H_2O)_6 \cdot Ar]^-$ occurs quite close to that of the bare hexamer anion and occurs with the same skewed
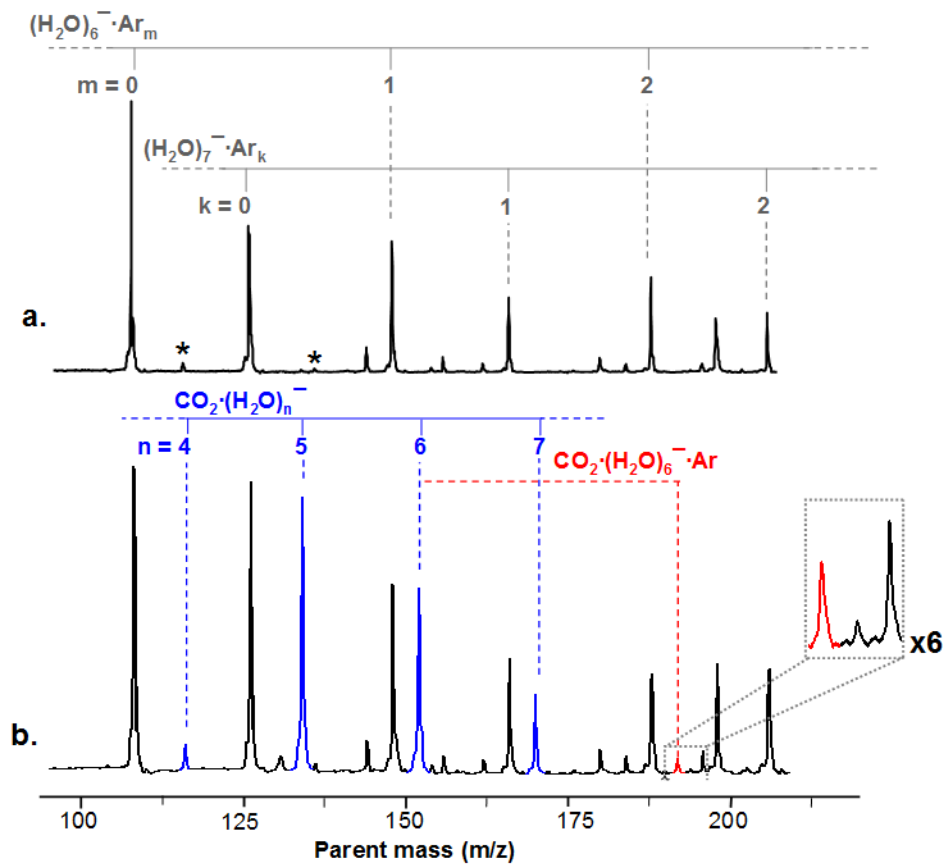
Figure A3: Mass spectra of (a) the $(H_2O)_n^-$ reactant ions in the $CO_2 + (H_2O)_n^-$ reaction and (b) the $[CO_2 \cdot (H_2O)_n]^-$ product ions. Peaks highlighted with the dotted blue lines correspond to the carbon dioxide-water distribution $[CO_2 \cdot (H_2O)_n]^-$. The dotted red line highlights the $[CO_2 \cdot (H_2O)_n]^- \cdot Ar$ parent ion of interest in this study. Peaks highlighted with (*) in the top trace represent mass packets from the Argon-tagged water dimer progression, $(H_2O)_2^- \cdot Ar_n$

angular distribution characteristic for ejection of the electron to a p-like continuum orbital, as expected for the entrance channel R isomer. Since the 2.33 eV photon energy used to obtain the image in Figure A4 is far below the VDE of the P isomer ($\sim$3.0 eV), that species is not observed in the present experiment. Nevertheless, we can still quantify how much of the ion yield is in the P isomer form by monitoring the degree to which the ion beam can be photodepleted upon excitation above the VDE of R (and hence in the region of continuum absorption due to direct electron photodetachment), but well below that of P. Excitation at 4400 cm^{-1} provides a particularly useful probe, as it efficiently photodetaches R, but is not resonant with any strong vibrational transitions associated with P. While less than 5% of the bare (non-Ar tagged) $[CO_2 \cdot (H_2O)_6]^-$ peak was destroyed at this energy, over 90% of the Ar-tagged species was photodepleted, thus establishing that the Ar-mediated condensation scheme provides a highly efficient and selective synthetic route to the R isomer. From this observation, we infer that the barrier to reaction must lie above the argon binding energy $D_0(Ar)$ ($\sim$500 cm^{-1}), otherwise the entrance channel would not survive the Ar evaporation events required to quench the collision complex into the entrance channel minimum during the original creation of the R isomer.

A.3.4 Infrared Photophysics of the Trapped Reaction Intermediate

Having isolated the reactive intermediate (isomer R) using the Ar-mediated approach, we next turn to the characterization of its structure and photophysical behavior. This requires acquisition of the vibrational spectrum of R using an "action" method, where resonances are detected by monitoring decomposition products after vibrationally excited states degrade their energy into the soft modes of the cluster and eventually lead to evaporation of weakly bound constituents.

Mass-selective infrared excitation was carried out using the Yale double-focusing, tandem time-of-flight (TOF) photofragmentation mass spectrometer as described in detail previously.[200] This instrument is capable of measuring the branching between electron photodetachment and break-up of the ion into charged fragments. One important consideration in the goal of phototriggering the intracluster electron capture is that, because the AEA of the anionic water cluster is quite low ($\sim$0.12 eV), vibrational excitation most likely competes with electron photodetachment, even when the cluster is complexed with CO_2.
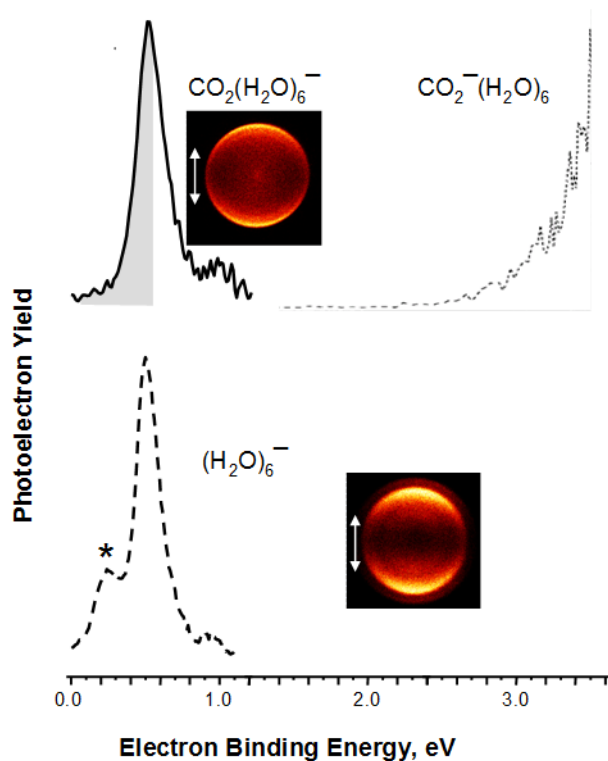
Figure A4: Photoelectron spectra of $[CO_2 \cdot (H_2O)_6]^- \cdot Ar$ (top trace solid line, current study), $[CO_2^- \cdot (H_2O)_6]$ (top trace dotted line, previous study)[183]) and $(H2O)_6^-$, (bottom trace, previous study).18 The raw photoelectron images of the R isomer and the bare water hexamer are displayed in the insets. The peak labeled (*) in the lower trace indicates the band associated with isomer II of water hexamer anion. The shaded gray area highlights the energy range scanned in the vibrational predissociation experiments. The white arrow in the images indicates the direction of the electric field of the laser.

The top trace in Figure A5 presents the fragmentation channel (i.e. giving $CO_2(H_2O)_n^-$ + Ar products) while the lower trace shows the evolution of the electron photodetachment yield as the laser is scanned through the OH stretching region. Note that the vibrational resonances are evident in both spectra, while the electron loss channel exhibits a broad gradual onset as the excitation begins to access the direct electron photodetachment continuum. The latter onset is slow because the direct process is very inefficient near threshold due to the weak vibrational overlap from the ground state geometry of the anion to that of the neutral. The breadth is, in fact, a direct manifestation of the reorganization energy, RE, mentioned above. The high energy cut-off of the scan in Figure A5 is about 420 cm^{-1} below the VDE of R. Interestingly, two resonances (at 3632 and 3662 cm^{-1}) are embedded in the direct detachment continuum region of the photodetachment (PD) spectrum. These features also appear in the predissociation spectrum and are attributed to OH stretching vibrations of the free OH groups associated with the AAD and AD water molecules, respectively.

Lower in energy, the vibrational resonances occur with very little electron loss between the bands, indicative of autodetachment in a regime where the vibrational energy is dissipated into the soft modes of the cluster prior to electron ejection.[174] For example, when water cluster anions in the size range of the hexamer are complexed with an Ar atom (as is the case in the R·Ar target), the Ar binding energy is lower than the AEA so that the system first cools by Ar evaporation before electron loss begins. The $(H_2O)_6^-$·Ar system does not, in fact, yield any ionic fragments as evaporation of a single Ar atom provides insufficient cooling to stabilize the remaining $(H_2O)_6^-$ system relative to thermionic emission. In the case of the R isomer, however, the intra-cluster electron capture process provides an alternative mechanism that retains the charge in the cluster with sufficient binding strength that water loss then becomes the lowest energy dissociation path.

To establish that the fragment ions indeed result from intracluster electron capture, we turn to the distribution of fragment ions, as this encodes the magnitude of energy put into play after photoexcitation. Excitation of the Ar-tagged R isomer at the various resonances throughout the 1300-3800 cm^{-1} region was observed to yield loss of at least one water molecule in addition to the loss of the Ar atom. This is significant because the photon energy corresponding to a low-energy HOH intramolecular bend is not sufficient by itself to

induce evaporation of a water molecule (with a typical binding energy of $\sim$3400 cm^{-1}).[153] It is relevant to note that excitation of the HOH bends of typical Ar-tagged hydrated valence anions results exclusively in loss of the Ar atom. For example, photoexcitation of X$^-$·(H$_2$O)$_n$·Ar (X$^-$ = O$_2^-$, OH$^-$, Cl$^-$) clusters:

$$X^- \cdot (H_2O)_n \cdot Ar + h\nu \rightarrow X^- \cdot (H_2O)_n + Ar \tag{A.4}$$
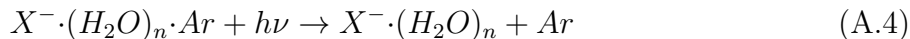
gives only X$^-$·(H$_2$O)$_n$ product ions.[201] The more extensive fragmentation observed upon excitation of R·Ar must therefore be derived from the exothermicity of the intracluster electron capture reaction as indicated in Figure A2. As expected for a statistical dissociation mechanism, the fragmentation pattern gradually evolves from loss of one water molecule (in addition to the Ar atom) to loss of two water molecules in a manner consistent with increasing photon energy as shown in Supplemental Figure 1. This crude form of cluster "calorimetry"[171,180,188,202,203] thus confirms our expectation based on the electron vs. fragment ion branching that the products formed are indeed much more stable than the reactants, which is the necessary result when isomer P is formed upon photoexcitation of R. More interestingly, ejection of the Ar atom alone was never observed at any of the R·Ar resonances, indicating that evaporation of a single Ar atom is not sufficient to quench the system back into the entrance channel minimum. Since the initial cluster retains an internal energy on the order of the Ar binding energy, the observation of reaction upon photoexcitation at 1500 cm^{-1} indicates the barrier to reaction, E$_A$, must be less than $\sim$2000 cm^{-1}. As we noted earlier, this barrier must lie above D$_o$(Ar) so that upon photoexcitation, the more weakly bound Ar atom will be lost first, removing about 500 cm^{-1} from the system.[204] This lowers the upper bound for E$_A$ to about 1500 cm^{-1}.

A.3.5 Structural Characterization of the Entrance Channel Intermediate by Analysis of the Vibrational Band Pattern

Figure A6 presents the vibrational predissociation spectrum of the R isomer over the region of the HOH intramolecular bends and the OH stretches. Included in this range is the asymmetric stretch associated with neutral CO$_2$ at 2349 cm^{-1} (red arrow in Figure A6b).[205] Indeed, there is a strong feature at 2343 cm^{-1}, confirming the identification of the R isomer as consisting of a nominally neutral CO$_2$ moiety attached to the anionic water cluster.
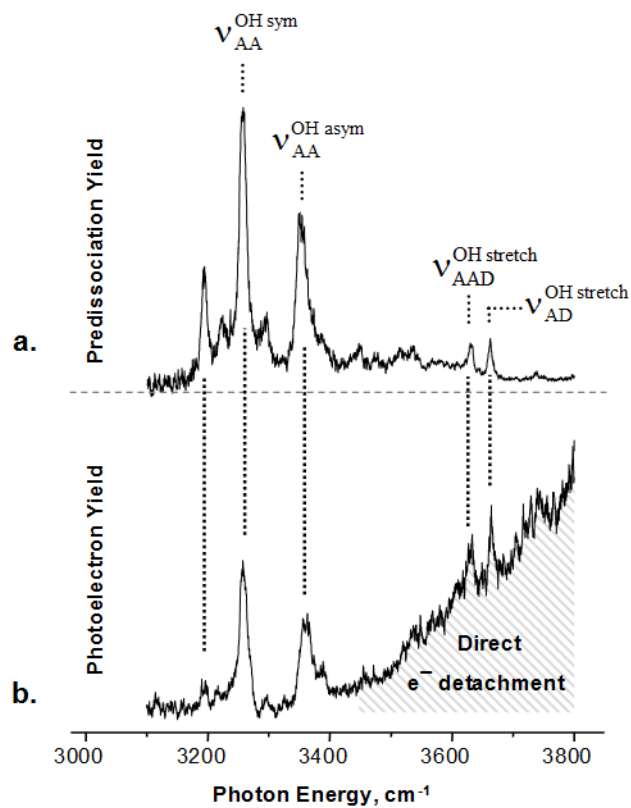
Figure A5: Comparison of (a) the vibrational predissociation spectrum and (b) the electron photodetachment spectrum of $[CO_2 \cdot (H2O)_6]^- \cdot Ar$ in the OH stretching region. The main features in the photodetachment spectrum match the five main OH stretching features in the predissociation spectrum. The onset of the electron detachment continuum is $\sim$3500 cm^{-1}

To obtain a clearer picture of the extent to which the CO_2 molecule perturbs the supporting water network in R, it is useful to consider the band pattern in Figure A6b in the context of the properties associated with the isolated water hexamer anion. The Ar-predissociation spectrum of $(H_2O_6) \cdot Ar_7$ is reproduced at the bottom of Figure A6 (trace c), revealing that the key bands associated with the excess electron binding motif in the bare hexamer anion are remarkably intact in the $CO_2 \cdot (H_2O)_6^-$ spectrum. This observation indicates that the neutral CO_2 molecule resides at a site remote from the excess electron such that it does not significantly perturb its binding to the water cluster.

With these aspects of the structure in mind, we carried out electronic structure calculations to identify cluster geometries that are consistent with the spectroscopic data. The geometry optimizations were carried out using the B3LYP[206,207] density functional method together with the 6-311++G**(sp) basis set.[152,208] A large number of starting structures were considered, and several local minima that have an essentially neutral CO_2 molecule accommodated on the outside of the H-bonded cage-like structure of the type I hexamer anion, were recovered. The lowest energy structure, depicted at the top of Figure A6, features the CO_2 molecule located on the opposite side of the cluster as the diffuse electron cloud. This configuration obviously supports a barrier to CO_2 anion formation since network reorganization and bending of the CO_2 are required for energetically feasible transfer of the excess electron into the valence orbital of the CO_2 molecule. The harmonic vibrational spectra for the lowest energy structure was calculated using the same theoretical method, with the water bending frequencies being scaled by 0.996 and the water stretches and CO_2 CO stretches by 0.970.[152,208]

A.3.6 Site-Specific Activation and the Topology of the Potential Landscape

The presence of a neutral CO_2 moiety in the R isomer provides an excellent opportunity to determine both the importance of the location of the initial energy deposition and the energetic limitations controlling the reaction pathway. Of particular interest is the observation that all observed vibrational resonances trigger the reaction as evidenced by the loss of the Ar atom and at least one water molecule. Most importantly, this includes excitation of the asymmetric CO stretch at 2343 cm^{-1} in the nominally neutral CO_2 molecule. Degradation of the v = 1 quantum in the CO_2 molecule to the background levels of the cluster must
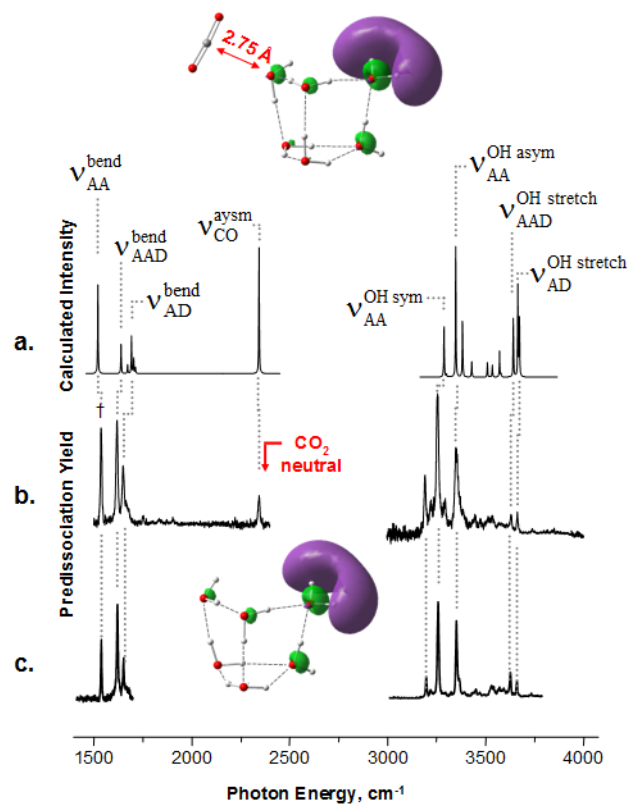
Figure A6: (a) Calculated (B3LYP/6-311+G(d,p)) harmonic spectrum of the $[CO_2 \cdot (H_2O)_6^-]$ minimum energy structure corresponding to the R isomer; (b) predissociation spectrum of $[CO_2 \cdot (H_2O)_6]^- \cdot Ar$; and (c) predissociation spectrum for $(H_2O)_6^- \cdot Ar_7$, detected by the loss of six Ar atoms, for comparison. The characteristic transitions associated with the unique AA water molecule are indicated by ν_{AA}^{symm}, ν_{AA}^{asymm} and ν_{AA}^{bend}(†).

therefore be faster than vibrational predissociation, as the CO_2 molecule is never lost as a fragment.[2] Electron autodetachment is also not observed for low energy excitation ($h\nu < 2350$ cm^{-1}), indicating that the barrier to reaction lies below the adiabatic detachment energy of the R isomer.

A.3.7 Unveiling the Pathway for Network-Mediated Chemistry through Molecular Dynamics Simulations

The empirical analysis of the spectra and photophysics provides a compelling scenario where a high-energy reaction intermediate R has been trapped and a water network-mediated electron-capture reaction has been triggered through vibrational excitation of either the neutral reactant or the OH stretch or HOH bend vibrations of the water monomers. It is natural to consider how this solvent dependent process occurs. For example, does the water network break apart prior to the electron transfer, and what type of new network must be assembled to shepherd the electron toward its eventual accommodation by the CO_2^- product anion? These questions were explored using "ab initio" molecular dynamics simulations in which the energies and forces are obtained on-the-fly using electronic structure calculations employing the BLYP[210] density functional method.

The simulations were carried out using the NVE ensemble and were initiated starting from the local minimum structure depicted in Figure A6, with the CO_2 at a site remote from the AA monomer and the associated excess electron. The experimental studies described above deposit energy into a specific vibrational mode, but as noted, this energy is expected to be rapidly equilibrated throughout the cluster prior to reaction. This situation corresponds to the statistical limit of unimolecular mechanics in the context of an internally excited microcanonical ensemble. Hence the simulations were started with the excess internal energy randomly distributed over the kinetic energies of the atoms.

The simulations were carried out with excess energies of 3466 and 3962 cm^{-1}, corresponding approximately to the total amount of internal energy in play after OH stretch excitation vibration of cluster targets prepared in the evaporative ensemble regime. Elec-

---

[2]Based on the behavior of related neutral and ionic clusters in this size range, the CO_2 molecule in the complex is expected to be bound by about 1400 cm^{-1}.[209] Because carbon dioxide is never observed to be lost as a neutral, the reaction barrier must lie below 1900 cm-1, due to BE(CO_2 + Ar), but this result is inconsequential for a reaction that proceeds with a transition state upper limit of 1500 cm^{-1}, obtained from our analysis in section A.3.4
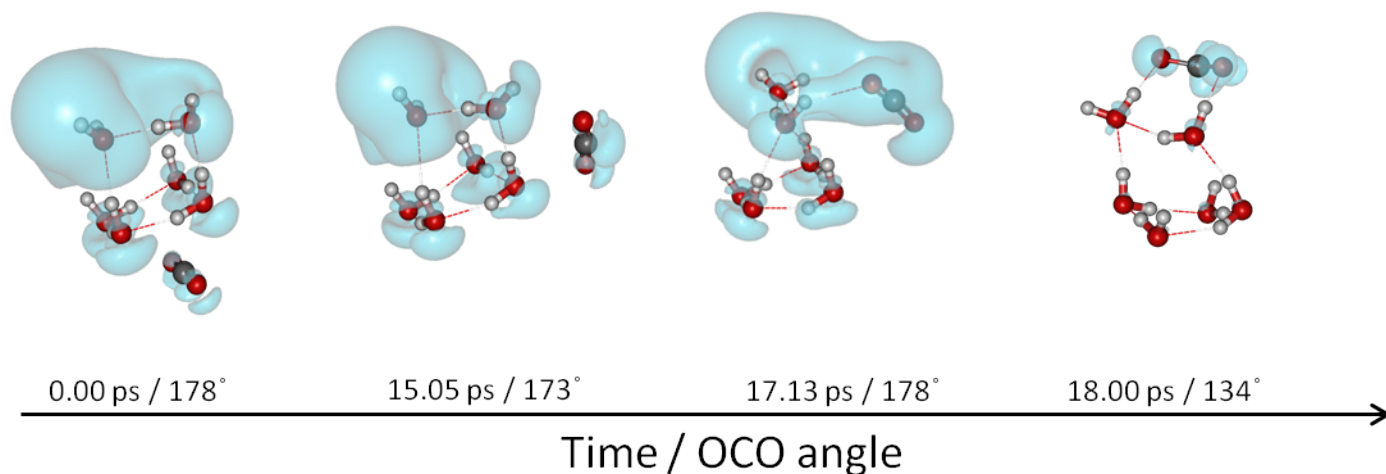
Figure A7: Snapshots of structures sampled at various times in an MD simulation using the BLYP functional and with an excess energy of 3466 cm^{-1}. The snapshots also show the surfaces that enclose 90% of the charge density of the excess electron and report the OCO angle for the selected structures. The arrow in the snapshots identifies the CO_2 molecule. In this trajectory the CO_2 molecule moves from the bottom of the water cluster to the side of the cluster where at about 15 ps the water monomer directly H-bonded to the AA monomer and with a free OH group rotates the later toward the CO_2 molecule. The angle between this OH group and the CO_2 molecule continues to evolve, leading to a structure with a small portion of the excess electron charge localized onto the CO_2 molecule (17.13 ps). The CO_2 molecule then quickly bends, accompanied by further localization of the excess electron onto the molecule.

tron transfer typically occurred in about 17 ps at an internal energy of 3466 cm^{-1}, which shortened to about 11 ps when the energy was increased to 3962 cm^{-1}. Because of the long computational times that would be required to achieve reaction, simulations were not attempted for internal energies consistent with photoactivation through the lower energy CO_2 asymmetric stretch or water bend vibrations.

A multitude of reactive pathways were observed depending on the initial conditions. This is not surprising given the fact that the potential energy surface of $(H_2O)_6^-$ itself displays a large number of local minima. many of which are separated by relatively small barriers.[70] In particular, we note that theoretical studies indicate that the barriers to escape from the AA type local minima are only about 200 m^{-1}, roughly half the energy that would be expected in the cluster before vibrational excitation. In spite of the wide diversity of pathways observed in the simulations, in all cases, the electron transfer event is triggered by partial accommodation of the CO_2 molecule into the H-bonding network, which, in turn, makes the CO_2 molecule a better electron acceptor.

Figure A7 depicts selected configurations from a trajectory with excess energy of 3466 cm^{-1} and for which the electron transfer to the CO_2 molecule occurs at about 17 ps. Interestingly, the water cluster retains the basic structure of the type I (AA-based) isomer until just before the electron transfers to the CO_2 molecule. It is clear from the depicted snapshots that the electron transfer is triggered by formation of an H-bond to the CO_2 molecule. The delocalization of the excess electron to the CO_2 molecule is accompanied by bending of the molecule. Further stabilization is provided by its engagement in a second H-bond as shown in the last snapshot in Figure A7. The pathway depicted in Figure A7 has the CO_2 migrating close to the AA water monomer before electron transfer, but there are also electron transfer pathways for which the CO_2 remains located near its initial position. For the latter cases, the reaction is triggered by breaking an H-bond of the water network to form an H-bond to the CO_2.

The pathway depicted in Figure A7 represents state-of-the-art application of simulation methods to an energized microcanonical ensemble that can undergo large amplitude motions including chemical reaction. It is useful to emphasize that in this description, the electrons are treated quantum mechanically but the nuclei move in a classical manner described by the forces calculated using density functional theory. As such, the vibrational zero-point

energy is not explicitly included. In addition, the nature and timescale of the energy transfer from the vibrational levels excited by the laser were not addressed. The utility of small scale cluster experiments is that they are sufficiently large to mimic the statistical approach to the transition state for reaction, but are also small enough that more advanced methods can be used to determine the importance of nuclear quantum effects in driving the dynamics. This interplay between theory and experiment will provide a central role for cluster-based experiments such as that described in this article for the foreseeable future.

A.4 CONCLUSIONS

The dynamics of water network-mediated CO_2 reduction are explored at the molecular level through the integration of cryogenic ion spectroscopy with theoretical simulations. An Ar-mediated condensation approach is used to attach a neutral CO_2 molecule to an anionic water hexamer cluster, thus trapping the reactants in a metastable assembly. We then photoexcite vibrational transitions of either the CO_2 or $(H_2O)_6^-$ to trigger the intracluster electron capture event. The vibrational action spectrum is analyzed to establish the structure of the reactant complex, while the evolution to the hydrated CO_2^- product is verified through the evaporative dissociation of the product cluster generated by the reaction exothermicity. The lack of vibrational mode-specificity in promoting the reaction points to a statistical mechanism taking place within the ansatz of the microcanonical ensemble. Molecular dynamics simulations reveal the key step to the reduction of CO_2 is an H-bond donation to neutral CO_2, making that adduct a better electron acceptor. One very interesting observation is that the molecular dynamics simulations indicate that the basic AA structure can persist for several picoseconds even when the excess energies are well above the expected (calculated) barriers for escaping from the AA excess electron binding motif.

APPENDIX B

SUPPLEMENTARY INFORMATION FOR NONVALENCE CORRELATION-BOUND ANIONS OF SPHERICAL FULLERENES

B.1   COMPARISON OF AB INITIO AND MODEL POTENTIALS FOR ELECTROSTATICS AND POLARIZATION

Figure B1 reports the electrostatic potentials of C_{60} and C_{240} from ab initio calculations and from the model potentials. For C_{60}, the ab initio electrostatic potential is reported at both the HF and second-order Möller-Plesset (MP2)[2] perturbation level of theory. The HF results are reported for both the atomic natural orbital double zeta (ANODZ[18]) and cc-pVDZ+s basis sets, while the MP2 results are reported only for the ANODZ basis set. The ANODZ basis set is of similar quality as the aug-cc-pVDZ[16,17] basis set but has the advantage of being less prone to linear dependency. The cc-pVDZ+s basis set was formed by adding the diffuse s function from the aug-cc-pVDZ basis set to the cc-pVDZ[16] basis set. For C_{60} the HF/ANODZ, HF/cc-pVDZ+s, and MP2/ANODZ electrostatic potentials are in close agreement and, as a result only the HF/cc-pVDZ+s method was used to calculate the electrostatic potential of C_{240}.

The shaded regions in Figure B1 indicate the van der Waals diameter of the carbon atoms. Most importantly, except for the van der Waals region, the atomic dipole model closely reproduces the ab initio electrostatic potentials. The deviation between the model and ab initio electrostatic potentials just outside the van der Waals region is due to the tail of the charge density of the fullerene. The charge penetration effects in the tail regions are effectively absorbed in the repulsive potential.
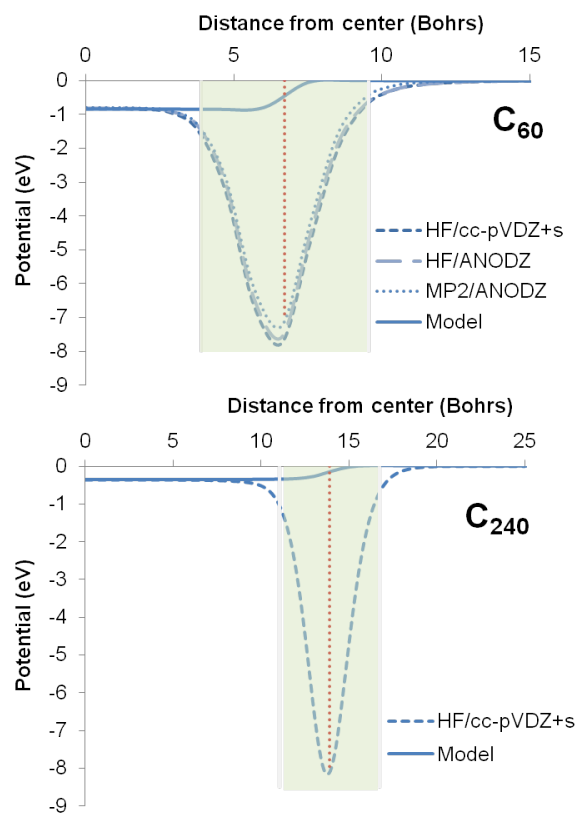
Figure B1: Electrostatic potentials of C_{60} and C_{240} from ab initio and model potential calculations for a negative point charge. For C_{60} the potential is plotted along a line passing through the middle of a C-C bond, while for C_{240} the potential is plotted along a line passing through a the center of a pentagonal ring.

Figure B2 compares the model and ab initio polarization potentials for C_{60} and C_{240}. The model polarization potentials closely reproduce the ab initio polarization potentials outside the van der Waals region.

B.2 DAMPING FUNCTION

The short-range divergence electron-water electrostatic and polarization potential is avoided by replacing R_{ie} with an effective distance R_{ie}^{eff} defined as

$$R_{ie}^{eff} = \begin{cases} R_{ie}, & if\ R_{ie} \geq d; \\ d\left(\frac{1}{2} + \left(\frac{R_{ie}}{d}\right)^3 \left(1 - \frac{R_{ie}}{2d}\right)\right), & if\ R_{ie} < d. \end{cases} \tag{B.1}$$

For electrostatic potential the damping parameter, d, is chosen to be 1.7 Bohrs. It should be noted that the electron binding energies are relatively insensitive to the choice of the damping parameter for the electrostatics. For polarization potential, the d parameter was chosen to be 5.7 Bohrs, such that the model potential including the polarization gives the same EBE of C_{60} (0.13 eV) as obtained from the EOM-CCSD calculations.

B.3 PARAMETRIZATION OF REPULSIVE POTENTIAL

In order to determine the a and b parameters of Eq. 6.4 of main text, an excess charge of 0.002 - 0.005 was added to each carbon atom of C_{60} so as to give a weakly-bound diffuse A_{1g} anion state in the ab initio Koopmans' theorem (KT)[1] approximation. The a and b parameters were then chosen so that the model potential (neglecting polarization) reproduces the ab initio KT electron binding energy (EBE) and also to have approximately the same amount of charge of the excess electron inside the cage as obtained in the EOM-CCSD calculations.
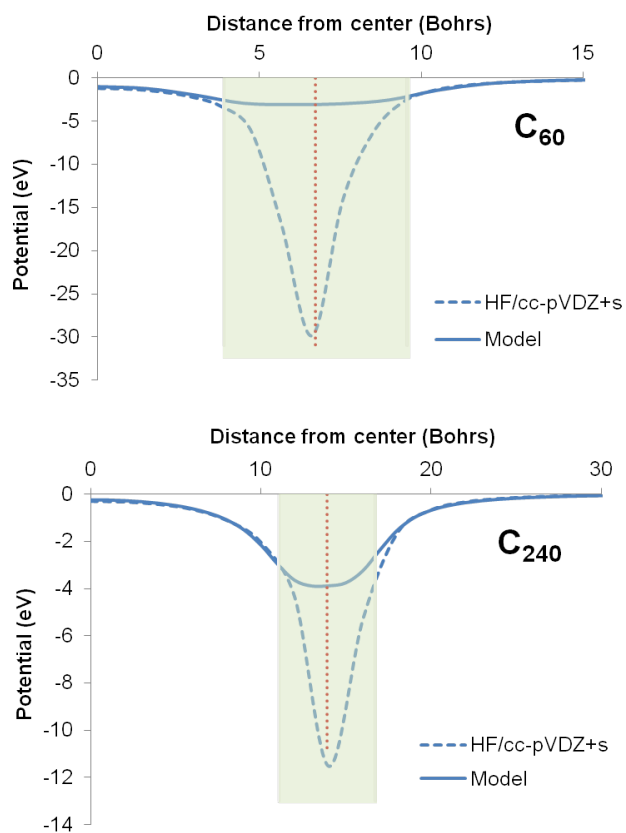
Figure B2: Polarization potentials of C_{60} and C_{240} from ab initio and model potential calculations. For C_{60} the potential is plotted along a line passing through the middle of a C-C bond, while for C_{240} the potential is plotted along a line passing through the center of a pentagonal ring.

B.4 CONSTRAINED CHARGE-FLOW EQUATIONS

The total energy of a configuration of induced atomic charges and dipoles is given by

$$
E_{tot} = \quad \frac{1}{2} \begin{pmatrix} \mathbf{q} & \mathbf{p} \end{pmatrix} \cdot \begin{pmatrix} \mathbf{T^{qq}} & -\mathbf{T^{qp}} \\ -\mathbf{T^{pq}} & -\mathbf{T^{pp}} \end{pmatrix} \cdot \begin{pmatrix} \mathbf{q} \\ \mathbf{p} \end{pmatrix}
$$
$$
+ \begin{pmatrix} \mathbf{q} & \mathbf{p} \end{pmatrix} \cdot \begin{pmatrix} \boldsymbol{\chi} + \mathbf{V^{ext}} \\ -\mathbf{E^{ext}} \end{pmatrix}, \tag{B.2}
$$

where $\mathbf{q}$ and $\mathbf{p}$ are, respectively, the vectors of net charges and induced dipoles on the atoms. $\mathbf{T^{qq}}$, $\mathbf{T^{qp}}$ and $\mathbf{T^{pp}}$ are the charge-charge, charge-dipole and dipole-dipole interaction matrices, respectively. They have been comprehensively discussed elsewhere.[125,126] $\boldsymbol{\chi}$ is the vector of electronegativities of the atoms of the system of interest. $\mathbf{V^{ext}}$ and $\mathbf{E^{ext}}$ are, respectively, the vectors consisting of external potential and fields felt at the atomic sites. The charges and dipoles are determined from the requirement that:

$$
\frac{dE_{tot}}{dq} = \frac{dE_{tot}}{dp_i^x} = \frac{dE_{tot}}{dp_i^y} = \frac{dE_{tot}}{dp_i^z} = 0. \tag{B.3}
$$

In addition, the model allows for the restriction of net zero charge on individual fullerene molecules. This constraint was used for $(C_{60})_2$ but not for $C_{60}@C_{240}$. The constrained charge-flow equation for energy is given as:

$$
f = E_{tot} + \sum_{k}^{N_f} \lambda_k \left(\sum_{i \,\epsilon\, k} q_{i,k} - Q_k^{tot} \right), \tag{B.4}
$$

where λ_k is the Lagrange multiplier of the kth fullerene, Q_k^{tot} is the total charge of the isolated fullerene and $q_{i,k}$ is the charge on the ith atom of the kth fullerene. N_f is the total number of fullerenes. f is minimized with respect to charges, dipoles and the Lagrange

multipliers, λ_k. This leads to a set of $4N+N_f$ equations which can be written in a matrix form. For a two fullerene system, the equations can be written in the following matrix form:

$$
\begin{pmatrix}
\mathbf{T}_{1,1}^{qq} & \mathbf{T}_{1,2}^{qq} & -\mathbf{T}_{1,1}^{qp} & -\mathbf{T}_{1,2}^{qp} & 1 & 0 \\
\mathbf{T}_{2,1}^{qq} & \mathbf{T}_{2,2}^{qq} & -\mathbf{T}_{2,1}^{qp} & -\mathbf{T}_{2,2}^{qp} & 0 & 1 \\
-\mathbf{T}_{1,1}^{pq} & -\mathbf{T}_{1,2}^{pq} & -\mathbf{T}_{1,1}^{pp} & -\mathbf{T}_{1,2}^{pp} & 0 & 0 \\
-\mathbf{T}_{2,1}^{pq} & -\mathbf{T}_{2,2}^{pq} & -\mathbf{T}_{2,1}^{pp} & -\mathbf{T}_{2,2}^{pp} & 0 & 0 \\
1 & 0 & 0 & 0 & 0 & 0 \\
0 & 1 & 0 & 0 & 0 & 0
\end{pmatrix}
\begin{pmatrix}
\mathbf{q_1} \\ \mathbf{q_2} \\ \mathbf{p_1} \\ \mathbf{p_2} \\ \lambda_1 \\ \lambda_2
\end{pmatrix}
=
\begin{pmatrix}
-\boldsymbol{\chi}_1 - \mathbf{V}_1 \\
-\boldsymbol{\chi}_2 - \mathbf{V}_2 \\
\mathbf{E}_1 \\
\mathbf{E}_2 \\
\mathbf{Q}_1^{tot} \\
\mathbf{Q}_2^{tot}
\end{pmatrix} .
\tag{B.5}
$$

Alternately, given the external field and the potential one can determine the induced charges and dipoles as:

$$
\begin{pmatrix}
\mathbf{q_1} \\ \mathbf{q_2} \\ \mathbf{p_1} \\ \mathbf{p_2} \\ \lambda_1 \\ \lambda_2
\end{pmatrix}
=
\begin{pmatrix}
\mathbf{T}_{1,1}^{qq} & \mathbf{T}_{1,2}^{qq} & -\mathbf{T}_{1,1}^{qp} & -\mathbf{T}_{1,2}^{qp} & 1 & 0 \\
\mathbf{T}_{2,1}^{qq} & \mathbf{T}_{2,2}^{qq} & -\mathbf{T}_{2,1}^{qp} & -\mathbf{T}_{2,2}^{qp} & 0 & 1 \\
-\mathbf{T}_{1,1}^{pq} & -\mathbf{T}_{1,2}^{pq} & -\mathbf{T}_{1,1}^{pp} & -\mathbf{T}_{1,2}^{pp} & 0 & 0 \\
-\mathbf{T}_{2,1}^{pq} & -\mathbf{T}_{2,2}^{pq} & -\mathbf{T}_{2,1}^{pp} & -\mathbf{T}_{2,2}^{pp} & 0 & 0 \\
1 & 0 & 0 & 0 & 0 & 0 \\
0 & 1 & 0 & 0 & 0 & 0
\end{pmatrix}^{-1}
\begin{pmatrix}
-\boldsymbol{\chi}_1 \\
-\boldsymbol{\chi}_2 \\
0 \\
0 \\
\mathbf{Q}_1^{tot} \\
\mathbf{Q}_2^{tot}
\end{pmatrix}
$$

$$
+
\begin{pmatrix}
\mathbf{T}_{1,1}^{qq} & \mathbf{T}_{1,2}^{qq} & -\mathbf{T}_{1,1}^{qp} & -\mathbf{T}_{1,2}^{qp} & 1 & 0 \\
\mathbf{T}_{2,1}^{qq} & \mathbf{T}_{2,2}^{qq} & -\mathbf{T}_{2,1}^{qp} & -\mathbf{T}_{2,2}^{qp} & 0 & 1 \\
-\mathbf{T}_{1,1}^{pq} & -\mathbf{T}_{1,2}^{pq} & -\mathbf{T}_{1,1}^{pp} & -\mathbf{T}_{1,2}^{pp} & 0 & 0 \\
-\mathbf{T}_{2,1}^{pq} & -\mathbf{T}_{2,2}^{pq} & -\mathbf{T}_{2,1}^{pp} & -\mathbf{T}_{2,2}^{pp} & 0 & 0 \\
1 & 0 & 0 & 0 & 0 & 0 \\
0 & 1 & 0 & 0 & 0 & 0
\end{pmatrix}^{-1}
\begin{pmatrix}
-\mathbf{V}_1 \\
-\mathbf{V}_2 \\
\mathbf{E}_1 \\
\mathbf{E}_2 \\
0 \\
0
\end{pmatrix} .
\tag{B.6}
$$

The inverse matrix on the right hand side of Eq. B.6 is the molecular polarizability matrix $\boldsymbol{\alpha}^{fullerene}$. The second term on the right hand side of Eq. B.6 represents the polarization effects due to external fields on the atoms of the fullerenes. Therefore only the second term contributes to the induced moments. Eq. B.6 can be expressed as:

$$
\mathbf{M}^{net} = \boldsymbol{\alpha}^{fullerene} \cdot \boldsymbol{\chi}^0 + \boldsymbol{\alpha}^{fullerene} \cdot \mathbf{F}^{ext},
\tag{B.7}
$$

where

$$\mathbf{M}^{net} = \begin{pmatrix} \mathbf{q_1} \\ \mathbf{q_2} \\ \mathbf{p_1} \\ \mathbf{p_2} \\ \boldsymbol{\lambda}_1 \\ \boldsymbol{\lambda}_2 \end{pmatrix}, \boldsymbol{\chi}^0 = \begin{pmatrix} -\boldsymbol{\chi}_1 \\ -\boldsymbol{\chi}_2 \\ \mathbf{0} \\ \mathbf{0} \\ \mathbf{Q_1^{tot}} \\ \mathbf{Q_2^{tot}} \end{pmatrix}, \mathbf{F}^{ext} = \begin{pmatrix} -\mathbf{V_1} \\ -\mathbf{V_2} \\ \mathbf{E_1} \\ \mathbf{E_2} \\ \mathbf{0} \\ \mathbf{0} \end{pmatrix}, \tag{B.8}$$

and

$$\boldsymbol{\alpha}^{fullerene} = \begin{pmatrix} \mathbf{T_{1,1}^{qq}} & \mathbf{T_{1,2}^{qq}} & -\mathbf{T_{1,1}^{qp}} & -\mathbf{T_{1,2}^{qp}} & \mathbf{1} & \mathbf{0} \\ \mathbf{T_{2,1}^{qq}} & \mathbf{T_{2,2}^{qq}} & -\mathbf{T_{2,1}^{qp}} & -\mathbf{T_{2,2}^{qp}} & \mathbf{0} & \mathbf{1} \\ -\mathbf{T_{1,1}^{pq}} & -\mathbf{T_{1,2}^{pq}} & -\mathbf{T_{1,1}^{pp}} & -\mathbf{T_{1,2}^{pp}} & \mathbf{0} & \mathbf{0} \\ -\mathbf{T_{2,1}^{pq}} & -\mathbf{T_{2,2}^{pq}} & -\mathbf{T_{2,1}^{pp}} & -\mathbf{T_{2,2}^{pp}} & \mathbf{0} & \mathbf{0} \\ \mathbf{1} & \mathbf{0} & \mathbf{0} & \mathbf{0} & \mathbf{0} & \mathbf{0} \\ \mathbf{0} & \mathbf{1} & \mathbf{0} & \mathbf{0} & \mathbf{0} & \mathbf{0} \end{pmatrix}^{-1}. \tag{B.9}$$

The second term in Eq. B.7 gives $\mathbf{M}^{ind}$

$$\mathbf{M}^{ind} = \boldsymbol{\alpha}^{fullerene} \cdot \mathbf{F}^{ext}. \tag{B.10}$$

BIBLIOGRAPHY

[1] Koopmans, T. *Physica* **1934**, *1*, 104–113.

[2] Mller, C.; Plesset, M. S. *Phys. Rev.* **1934**, *46*, 618–622.

[3] Pople, J. A.; Head-Gordon, M.; Raghavachari, K. *J. Chem. Phys.* **1987**, *87*, 5968–5975.

[4] Schirmer, J.; Cederbaum, L. S.; Walter, O. *Phys. Rev. A* **1983**, *28*, 1237–1259.

[5] Nooijen, M.; Bartlett, R. J. *J. Chem. Phys.* **1995**, *102*, 3629–3647.

[6] Bozkaya, U.; Turney, J. M.; Yamaguchi, Y.; Schaefer, H. F.; Sherrill, C. D. *J. Chem. Phys.* **2011**, *135*, 1041031.

[7] Neese, F.; Schwabe, T.; Kossmann, S.; Schirmer, B.; Grimme, S. *Journal of Chemical Theory and Computation* **2009**, *5*, 3060–3073.

[8] Handy, N. C.; Pople, J. A.; Head-Gordon, M.; Raghavachari, K.; Trucks, G. W. *Chem. Phys. Lett.* **1989**, *164*, 185 – 192.

[9] Nooijen, M.; Snijders, J. G. *J. Chem. Phys.* **1995**, *102*, 1681–1688.

[10] Stanton, J. F.; Gauss, J. *J. Chem. Phys.* **1995**, *103*, 1064–1076.

[11] Sommerfeld, T.; Bhattarai, B.; Vysotskiy, V. P.; Cederbaum, L. S. *J. Chem. Phys.* **2010**, *133*, 114301.

[12] Bezchastnov, V. G.; Vysotskiy, V. P.; Cederbaum, L. S. *Phys. Rev. Lett.* **2011**, *107*, 133401.

[13] Voora, V. K.; Cederbaum, L. S.; Jordan, K. D. *J. Phys. Chem. Lett.* **2013**, *4*, 849–853.

[14] Voora, V. K.; Jordan, K. D. *J. Phys. Chem. A* 10.1021/jp408386f.

[15] Vysotskiy, V. P.; Cederbaum, L. S.; Sommerfeld, T.; Voora, V. K.; Jordan, K. D. *J. Chem. Theory Comput.* **2012**, *8*, 893–900.

[16] Dunning Jr., T. H. *J. Chem. Phys.* **1989**, *90*, 1007–1023.

[17] Kendall, R. A.; Dunning Jr., T. H.; Harrison, R. J. *J. Chem. Phys.* **1992**, *96*, 6796–6806.

[18] Widmark, P.-O.; Malmqvist, P.-k.; Roos, B. *Theor. Chim. Acta* **1990**, *77*, 291–306.

[19] Sommerfeld, T. *J. Phys. B* **2003**, *36*, L127.

[20] Stanton, J.; Gauss, J.; Harding, M.; Szalay, P. *CFOUR, Coupled-Cluster Techniques for Computational Chemistry* **2010**,

[21] Turney, J. M. et al. *WIREs Comput. Mol. Sci.* **2012**, *2*, 556–565.

[22] Hedin, L. *Phys. Rev.* **1965**, *139*, A796–A823.

[23] Chowdhury, S.; Kebarle, P. *J. Am. Chem. Soc.* **1986**, *108*, 5453–5459.

[24] Turi, L.; Sheu, W.-S.; Rossky, P. J. *Science* **2005**, *309*, 914–917.

[25] Verlet, J.; Bragg, A.; Kammrath, A.; Cheshnovsky, O.; Neumark, D. *Science* **2005**, *307*, 93–96.

[26] Barnett, R. N.; Landman, U.; Cleveland, C. L.; Jortner, J. *Phys. Rev. Lett.* **1987**, *59*, 811–814.

[27] Turi, L.; Madarsz, A.; Rossky, P. *J. Chem. Phys.* **2006**, *125*, 014308.

[28] Asmis, K.; Santambrogio, G.; Zhou, J.; Garand, E.; Headrick, J.; Goebbert, D.; Johnson, M.; Neumark, D. *J. Chem. Phys.* **2007**, *126*, 191105.

[29] Bragg, A. E.; Verlet, J. R. R.; Kammrath, A.; Cheshnovsky, O.; Neumark, D. M. *J. Am. Chem. Soc.* **2005**, *127*, 15283–15295.

[30] Barnett, R. N.; Landman, U.; Cleveland, C. L.; Jortner, J. *J. Chem. Phys.* **1988**, *88*, 4429–4447.

[31] Barnett, R.; Landman, U.; Cleveland, C.; Jortner, J. *J. Chem. Phys.* **1988**, *88*, 4421–4428.

[32] Schnitker, J.; Rossky, P. J. *J. Chem. Phys.* **1987**, *86*, 3462–3470.

[33] Turi, L.; Borgis, D. *J. Chem. Phys.* **2002**, *117*, 6186–6195.

[34] Turi, L.; Gaigeot, M.-P.; Levy, N.; Borgis, D. *J. Chem. Phys.* **2001**, *114*, 7805–7815.

[35] Jacobson, L. D.; Williams, C. F.; Herbert, J. M. *J. Chem. Phys.* **2009**, *130*, 124115.

[36] Sommerfeld, T.; DeFusco, A.; Jordan, K. D. *J. Phys. Chem. A* **2008**, *112*, 11021–11035.

[37] Wang, F.; Jordan, K. D. *J. Chem. Phys.* **2002**, *116*, 6973–6981.

[38] Sommerfeld, T.; Jordan, K. *J. Am. Chem. Soc.* **2006**, *128*, 5828–5833.

[39] Sommerfeld, T.; Jordan, K. D. *J. Phys. Chem. A* **2005**, *109*, 11531–11538.

[40] Sommerfeld, T.; Gardner, S.; DeFusco, A.; Jordan, K. *J. Chem. Phys.* **2006**, *125*, 174301.

[41] Jacobson, L.; Herbert, J. *J. Chem. Phys.* **2010**, *133*, 154506.

[42] Wang, F.; Jordan, K. *J. Chem. Phys.* **2003**, *119*, 11645–11653.

[43] Ben-Amotz, D. *J. Phys. Chem. Lett.* **2011**, *2*, 1216–1222.

[44] Larsen, R. E.; Glover, W. J.; Schwartz, B. J. *Science* **2010**, *329*, 65–69.

[45] Jacobson, L. D.; Herbert, J. M. *Science* **2011**, *331*, 1387.

[46] Turi, L.; Madarasz, A. *Science* **2011**, *331*, 1387–c.

[47] Gutowski, M.

[48] Herbert, J.; Head-Gordon, M. *J. Phys. Chem. A* **2005**, *109*, 5217–5229.

[49] Herbert, J.; Head-Gordon, M. *Phys. Chem. Chem. Phys.* **2006**, *8*, 68–78.

[50] Hehre, W.; Ditchfield, K.; Pople, J. *J. Chem. Phys.* **1972**, *56*, 2257–2261.

[51] Frigato, T.; Vondele, J.; Schmidt, B.; Schtte, C.; Jungwirth, P. *J. Phys. Chem. A* **2008**, *112*, 6125–6133.

[52] Becke, A. *J. Chem. Phys.* **1993**, *98*, 1372–1377.

[53] Rienstra-Kiracofe, J.; Tschumper, G.; Schaefer III, H.; Nandi, S.; Ellison, G. *Chem. Rev.* **2002**, *102*, 231–282.

[54] Schirmer, J.; Mertins, F. *Int. J. Quantum Chem.* **1996**, *58*, 329–339.

[55] Sommerfeld, T. *J. Phys. Chem. A* **2008**, *112*, 11817–11823.

[56] Feuerbacher, S.; Sommerfeld, T.; Santra, R.; Cederbaum, L. *J. Chem. Phys.* **2003**, *118*, 6188–6199.

[57] Davis, D.; Vysotskiy, V.; Sajeev, Y.; Cederbaum, L. *Angew. Chem., Int. Ed.* **2011**, *50*, 4119–4122.

[58] Simons, J.; Smith, W. *J. Chem. Phys.* **1973**, *58*, 4899–4907.

[59] Beebe, N.; Linderberg, J. *Int. J. Quantum Chem.* **1977**, *12*, 683–705.

[60] Vysotskiy, V. P.; Cederbaum, L. S. *J. Chem. Phys.* **2010**, *132*, 044110.

[61] Harding, M.; Metzroth, T.; Gauss, J.; Auer, A. *J. Chem. Theory Comput.* **2008**, *4*, 64–74.

[62] Aquilante, F.; De Vico, L.; Ferr, N.; Ghigo, G.; Malmqvist, P.-.; Neogrdy, P.; Peder-sen, T.; Pitok, M.; Reiher, M.; Roos, B.; Serrano-Andrs, L.; Urban, M.; Veryazov, V.; Lindh, R. *J. Comput. Chem.* **2010**, *31*, 224–247.

[63] Hammer, N.; Roscioli, J.; Johnson, M. *J. Phys. Chem. A* **2005**, *109*, 7896–7901.

[64] Feng, D.-F.; Kevan, L. *Chem. Rev.* **1980**, *80*, 1–20.

[65] Chipman, D. *Theor. Chim. Acta* **1989**, *76*, 73–84.

[66] Simons, J. *J. Phys. Chem. A* **2010**, *114*, 8631–8643.

[67] Wang, F.; Jordan, K. *J. Chem. Phys.* **2001**, *114*, 10717–10724.

[68] Siefermann, K. R.; Liu, Y.; Lugovoy, E.; Link, O.; Faubel, M.; Buck, U.; Winter, B.; Abel, B. *Nature Chem.* **2010**, *2*, 274–279.

[69] Hammer, N. I.; Roscioli, J. R.; Bopp, J. C.; Headrick, J. M.; Johnson, M. A. *J. Chem. Phys.* **2005**, *123*, 244311.

[70] Choi, T. H.; Jordan, K. D. *Chem. Phys. Lett.* **2009**, *475*, 293 – 297.

[71] Stampfli, P. *Phys. Rep.* **1995**, *255*, 1 – 77.

[72] Gutowski, M.; Skurski, P.; Boldyrev, A. I.; Simons, J.; Jordan, K. D. *Phys. Rev. A* **1996**, *54*, 1906–1909.

[73] Ren, P.; Ponder, J. W. *J. Phys. Chem. B* **2003**, *107*, 5933–5947.

[74] Defusco, A.; Schofield, D. P.; Jordan, K. D. *Mol. Phys.* **2007**, *105*, 2681–2696.

[75] Thole, B. *Chem. Phys.* **1981**, *59*, 341 – 350.

[76] Light, J. C.; Carrington, T. *Advances in Chemical Physics*; John Wiley and Sons, Inc., 2007; pp 263–310.

[77] Raghavachari, K.; Trucks, G. W.; Pople, J. A.; Head-Gordon, M. *Chem. Phys. Lett.* **1989**, *157*, 479 – 483.

[78] Sommerfeld, T.; Choi, T.-H.; Voora, V. K.; Jordan, K. D. *Pittsburgh InfraStructure for Clusters with Excess ElectronS, PISCES, www.pisces.pitt.edu*

[79] Choi, T. H.; Sommerfeld, T.; Yilmaz, S. L.; Jordan, K. D. *J. Chem. Theory Comput.* **2010**, *6*, 2388–2394.

[80] Mones, L.; Turi, L. *J. Chem. Phys.* **2010**, *132*, 154507.

[81] Mones, L.; Rossky, P. J.; Turi, L. *J. Chem. Phys.* **2011**, *135*, 084501.

[82] Wang, X.-B.; Woo, H.-K.; Wang, L.-S. *J. Chem. Phys.* **2005**, *123*, 051106.

[83] Green, W. H.; Gorun, S. M.; Fitzgerald, G.; Fowler, P. W.; Ceulemans, A.; Titeca, B. C. *J. Phys. Chem.* **1996**, *100*, 14892–14898.

[84] Reed, C. A.; Bolskar, R. D. *Chem. Rev.* **2000**, *100*, 1075–1120.

[85] Cammarata, V.; Guo, T.; Illies, A.; Li, L.; Shevlin, P. *J. Phys. Chem. A* **2005**, *109*, 2765–2767.

[86] Difley, S.; Simons, J. *Int. J. Quantum Chem.* **2006**, *106*, 507–513.

[87] Yang, S.; Pettiette, C.; Conceicao, J.; Cheshnovsky, O.; Smalley, R. *Chem. Phys. Lett.* **1987**, *139*, 233 – 238.

[88] Amusia, M.; Baltenkov, A.; Krakov, B. *Phys. Lett. A* **1998**, *243*, 99 – 105.

[89] Voora, V. K.; Ding, J.; Sommerfeld, T.; Jordan, K. D. *J. Phys. Chem. B* **2013**, *117*, 4365–4370.

[90] Huang, J.; Carman, H. S.; Compton, R. N. *J. Phys. Chem.* **1995**, *99*, 1719–1726.

[91] Jaffke, T.; Illenberger, E.; Lezius, M.; Matejcik, S.; Smith, D.; Mrk, T. D. *Chem. Phys. Lett.* **1994**, *226*, 213 – 218.

[92] Smith, D.; panel, P.; Mrk, T. D. *Chem. Phys. Lett.* **1993**, *213*, 202 – 206.

[93] Smith, D.; Spanel, P. *J. Phys. B* **1996**, *29*, 5199.

[94] Finch, C.; Popple, R.; Nordlander, P.; Dunning, F. *Chem. Phys. Lett.* **1995**, *244*, 345 – 349.

[95] Weber, J. M.; Ruf, M.-W.; Hotop, H. *Z. Phys. D: At. Mol. Clusters* **1996**, *37*, 351.

[96] Elhamidi, O.; Pommier, J.; Abouaf, R. *J. Phys. B* **1997**, *30*, 4633.

[97] Prabhudesai, V.; Nandi, D.; Krishnakumar, E. *European Physical Journal D* **2005**, *35*, 261–266.

[98] Viggiano, A.; Friedman, J.; Shuman, N.; Miller, T.; Schaffer, L.; Troe, J. *J. Chem. Phys.* **2010**, *132*, 194307.

[99] Kasperovich, V.; Tikhonov, G.; Kresin, V. *Chem. Phys. Lett.* **2001**, *337*, 55–60.

[100] Lezius, M.; Scheier, P.; Mrk, T. *Chem. Phys. Lett.* **1993**, *203*, 232–236.

[101] Alberg, M.; Bawin, M.; Brau, F. *Phys. Rev. A* **2005**, *71*, 022108.

[102] Pavlyukh, Y.; Berakdar, J. *J. Chem. Phys.* **2011**, *135*, 201103.

[103] Feng, M.; Zhao, J.; Petek, H. *Science* **2008**, *320*, 359–362.

[104] Feng, M.; Zhao, J.; Huang, T.; Zhu, X.; Petek, H. *Acc. Chem. Res.* **2011**, *44*, 360–368.

[105] Zhu, X.-Y.; Dutton, G.; Quinn, D. P.; Lindstrom, C. D.; Schultz, N. E.; Truhlar, D. G. *Phys. Rev. B* **2006**, *74*, 241401.

[106] Weaver, J.; Martins, J.; Komeda, T.; Chen, Y.; Ohno, T.; Kroll, G.; Troullier, N.; Haufler, R.; Smalley, R. *Phys. Rev. Lett.* **1991**, *66*, 1741–1744.

[107] Jensen, F. *J. Chem. Theory Comput.* **2010**, *6*, 2726–2735.

[108] Tozer, D.; De Proft, F. *J. Chem. Phys.* **2007**, *127*, 034108.

[109] Gutowski, M.; Jordan, K.; Skurski, P. *J. Phys. Chem. A* **1998**, *102*, 2624–2633.

[110] Hedberg, K.; Hedberg, L.; Bethune, D.; Brown, C.; Dorn, H.; Johnson, R.; De Vries, M. *Science* **1991**, *254*, 410–412.

[111] Lowdin, P.-O. *Phys. Rev.* **1955**, *97*, 1474–1489.

[112] Stone, A. *J. Chem. Theory Comput.* **2005**, *1*, 1128–1132.

[113] Stone, A. *The Theory of Intermolecular Forces* **1996**,

[114] De Proft, F.; Van Alsenoy, C.; Geerlings, P. *J. Phys. Chem.* **1996**, *100*, 7440–7448.

[115] Antoine, R.; Dugourd, P.; Rayane, D.; Benichou, E.; Broyer, M.; Chandezon, F.; Guet, C. *J. Chem. Phys.* **1999**, *110*, 9771–9772.

[116] Lucchese, R.; Gianturco, F.; Sanna, N. *Chem. Phys. Lett.* **1999**, *305*, 413–418.

[117] Winstead, C.; McKoy, V. *Phys. Rev. A* **2006**, *73*, 012711.

[118] Ensing, B.; Costanzo, F.; Silvestrelli, P. *J. Phys. Chem. A* **2012**, *116*, 12184–12188.

[119] Vondrak, T.; Zhu, X.-Y. *J. Phys. Chem. B* **1999**, *103*, 3449–3456.

[120] Dougherty, D. B.; Feng, M.; Petek, H.; Yates, J. T.; Zhao, J. *Phys. Rev. Lett.* **2012**, *109*, 266802.

[121] Silkin, V. M.; Zhao, J.; Guinea, F.; Chulkov, E. V.; Echenique, P. M.; Petek, H. *Phys. Rev. B* **2009**, *80*, 121408.

[122] Craes, F.; Runte, S.; Klinkhammer, J.; Kralj, M.; Michely, T.; Busse, C. *Phys. Rev. Lett.* **2013**, *111*, 056804.

[123] Granger, B. E.; Král, P.; Sadeghpour, H. R.; Shapiro, M. *Phys. Rev. Lett.* **2002**, *89*, 135506.

[124] Zamkov, M.; Woody, N.; Shan, B.; Chakraborty, H. S.; Chang, Z.; Thumm, U.; Richard, P. *Phys. Rev. Lett.* **2004**, *93*, 156803.

[125] Mayer, A. *Phys. Rev. B* **2007**, *75*, 045407.

[126] Mayer, A.; Astrand, P.-O. *J. Phys. Chem. A* **2008**, *112*, 1277–1285.

[127] Chen, J.; Martnez, T. J. *Chem. Phys. Lett.* **2007**, *438*, 315 – 320.

[128] Chen, J.; Martnez, T. J. *J. Chem. Phys.* **2009**, *131*, 044114.

[129] Gumbs, G.; Balassis, A.; Iurov, A.; Fekete, P. *The Scientific World Journal* **2014**, *2014*, 726303.

[130] Hazi, A. U.; Taylor, H. S. *Phys. Rev. A* **1970**, *1*, 1109–1120.

[131] Faidas, H.; Christophorou, L.; McCorkle, D. *Chem. Phys. Lett.* **1992**, *193*, 487 – 492.

[132] Miller, T. M.; Doren, J. M. V.; Viggiano, A. *Int. J. Mass Spectrom.* **2004**, *233*, 67 – 73.

[133] Nakajima, A.; Taguwa, T.; Hoshino, K.; Sugioka, T.; Naganuma, T.; Oho, F.; Watanabe, K.; Nakao, K.; Konishi, Y.; Kishi, R.; Kaya, K. *Chem. Phys. Lett.* **1993**, *214*, 22 – 26.

[134] Shchegoleva, L.; Bilkis, I.; Schastnev, P. *Chem. Phys.* **1983**, *82*, 343 – 353.

[135] Wentworth, W. E.; Limero, T.; Chen, E. C. M. *J. Phys. Chem.* **1987**, *91*, 241–245.

[136] Field, D.; Jones, N. C.; Ziesel, J.-P. *Phys. Rev. A* **2004**, *69*, 052716.

[137] Cho, H.; Gulley, R. J.; Sunohara, K.; Kitajima, M.; Uhlmann, L. J.; Tanaka, H.; Buckman, S. J. *J. Phys. B* **2001**, *34*, 1019.

[138] Holroyd, R. A.; Schmidt, W. *Annu. Rev. Phys. Chem.* **1989**, *40*, 439–468.

[139] Suess, L.; Parthasarathy, R.; Dunning, F. B. *J. Chem. Phys.* **2002**, *117*, 11222–11227.

[140] Finch, C. D.; Parthasarathy, R.; Hill, S. B.; Dunning, F. B. *J. Chem. Phys.* **1999**, *111*, 7316–7320.

[141] Ingólfsson, O.; Illenberger, E. *Int. J. Mass Spectrom. Ion Processes* **1995**, *149150*, 79 – 86.

[142] Frazier, J. R.; Christophorou, L. G.; Carter, J. G.; Schweinler, H. C. *J. Chem. Phys.* **1978**, *69*, 3807–3818.

[143] Eustis, S. N.; Wang, D.; Bowen, K. H.; Naresh Patwari, G. *J. Chem. Phys.* **2007**, *127*, 114312.

[144] Shchegoleva, L.; Beregovaya, I.; Schastnev, P. *Chem. Phys. Lett.* **1999**, *312*, 325 – 332.

[145] Gahl, C.; Ishioka, K.; Zhong, Q.; Hotzel, A.; Wolf, M. *Faraday Discuss.* **2000**, *117*, 191–202.

[146] Kirchmann, P. S.; Loukakos, P. A.; Bovensiepen, U.; Wolf, M. *New. J. Phys.* **2005**, *7*, 113.

[147] Föhlisch, A.; Vijayalakshmi, S.; Pietzsch, A.; Nagasono, M.; Wurth, W.; Kirch-mann, P.; Loukakos, P.; Bovensiepen, U.; Wolf, M.; Tchaplyguine, M.; Hennies, F. *Surf. Sci.* **2012**, *606*, 881 – 885.

[148] Headrick, J.; Diken, E.; Walters, R.; Hammer, N.; Christie, R.; Cui, J.; Myshakin, E.; Duncan, M.; Johnson, M.; Jordan, K. *Science* **2005**, *308*, 1765–1769.

[149] Singh, N.; Park, M.; Seung, K.; Seung, B.; Kim, K. *Angew. Chem., Int. Ed.* **2006**, *45*, 3795–3800.

[150] Jiang, J.-C.; Wang, Y.-S.; Chang, H.-C.; Lin, S.; Lee, Y.; Niedner-Schatteburg, G.; Chang, H.-C. *J. Am. Chem. Soc.* **2000**, *122*, 1398–1410.

[151] Niedner-Schatteburg, G. *Angew. Chem., Int. Ed.* **2008**, *47*, 1008–1011.

[152] Hammer, N.; Shin, J.-W.; Headrick, J.; Diken, E.; Roscioli, J.; Weddle, G.; John-son, M. *Science* **2004**, *306*, 675–679.

[153] McCunn, L.; Headrick, J.; Johnson, M. *Phys. Chem. Chem. Phys.* **2008**, *10*, 3118–3123.

[154] Coe, J.; Arnold, S.; Eaton, J.; Lee, G.; Bowen, K. *J. Chem. Phys.* **2006**, *125*.

[155] Coe, J.; Williams, S.; Bowen, K. *Int. Rev. Phys. Chem.* **2008**, *27*, 27–51.

[156] Bragg, A.; Verlet, J.; Kammrath, A.; Cheshnovsky, O.; Neumark, D. *Science* **2004**, *306*, 669–671.

[157] Neumark, D. *Mol. Phys.* **2008**, *106*, 2183–2197.

[158] Kammrath, A.; Verlet, J.; Griffin, G.; Neumark, D. *J. Chem. Phys.* **2006**, *125*, 076101.

[159] Guasco, T.; Elliott, B.; Johnson, M.; Ding, J.; Jordan, K. *J. Phys. Chem. Lett.* **2010**, *1*, 2396–2401.

[160] Roscioli, J.; Hammer, N.; Johnson, M. *J. Phys. Chem. A* **2006**, *110*, 7517–7520.

[161] Kamrath, M.; Relph, R.; Johnson, M. *J. Am. Chem. Soc.* **2010**, *132*, 15508–15511.

[162] Relph, R.; Guaseo, T.; Elliott, B.; Kamrath, M.; McCoy, A.; Steele, R.; Schofield, D.; Jordan, K.; Viggiano, A.; Ferguson, E.; Johnson, M. *Science* **2010**, *327*, 308–312.

[163] Elliott, B.; Relph, R.; Roscioli, J.; Bopp, J.; Gardenier, G.; Guasco, T.; Johnson, M. *J. Chem. Phys.* **2008**, *129*, 094303.

[164] McCunn, L.; Gardenier, G.; Guasco, T.; Elliott, B.; Bopp, J.; Relph, R.; Johnson, M. *J. Chem. Phys.* **2008**, *128*, 234311.

[165] Relph, R.; Elliott, B.; Weddle, G.; Johnson, M.; Jing, D.; Jordan, K. *J. Phys. Chem. A* **2009**, *113*, 975–981.

[166] Choi, J.-H.; Kuwata, K.; Haas, B.-M.; Cao, Y.; Johnson, M.; Okumura, M. *J. Chem. Phys.* **1994**, *100*, 7153–7165.

[167] Roscioli, J.; Hammer, N.; Johnson, M.; Diri, K.; Jordan, K. *J. Chem. Phys.* **2008**, *128*, 104314.

[168] Kim, K.; Park, I.; Lee, S.; Cho, K.; Lee, J.; Kim, J.; Joannopoulos, J. *Phys. Rev. Lett.* **1996**, *76*, 956–959.

[169] Kim, K.; Lee, S.; Kim, J.; Lee, J. *J. Am. Chem. Soc.* **1997**, *119*, 9329–9330.

[170] Diken, E.; Weddle, G.; Headrick, J.; Weber, J.; Johnson, M. *J. Phys. Chem. A* **2004**, *108*, 10116–10121.

[171] Posey, L.; DeLuca, M.; Campagnola, P.; Johnson, M. *J. Phys. Chem.* **1989**, *93*, 1178–1181.

[172] Hart, E.; Gordon, S.; Thomas, J. *Radiat. Res.* **1964**, 74.

[173] Gordon, S.; Hart, E.; Matheson, M.; Rabani, J.; Thomas, J. *J. Am. Chem. Soc.* **1963**, *85*, 1375–1377.

[174] Elliott, B.; McCunn, L.; Johnson, M. *Chem. Phys. Lett.* **2008**, *467*, 32–36.

[175] Hammer, N.; Roscioli, J.; Johnson, M.; Myshakin, E.; Jordan, K. *J. Phys. Chem. A* **2005**, *109*, 11526–11530.

[176] Lee, G.; Arnold, S.; Eaton, J.; Bowen, K. *Chem. Phys. Lett.* **2000**, *321*, 333–337.

[177] Ma, L.; Majer, K.; Chirot, F.; Von Issendorff, B. *J. Chem. Phys.* **2009**, *131*, 144303.

[178] Choi, T.; Jordan, K. *Chem. Phys. Lett.* **2008**, *464*, 139–143.

[179] Jordan, K. *Science* **2004**, *306*, 618–619.

[180] Donald, W.; Williams, E. *J. Am. Soc. Mass Spectrom.* **2010**, *21*, 615–625.

[181] Coe A, J.; Lee, G.; Eaton, J.; Arnold, S.; Sarkas, H.; Bowen, K.; Ludewigt, C.; Haberland, H.; Worsnop, D. *J. Chem. Phys.* **1990**, *92*, 3980–3982.

[182] Kim, J.; Becker, I.; Cheshnovsky, O.; Johnson, M. *Chem. Phys. Lett.* **1998**, *297*, 90–96.

[183] Arnold, S.; Morris, R.; Viggiano, A.; Johnson, M. *J. Phys. Chem.* **1996**, *100*, 2900–2906.

[184] Compton, R.; Reinhardt, P.; Cooper, C. *J. Chem. Phys.* **1975**, *63*, 3821–3827.

[185] Donald, W.; Demireva, M.; Leib, R.; Aiken, M.; Williams, E. *J. Am. Chem. Soc.* **2010**, *132*, 4633–4640.

[186] Rashin, A.; Namboodiri, K. *J. Phys. Chem.* **1987**, *91*, 6003–6012.

[187] Prell, J.; O'Brien, J.; Holm, A.; Leib, R.; Donald, W.; Williams, E. *J. Am. Chem. Soc.* **2008**, *130*, 12680–12689.

[188] Leib, R.; Donald, W.; Bush, M.; O'Brien, J.; Williams, E. *J. Am. Soc. Mass Spectrom.* **2007**, *18*, 1217–1231.

[189] Holm, A.; Donald, W.; Hvelplund, P.; Larsen, M.; Nielsen, S.; Williams, E. *J. Phys. Chem. A* **2008**, *112*, 10721–10727.

[190] Viggiano, A.; Arnold, S.; Morris, R. *Int. Rev. Phys. Chem.* **1998**, *17*, 147–184.

[191] Motegi, H.; Takayanagi, T.; Tsuneda, T.; Yagi, K.; Nakanishi, R.; Nagata, T. *J. Phys. Chem. A* **2010**, *114*, 8939–8947.

[192] Anderson, J.; Fenn, J. *Phys. Fluids* **1965**, *8*, 780–787.

[193] Arnold, S.; Morris, R.; Viggiano, A. *J. Chem. Phys.* **1995**, *103*, 9242–9248.

[194] Ding, D.; Huang, J.; Compton, R.; Klots, C.; Haufler, R. *Phys. Rev. Lett.* **1994**, *73*, 1084–1087.

[195] Surber, E.; Mabbs, R.; Habteyes, T.; Sanov, A. *J. Phys. Chem. A* **2005**, *109*, 4452–4458.

[196] Nakanishi, R.; Nagata, T. *J. Chem. Phys.* **2009**, *130*, 224309.

[197] Eppink, A.; Parker, D. *Rev. Sci. Instrum.* **1997**, *68*, 3477–3484.

[198] Sanov, A.; Mabbs, R. *Int. Rev. Phys. Chem.* **2008**, *27*, 53–85.

[199] Gerardi, H.; Breen, K.; Guaseo, T.; Weddle, G.; Gardenier, G.; Laaser, J.; Johnson, M. *J. Phys. Chem. A* **2010**, *114*, 1592–1601.

[200] Johnson, M.; Lineberger, W. *Techniques for the Study of Ion Molecule Reactions* **1988**, *20*, 591–635.

[201] Roscioli, J.; Diken, E.; Johnson, M.; Horvath, S.; McCoy, A. *J. Phys. Chem. A* **2006**, *110*, 4943–4952.

[202] Donald, W.; Leib, R.; O'Brien, J.; Holm, A.; Williams, E. *Proc. Natl. Acad. Sci. U. S. A.* **2008**, *105*, 18102–18107.

[203] O'Brien, J.; Prell, J.; Holm, A.; Williams, E. *J. Am. Soc. Mass Spectrom.* **2008**, *19*, 772–779.

[204] Robertson, W.; Kelley, J.; Johnson, M. *Rev. Sci. Instrum.* **2000**, *71*, 4431–4434.

[205] Shin, J.-W.; Hammer, N.; Johnson, M.; Schneider, H.; Gi, A.; Weber, J. *J. Phys. Chem. A* **2005**, *109*, 3146–3152.

[206] Becke, A. *J. Chem. Phys.* **1993**, *98*, 5648–5652.

[207] Stephens, P.; Devlin, F.; Chabalowski, C.; Frisch, M. *J. Phys. Chem.* **1994**, *98*, 11623–11627.

[208] Suh, S.; Lee, H.; Kim, J.; Lee, J.; Kim, K. *J. Chem. Phys.* **2000**, *113*, 5273–5277.

[209] Bright Wilson Jr., E. *J. Chem. Phys.* **1935**, *3*, 276–283.

[210] Vaden, T.; Weinheimer, C.; Lisy, J. *J. Chem. Phys.* **2004**, *121*, 3102–3107.